SYNTHESES AND STRUCTURAL CHARACTERIZATIONS OF NEW INORGANIC ANHYDROUS BORATE COMPOUNDS

By

HYUNSOO PARK

A Thesis

Submitted to the School of Graduate Studies

in Partial Fulfillment of the Requirements

for the Degree

Master of Science

McMaster University

MASTER OF SCIENCE (2002) McMaster University

(Chemistry) Hamilton, Ontario

TITLE: Syntheses and Structural Characterizations of New Inorganic Anhydrous Borate Compounds

AUTHOR: Hyunsoo Park (B.Sc., McMaster University)

SUPERVISOR: Dr. Jacques Barbier

NUMBER OF PAGES: ix, 123

"For the harmony of the world is made manifest in Form and Number,
and the heart and soul and all the poetry of Natural Philosophy
are embodied in the concept of mathematical beauty."

D'Arcy Thompson, in *On Growth and Form*

ABSTRACT

A number of new ternary borate compounds have been synthesized, and their crystal structures have been characterized via X-ray and neutron diffraction techniques. A series of new compounds with the composition $PbMBO_4$ (M = Cr, Mn, Fe, Ga) has been prepared from solid-state reactions and from single crystal growths using PbO as a flux. They crystallize in the orthorhombic Pnma space group and represent a new structure-type for the family of anhydrous borates. The $PbAlBO_4$ compound undergoes a phase transformation at high temperatures, which has been investigated by *in-situ* powder neutron diffraction experiments. The structure of β-$PbAlBO_4$ has been solved from powder X-ray diffraction data and subsequently confirmed by a Rietveld refinement of powder neutron diffraction data. The investigation of the $SrO - Ga_2O_3 - B_2O_3$ system has led to the synthesis of a new structure-type, $SrGaBO_4$, from solid-state reactions. Its crystal structure has been determined from powder X-ray diffraction data. It crystallizes in the orthorhombic Pbam space group, and is structurally related to the previously known alumino-borate compounds, $SrAlBO_4$ and $CaAlBO_4$. The "$Ba_2Ti_2B_2O_9$" compound has been re-formulated as $Ba_3Ti_3B_2O_{13}$, and its crystal structure has been determined by single crystal X-ray diffraction. This compound crystallizes in the non-centrosymmetric $P\bar{6}2m$ space group. It is isostructural with $K_3Ta_3B_2O_{12}$ and the high temperature phase of $K_3Nb_3B_2O_{12}$.

ACKNOWLEDGEMENTS

First of all, I would like to express my deepest appreciation to my supervisor, Dr. Jacques Barbier, for his enthusiasm, guidance and patience throughout the course of my studies. I am very grateful to have had the opportunity to carry out my M.Sc. research in his group.

I'd like to extend my gratitude to Dr. J. E. Greedan for his support and encouragement as well as for his helpful advice on solid-state chemistry.

I'd like to thank Dr. J. F. Britten for collecting single crystal X-ray data and for his helpful advice on crystallographic problems. I also thank Dr. Robert Hammond at Chalk River Laboratories for collecting powder neutron diffraction data. I wish to acknowledge A. Kahn-Harari at Ecole Nationale Supérieure de Chimie de Paris for the NLO measurements.

I am also indebted to Dr. Hanna Dabkowska and Dr. Antoni Dabkowski for their valuable suggestions with single crystal growth experiments as well as for their support and encouragement during my studies. Special thanks go to all undergraduate and graduate students, visiting students and post-docs in the solid-state chemistry research group.

Finally, I'd like to thank my family and friends for their endless support and belief in me, especially when I was preparing this thesis. Without their love and kindness, this work would never have been completed.

TABLE OF CONTENTS

Abstract iv

Acknowledgements v

List of Tables vi

List of Figures viii

Chapter 1

INTRODUCTION 1

Chapter 2

DESCRIPTION OF EXPERIMENTS

2.1 Introduction 13

2.2 Solid-state syntheses 13

2.3 Single crystal growth using a flux 15

2.4 Powder X-ray diffraction 16

2.5 Single crystal X-ray diffraction 20

2.6 Structure determination from powder diffraction data 20

2.7 Rietveld structure refinement 24

2.8 Powder neutron diffraction 26

2.9 Bond valence analysis 28

Chapter 3

SYNTHESES AND STRUCTURES OF $PbMBO_4$ (M = Cr, Mn, Fe, Ga)

3.1 Introduction 31

3.2 Sample preparation

3.2.1 Solid-state syntheses 31

3.2.2 Single crystal growth 34

3.3 Structure determination and refinement

3.3.1 $PbMBO_4$ (M = Mn, Fe, Ga) 37

3.3.2 $PbCrBO_4$ 37
3.4 Description of the $PbMBO_4$ structure 43

Chapter 4

SYNTHESES AND STRUCTURES OF α- AND β-$PbAlBO_4$

4.1 Introduction 54
4.2 Sample preparation 54
4.3 Structure determination and refinement
4.3.1 α-$PbAlBO_4$ at room temperature 55
4.3.2 α-$PbAlBO_4$ at high temperatures 56
4.3.3 β-$PbAlBO_4$ at room temperature 60
4.4 Description of the $PbAlBO_4$ structures
4.4.1 α-$PbAlBO_4$ at room temperature 62
4.4.2 α-$PbAlBO_4$ at high temperatures 69
4.4.3 β-$PbAlBO_4$ at room temperature 71

Chapter 5

SYNTHESIS AND STRUCTURAL CHARACTERIZATION OF $SrGaBO_4$

5.1 Introduction 80
5.2 Sample preparation 80
5.3 Structure determination and refinement from powder
X-ray diffraction data 81
5.4 Description of the $SrGaBO_4$ structure (Pbam setting) 92
5.5 Comparison of $SrGaBO_4$ with other related compounds 96
5.6 Comparison of structure refinement results
(Pbam vs. $P2_12_12$) 99

Chapter 6

SYNTHESIS AND STRUCTURAL CHARACTERIZATION of $Ba_3Ti_3B_2O_{12}$

6.1 Introduction 101

6.2 Sample preparation

6.2.1 Solid-state syntheses 101

6.2.2 Single crystal growth 102

6.3 Structure determination and refinement from single crystal X-ray diffraction data 104

6.4 Description of the $Ba_3Ti_3B_2O_{12}$ structure 108

CONCLUSION 118

REFERENCES 120

LIST OF TABLES

1.1	Ternary alumino-borate compounds	3
1.2	Ternary gallo-borate compounds	10
2.1	Chemical reagents used	14
3.1	Crystal growth conditions and crystal colours of $PbMBO_4$ (M = Mn, Fe, Ga)	35
3.2	Details of single crystal and powder X-ray diffraction refinements	38
3.3	Crystal data for $PbMBO_4$ (M = Al, Cr, Mn, Fe, Ga)	39
3.4	Atomic coordinates and isotropic displacement parameters of $PbMBO_4$	40
3.5	Anisotropic displacement parameters for $PbMBO_4$ (M = Mn, Fe, Ga)	41
3.6	Selected bond distances and valences in $PbMBO_4$	44
3.7	Selected bond angles in $PbMBO_4$	45
4.1	Details of the structure refinement	
	a. α-$PbAlBO_4$ at RT	57
	b. α-$PbAlBO_4$ at high temperatures	57
	c. β-$PbAlBO_4$ at RT	57
4.2	Crystal data for $PbAlBO_4$	63
4.3	Atomic coordinates and isotropic displacement parameters	
	a. α-$PbAlBO_4$ at RT	64
	b. β-$PbAlBO_4$ at RT	64
4.4	Atomic coordinates and isotropic displacement parameters of α-$PbAlBO_4$ at high temperatures	65
4.5	Bond distances, bond valences and bond angles in α-$PbAlBO_4$ at RT	67
4.6	Bond valences around oxygen atoms in α-$PbAlBO_4$ at RT	67
4.7	Bond distances in α-$PbAlBO_4$ at high temperatures	70
4.8	Bond valences in α-$PbAlBO_4$ at high temperatures	70

4.9	Bond distances, bond valences and bond angles in β-$PbAlBO_4$	72
4.10	Bond valences around oxygen atoms in β-$PbAlBO_4$	72
5.1	Indexed powder X-ray pattern of $SrGaBO_4$	82
5.2	Details of Rietveld refinement of $SrGaBO_4$	85
5.3	Crystal data for $SrGaBO_4$ and its related compounds	87
5.4	Atomic coordinates and isotropic displacement parameters of $SrGaBO_4$	
	a) Pbam	88
	b) Pba2	88
5.5	Bond distances, bond valences and bond angles for $SrGaBO_4$	
	a) Pbam	90
	b) Pba2	91
6.1	Products from single crystal growth of $Ba_3Ti_3B_2O_{12}$ from melt	103
6.2	Crystallographic data and single crystal X-ray diffraction refinement for $Ba_3Ti_3B_2O_{12}$	105
6.3	Atomic coordinates and isotropic displacement parameters for $Ba_3Ti_3B_2O_{12}$	107
6.4	Anisotropic displacement parameters for $Ba_3Ti_3B_2O_{12}$	107
6.5	Bond distances, bond valences and bond angles in $Ba_3Ti_3B_2O_{12}$	110
6.6	Crystallographic data for $Ba_3Ti_3B_2O_{12}$ and its related compounds	114

LIST OF FIGURES

1.1	Structures of $CaAlBO_4$ and $SrAlBO_4$	4
1.2	Structures of $CaAl_2B_2O_7$ and $BaAl_2B_2O_7$	6
1.3	Phase diagram of $BaO - Al_2O_3 - B_2O_3$ system	8
1.4	Crystal structure of $SrGa_2B_2O_7$	9
2.1	Schematic diagram of a Guinier-Hägg camera	17
2.2	Schematic diagram of a Bragg – Brentano powder diffractometer	19
2.3	Sketch of single crystal X-ray diffractometer	21
2.4	Procedures of *ab-initio* structure determination from powder X-ray diffraction data	23
2.5	Schematic diagram of the C2 powder neutron diffractometer	27
3.1	Photograph of $PbMBO_4$ (M = Mn, Fe, Ga) crystals	36
3.2	Rietveld refinement plot of $PbCrBO_4$	42
3.3	Crystal structure of $PbMBO_4$ near the [010] direction	47
3.4	Structure of $PbMBO_4$ viewed along the c-axis	48
3.5	Bonding environment around Mn^{3+} ions in $PbMnBO_4$	49
4.1	Rietveld refinement plot of α-$PbAlBO_4$ at room temperature	58
4.2	Rietveld refinement plots of α-$PbAlBO_4$ at high temperatures	59
4.3	Rietveld refinement plot of β-$PbAlBO_4$ at room temperature	61
4.4	Crystal structure of α-$PbAlBO_4$	68
4.5	Crystal structure of β-$PbAlBO_4$	73
4.6	Bridging environments of AlO_6 chains in α, β-$PbAlBO_4$	74
4.7	$Pb^{2+} \cdots Pb^{2+}$ distances in $PbAlBO_4$	78
5.1	Electron diffraction pattern of $SrGaBO_4$	83
5.2	Rietveld refinement plot of $SrGaBO_4$	86

5.3	Crystal structure of $SrGaBO_4$	94
5.4	GaO_4 chain and BO_3 groups in the $SrGaBO_4$ structure	95
5.5	Structures of $SrGaBO_4$ and its related compounds	97
6.1	Crystal structure of $Ba_3Ti_3B_2O_{12}$ along the [001] direction	111
6.2	Crystal structure of $Ba_3Ti_3B_2O_{12}$ near the [111] direction	112
6.3	Structures of $K_3Nb_3Si_2O_{13}$ and $Ba_{1.5}Nb_3Si_2O_{13}$	116

Chapter 1

INTRODUCTION

Although boron is not an abundant element in the universe, the crystal chemistry of inorganic borate compounds is as diverse and complex as that of silicates. In nature, boron occurs as borate minerals or as borosilicates. There are more than 100 known borate minerals, and most of them are hydrated as they contain OH^- or H_2O groups (Grice *et al.*, 1999). The complexity and variety of borate crystal structures arise due to the fact that boron atoms can be found in either a triangular or a tetrahedral coordination environment. In some cases, both geometries are observed in the same compound. For borates based only on the BO_3 triangular groups, the compounds can be classified according to the basic unit found in the structures (Heller, 1986). An *orthoborate* is a compound which contains isolated BO_3^{3-} groups. No oxygen atom is shared between two B atoms. If dimers of BO_3 triangles are found, the compound is called a *pyroborate* which can be formulated as $B_2O_5^{2-}$. A *metaborate* of empirical formula BO_2^- consists of an infinite one-dimensional chain ($(BO_2)_n^{n-}$) or a 6-membered ring by linking three BO_3 groups by corners ($(B_3O_6)^{3-}$). The polymerization of triangular and tetrahedral coordination polyhedra leads to a large number of intricate and unique structures. The lengths of B – O bond range from 1.28 to 1.43 Å for triangular coordination, and from 1.43 to 1.55 Å for tetrahedral coordination (Wells, 1984). These short and rigid B – O bonds therefore can provide a strong backbone for the whole structure of a given borate compound.

The study of synthetic anhydrous borates has been an active area of research in both chemistry and materials science around the world, in search of new compounds with potential applications as optical materials. Since the successful application of β-BaB_2O_4 to the frequency doubling of laser light (Chen *et al.*, 1985), a number of non-centrosymmetric borate compounds have been synthesized and their non-linear optical properties have been tested. These compounds are binary borates such as LiB_3O_5 (Chen *et al.*, 1989) and CsB_3O_5 (Mori *et al.*, 1995) as well as ternary borates including $K_2Al_2B_2O_7$ (Hu *et al.*, 1999), $K_2Ga_2B_2O_7$ (Smith *et al.*, 1997) and $Sr_2Be_2B_2O_7$ (Chen *et al.*, 1995). A recent review by Becker (1998) lists 36 borate compounds which have been used or suggested for their non-linear optical applications. Eu^{2+}-doped borates have been also extensively studied in search of new UV or blue-emitting materials. Although most Eu^{2+}-doped borates exhibit an excitation at low energy at room temperature, a high intensity emission was reported for the UV emission of SrB_4O_7:Eu^{2+} at 368 nm (Machida *et al.*, 1979).

In spite of numerous compounds reported, so far few studies on ternary borates have been carried out systematically. In the case of the alumino-borate systems, MO – Al_2O_3 – B_2O_3 (M = Ca, Sr, Ba), the initial work took place in the late 1960's, and Table 1.1 describes the ternary alumino-borates found in these systems since then. The CaO – Al_2O_3 – B_2O_3 system was first studied by Schäfer and Kuzel (1967). They reported two new alumino-borates $CaAlBO_4$ and $CaAl_2B_2O_7$, but only the unit-cell parameters were given. The structure of $CaAlBO_4$ was subsequently determined by Schuckmann (1968). Its crystal structure is depicted in Figure 1.1. It is based on infinite chains of corner-sharing AlO_4 tetrahedra and BO_3 triangular groups. The Ca^{2+} ions occur in the resulting

Table 1.1 Ternary alumino-borate compounds whose structures have been determined

Compound	Space group	Unit-cell parameters (Å)	Z	Reference
$CaAl_2B_2O_7$	$R\bar{3}c$	a = 4.810(6) c = 46.633(5)	3	Chang & Keszler, 1998
$SrAl_2B_2O_7$	$R\bar{3}c$	a = 4.893(1) c = 47.78(1)	3	Lucas *et al.*, 2000
$BaAl_2B_2O_7$	R32	a = 5.001(2) c = 24.378(3)	3	Ye *et al.*, 1998
$CaAlBO_4$	Ccc2	a = 8.629(2) b = 15.227(3) c = 5.733(3)	8	Schuckmann, 1968
$SrAlBO_4$	Pccn	a = 15.17(4) b = 8.86(3) c = 5.48(2)	8	Nagai & Ihara, 1972

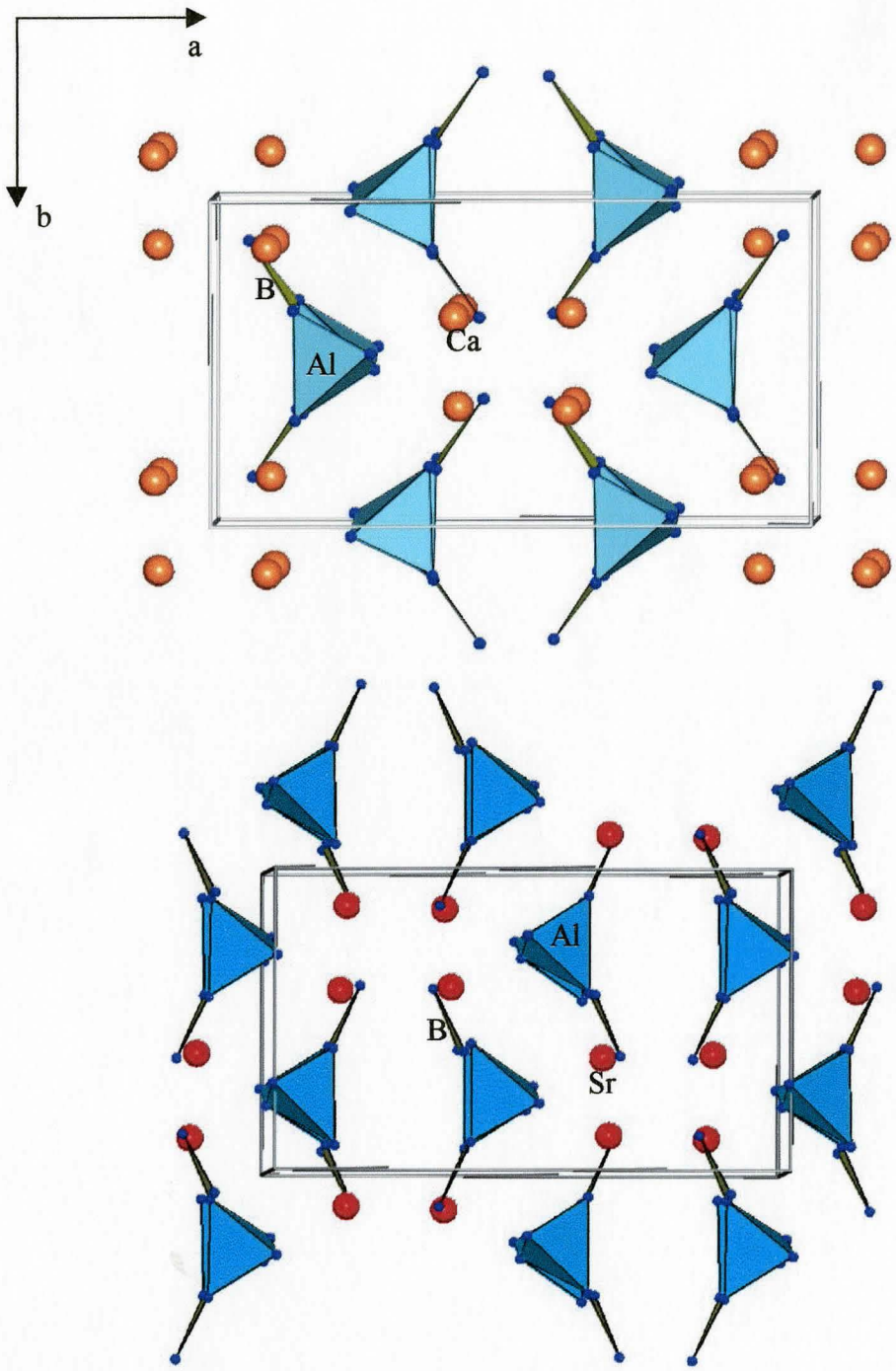

Figure 1.1 Structures of $CaAlBO_4$ (top; Schuckmann, 1968) and $SrAlBO_4$ (bottom; Nagai & Ihara, 1972)

channels between the $AlBO_4$ chains. The crystal structure of $CaAl_2B_2O_7$ had not been established until recently (Chang & Keszler, 1998). This compound crystallizes in the trigonal space group $R\bar{3}c$. This structure is illustrated in Figure 1.2. This structure, which can be described as an orthoborate, $CaAl(BO_3)_2O$, is characterized by double layers of AlO_4 tetrahedra parallel to the c-axis, which are further linked alternately by BO_3 triangles, to form a six-membered ring. The Ca^{2+} ions are located in the cavities between the layers.

In the SrO-Al_2O_3-B_2O_3 system, two compounds have been discovered, namely $SrAlBO_4$ (Nagai & Ihara, 1972) and $SrAl_2B_2O_7$ (Lucas *et al.*, 2000). The latter compound has been fully structurally characterized, and its luminescence properties have been examined by doping with Eu^{2+} ions. Like its Ca analogue, $SrAl_2B_2O_7$ also crystallizes in the rhombohedral space group $R\bar{3}c$ (Table 1.1). The compound $SrAlBO_4$ has been described in the orthorhombic space group Pccn. However, the results of the structure refinements are not very reliable, as indicated by a high value of agreement factor (R = 16.3%) and a large range of Al – O bond lengths (1.59 – 1.80 Å). Nonetheless, it displays structural features which are very similar to those seen in $CaAlBO_4$ (cf. Figure 1.1). Both compounds, which can be formulated as orthoborates, are built of corner-sharing AlO_4 chains and BO_3 triangles which bridge adjacent AlO_4 tetrahedra. One major difference between the two structures is the lack of C-centering in $SrAlBO_4$ due to non-equivalent orientations of the AlO_4 chains which arise from different coordination environments around the Sr^{2+} ions (CN = 7) from the Ca^{2+} ions (CN = 6).

In the BaO – Al_2O_3 – B_2O_3 system, a number of compounds have been synthesized via solid-state reactions and single crystal growths (Hübner, 1970). Figure

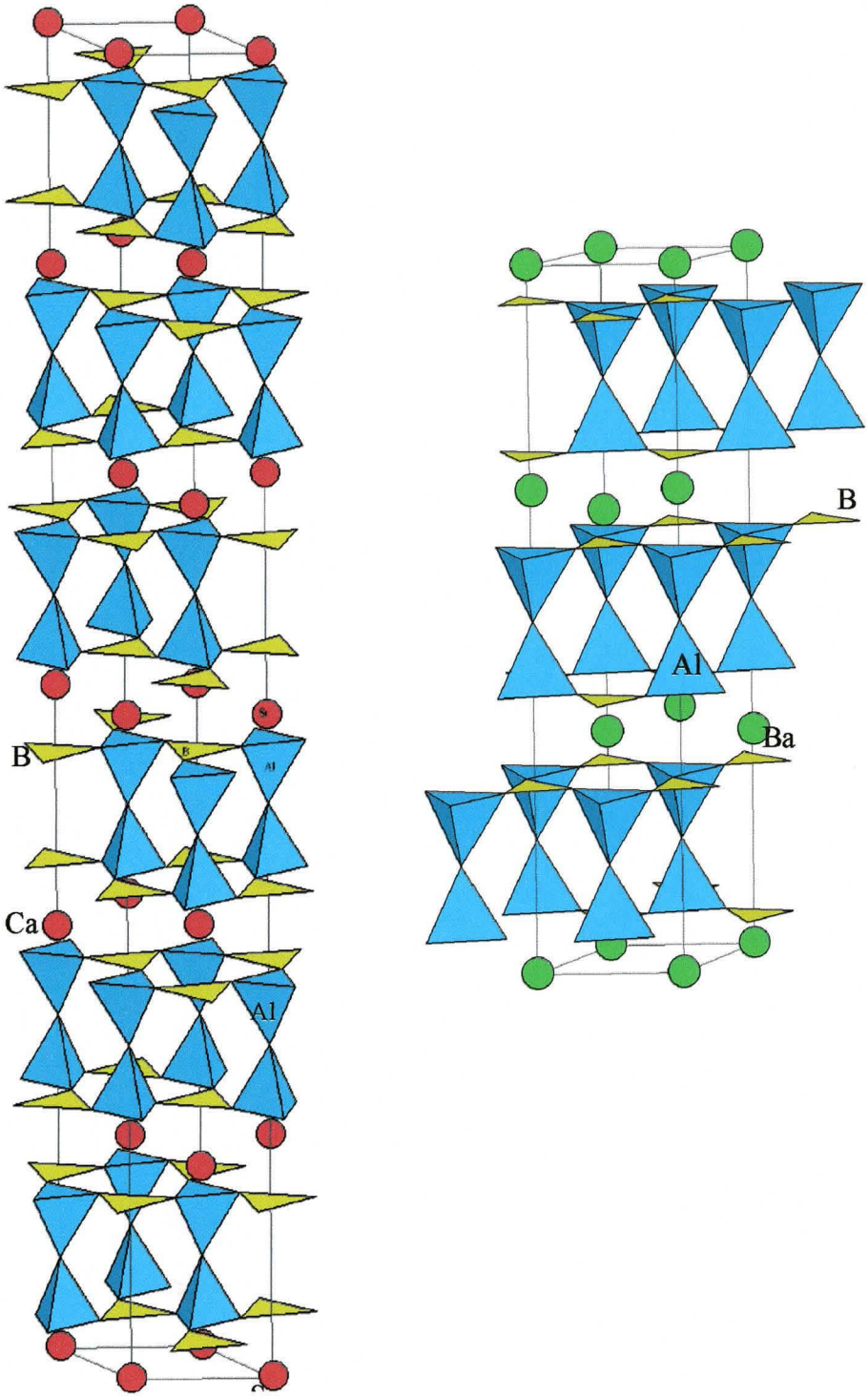

Figure 1.2 Structures of $CaAl_2B_2O_7$ (left; Chang & Keszler, 1998) and $BaAl_2B_2O_7$ (right; Ye *et al.*, 1998).

1.3 shows a phase diagram showing all the compositions prepared in this system. Among these compounds, only $BaAl_2B_2O_7$ has been structurally characterized so far (Ye *et al.*, 1998). This compound crystallizes in the trigonal R32 space group. It shares many structural similarities with its Ca and Sr analogues (cf. Figure 1.2). However, no centre of symmetry is present in $BaAl_2B_2O_7$, as a c-glide plane is replaced by two-fold axis.

In an attempt to synthesize the gallium analogues of the known alumino-borates, the $MO - Ga_2O_3 - B_2O_3$ (M = Sr, Ba) systems have been recently investigated. Two new compounds, namely $SrGa_2B_2O_7$ and $BaGa_2B_2O_7$, have been synthesized and their structures have been determined (Park & Barbier, 2000). These compounds crystallize in the orthorhombic space group Cmcm. Despite the identical composition, they are structurally distinct from their aluminum analogues (Figure 1.4). Their structures are built of a three-dimensional framework of corner-sharing GaO_4 tetrahedra and BO_3 triangles. The eight-coordinated M^{2+} cations are present in the cavities of the framework. These compounds can be formulated as pyroborates, $MGa_2(B_2O_5)O_2$, whereas the corresponding alumino-borates are orthoborates with formula $MAl_2(BO_3)_2O$.

At the time this thesis was being written, Yang *et al.* (2001, 2002) have published the reports illustrating the structural characterizations of two additional gallo-borate compounds, namely $CaGaBO_4$ and β-$SrGaBO_4$. While the $CaGaBO_4$ compound is isostructural to $CaAlBO_4$ (Schuckmann, 1968), the β-$SrGaBO_4$ compound, described in the $P2_12_12$ space group, exhibits many structural similarities with its Al-analogue as well as with $CaGaBO_4$, such as the GaO_4 tetrahedral chains and the BO_3 groups which bridge adjacent tetrahedra. The crystal data for the known borates in the $MO - Ga_2O_3 - B_2O_3$ systems (M = Ca, Sr, Ba) are listed in Table 1.2.

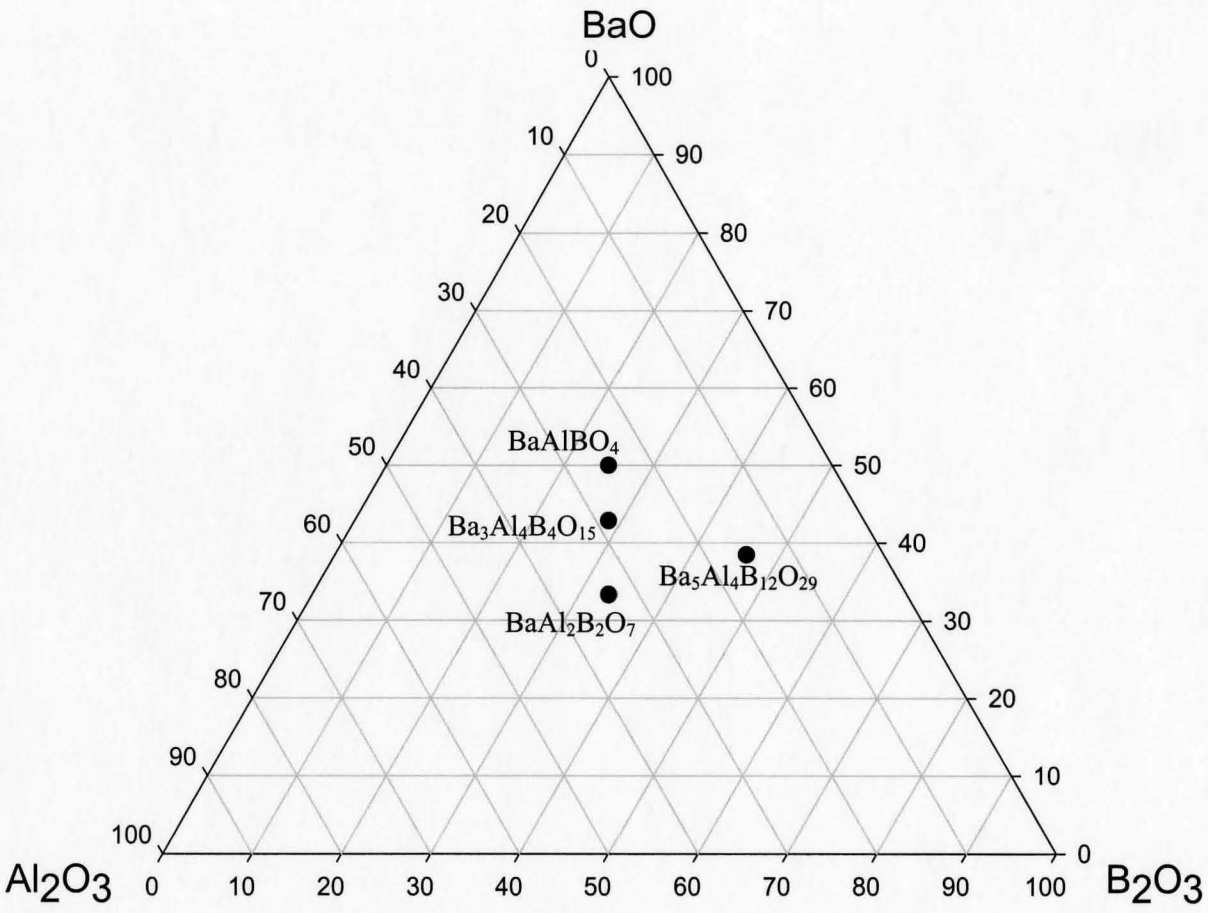

Figure 1.3 Phase diagram of $BaO - Al_2O_3 - B_2O_3$ system (Hübner, 1970). Only the structure of $BaAl_2B_2O_7$ has been fully characterized (Ye *et al.*, 1998).

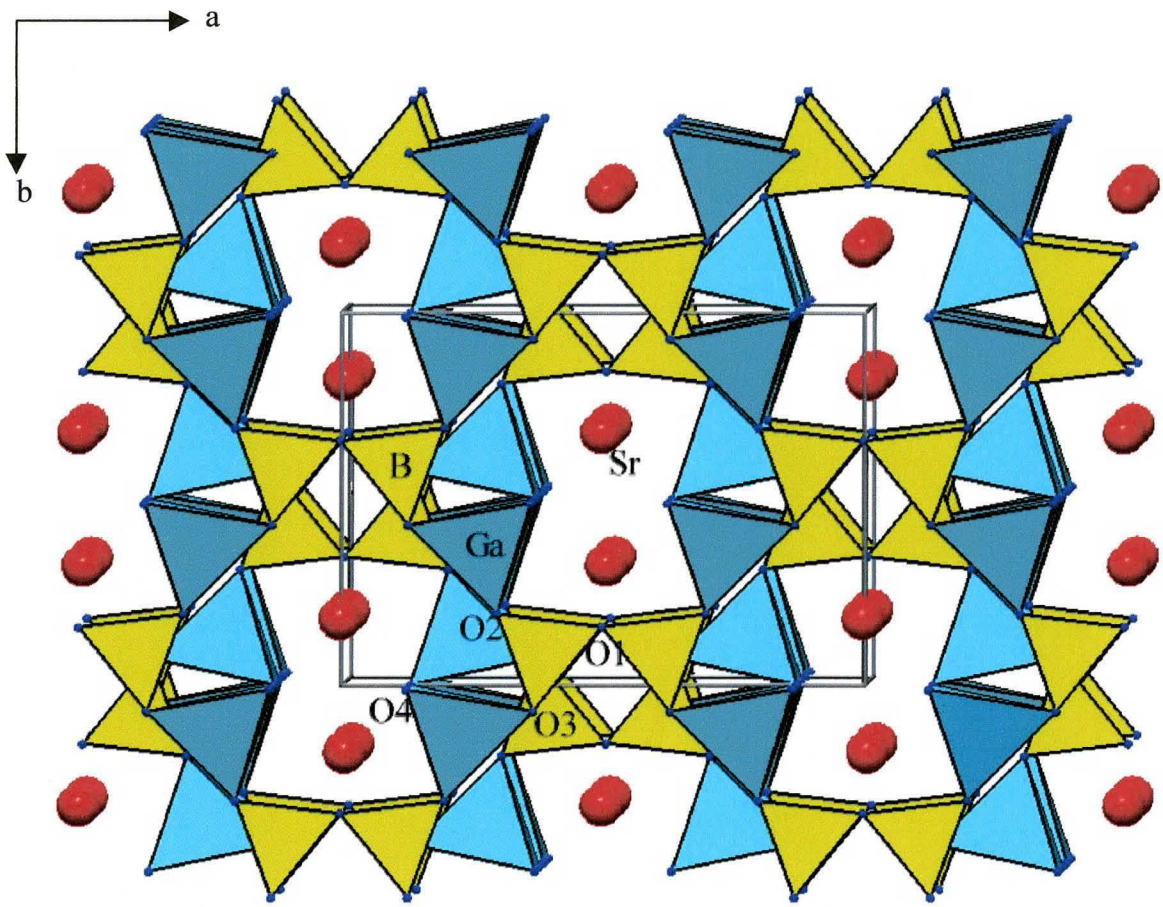

Figure 1.4 Crystal structure of $SrGa_2B_2O_7$ viewed near the [001] direction (Park & Barbier, 2000).

Table 1.2 Ternary gallo-borate compounds whose structures have been determined

Compound	Space group	Unit-cell parameters (Å)	Z	Reference
$SrGa_2B_2O_7$	Cmcm	a = 11.7260(7) b = 8.3745(4) c = 5.7062(3)	4	Park & Barbier, 2000
$BaGa_2B_2O_7$	Cmcm	a = 11.7434(6) b = 8.7076(4) c = 5.8038(3)	4	Park & Barbier, 2000
$CaGaBO_4$	Ccc2	a = 15.473(1) b = 8.2940(8) c = 5.8392(6)	8	Yang *et al.*, 2001
β-$SrGaBO_4$*	$P2_12_12$	a = 15.3706(2) b = 8.9921(1) c = 5.9191(1)	8	Yang *et al.*, 2002

*An alternative structure determination of $SrGaBO_4$ in the Pbam space group is discussed in Chapter 5.

The $BaO - TiO_2 - B_2O_3$ system was first investigated by Vicat and Aléonard (1968) as a part of studies on dolomite-type borates with the composition $M^{2+}M^{4+}(BO_3)_2$. One ternary titanium borate, $BaTiB_2O_6$, was reported. This compound crystallizes in the rhombohedral $R\bar{3}$ space group with unit-cell parameters of a = 5.02(8) Å, c = 16.4(1) Å. While examining the phase relations among BaO, TiO_2 and B_2O_3, a new ternary compound with the composition $Ba_2Ti_2B_2O_9$ was discovered (Millet *et al.*, 1986). However, the authors were not able to prepare this compound as a single phase, since $BaTiO_3$ and $BaTiB_2O_6$ impurities remained even after repeated long firings. No detailed structural characterization was carried out except the determination of unit-cell parameters. From a powder X-ray diffraction pattern, this compound was determined to crystallize in the hexagonal symmetry with unit-cell parameters of a = 8.722(2) Å, c = 3.933(2) Å.

In this work, a number of new inorganic ternary borate compounds have been investigated. Three particular borate structure-types have been studied, namely $PbMBO_4$ (M = Al, Cr, Mn, Fe, Ga), $SrGaBO_4$ and $Ba_3Ti_3B_2O_{12}$. These compounds have been prepared as well-crystallized powders via solid-state reactions or as single crystals from slow-cooling of melts. Their structures have been characterized in detail via various techniques such as X-ray and neutron diffraction methods. In particular, the application of *ab-initio* structure determination was examined by solving crystal structures of two new borate compounds from powder X-ray diffraction data. For all the compounds discussed in this thesis, bond valence analysis was extensively applied in order to identify and to understand any irregularities in bonding, including over- or under-bonding of an atom (or an ion) in the structure.

The isostructural $PbMBO_4$ compounds have been synthesized from solid-state reactions and single crystal growths (Park & Barbier, 2001). They have been characterized structurally by powder and single crystal X-ray diffraction techniques. In particular, the phase transformation of $PbAlBO_4$ at high temperatures has been examined by *in-situ* powder neutron diffraction experiments. The structural changes of α-$PbAlBO_4$ at high temperatures have been also investigated. The structure of β-$PbAlBO_4$ at room temperature has been determined from powder X-ray diffraction data and confirmed by a Rietveld refinement of powder neutron diffraction data.

In the $SrO - Ga_2O_3 - B_2O_3$ system, a new compound, $SrGaBO_4$, has been synthesized from solid-state reactions. Its crystal structure has been solved and characterized using powder X-ray diffraction data. The structural characterization has been compared with that described in the recent report by Yang *et al.* (2002).

The last compound of interest in this thesis was $Ba_3Ti_3B_2O_{12}$, which had been previously reported as $Ba_2Ti_2B_2O_9$. By single crystal X-ray diffraction, the formula of this compound has been re-determined. Its structure has been compared with isostructural $K_3M_3B_2O_{12}$ (M = Nb, Ta; Becker *et al.*, 1997; Abrahams, *et al.* 1981) as well as several related silicate compounds, $Ba_{1.5}M_3Si_2O_{13}$ (Shannon & Katz, 1970) and $K_3M_3Si_2O_{13}$ (Choisnet *et al.*, 1976; Jaulmes *et al.*, 1995).

Chapter 2

DESCRIPTION OF EXPERIMENTS

2.1 Introduction

This chapter describes various experimental conditions and techniques to prepare single crystals as well as polycrystalline samples in this research. A number of structural characterization methods are also discussed.

2.2 Solid-State Syntheses

All compounds discussed in this work were synthesized as polycrystalline powders via solid-state reactions. Table 2.1 lists the purities of chemical reagents used as starting materials for the solid-state syntheses. Boric acid (H_3BO_3) was used as a source of boron oxide which is hygroscopic in air. For the preparation of samples for powder neutron diffraction experiments, ^{11}B-enriched boric acid was employed in order to minimize the absorption of neutrons by ^{10}B.

For a typical solid-state synthesis, stoichiometric amounts of the starting materials were mixed and ground in acetone using an agate pestle and mortar. The mixed powders were pressed into small pellets of 0.50 to 1.00-g which were placed in an alumina boat or a platinum crucible and heated slowly (1°C min^{-1}) up to 500°C to dehydrate boric acid. The re-mixed and re-pelletized samples were then fired at higher temperatures for 3 – 5 days in air in a box furnace. A tube furnace with flowing inert gas (usually high purity argon) was also used when a controlled atmosphere was required (e.g. for the synthesis of $PbCrBO_4$ in Chapter 3). The heating conditions required to obtain the desired compounds were determined by trial and error. Since borate compounds tend to melt

Table 2.1 Reagents used for sample preparations and syntheses

Reagent	Purity and manufacturer
$BaCO_3$	99%, J. T. Baker
$Ba(NO_3)_2$	99%, Alfa Aesar
$SrCO_3$	99%, Alfa Aesar
$Sr(NO_3)_2$	99%, Alfa Aesar
PbO	99.9%, Fisher Scientific
$BaTiO_3$	99.99%, Aldrich
Ga_2O_3	99.99+%, Aldrich
Al_2O_3	99.2%, Cerac
Fe_2O_3	Reagent grade, Fisher Scientific
MnO_2	99.9%, J. T. Baker
TiO_2	99.9%, Cerac
$Cr(NO_3)_3.9H_2O$	98.9%, J. T. Baker
H_3BO_3	99.99%, Alfa Aesar
H_3BO_3 (^{11}B-enriched)	99.27%, Eagle Picher

incongruently at relatively low temperatures (750 – 950°C), it was essential to find the maximum heating temperature to ensure complete reactions among the starting materials without melting and formation of glass. After each heating period, an X-ray pattern was recorded to monitor the reaction progress. Further details on the preparation of each sample are described in the relevant chapters as each compound was synthesized using different reaction conditions.

2.3 Single Crystal Growth Using a Flux

Flux growth utilizes a molten inorganic solvent to grow crystals of a solute at high temperature. This method allows the crystals to grow at temperatures below the melting point of the solute phase. The reduction in temperature is one of the advantages of flux growth over the growth from a pure melt. It is essential to understand the following in order to use and appreciate the flux method:

- The solubility of various molten salts to choose an appropriate flux
- The phase relationship between solute and flux to ensure the precipitation of the desired crystals only

The flux can be either one of the constituents of the crystals of interest or a compound completely separate from the solute. The most commonly used fluxes are alkali borates, lead oxide/fluoride, alkali molybdates and halides since they have low melting points allowing the crystallization process to take place at relatively low temperatures (Pamplin, 1975).

In this work, lead oxide (PbO), with a melting point of 886°C, was used as a flux to grow crystals of PbO-based borates. For a typical experiment, 10.0 – 12.0 g of well-

mixed starting materials were melted in a covered platinum crucible at 900 – 1000°C, soaked for several hours and cooled down slowly at a rate of 3 - 5°C hr^{-1}. The solidified product was hammered out of the crucible and soaked in dilute acid to separate the crystals from the PbO flux.

2.4 Powder X-ray Diffraction

A polycrystalline sample consists of a large number of small particles arranged in random orientations. These crystallites will diffract X-ray beams if they are oriented in such a way that Bragg's Law, $\lambda = 2d\sin\theta$, is satisfied. The diffracted beams can be collected by a photographic film or by a movable detector. Two types of powder X-ray instruments were used in this work: a Guinier-Hägg camera ($CuK\alpha_1$ radiation, $\lambda = 1.5406$ Å) and a Bruker D8 diffractometer ($CuK\alpha$ radiation, $\lambda = 1.542$ Å or $CuK\alpha_1$).

A Guinier camera utilizes a bent quartz crystal monochromator, placed between the X-ray source and the sample, to give an intense, convergent X-ray beam. A schematic diagram of the Guinier geometry is illustrated in Figure 2.1. The orientation of the crystal can be adjusted so that it diffracts the incident beam which is then converted into a convergent beam to strike the sample. The beams diffracted by the sample are focused on the surface of a photographic film. The primary use of the Guinier camera is for monitoring the reaction progress in the solid-state syntheses and for checking the purity of the prepared samples.

The Guinier diffraction pattern is scanned using a KEJ-LS20 digital scanner to measure peak positions and intensities. The computer program SCANPI (Malmros & Werner, 1973) is then used to calculate the corrected line positions and integrated

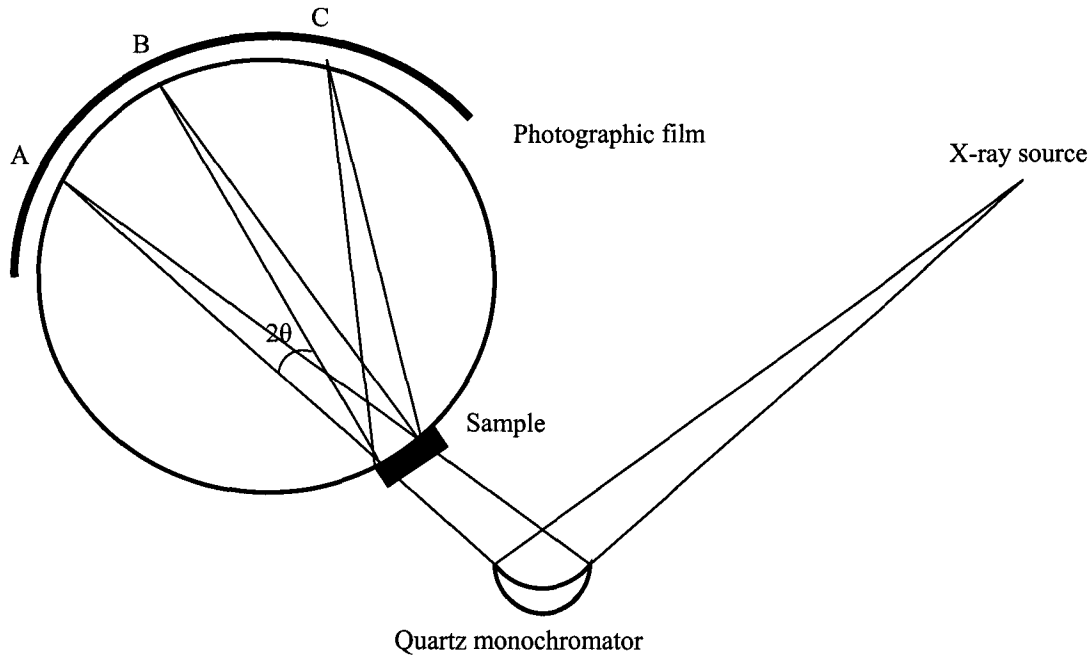

Figure 2.1 A schematic diagram of a Guinier-Hägg camera

intensities. An internal standard (Si powder) is employed to correct for film shrinkage and sample displacement. Since it produces profiles of excellent spatial resolution, the diffraction profile from a Guinier camera is also used to determine the unit-cell parameters of new compounds and solve their crystal structures using various computer software packages. The details of the structure determination from Guinier data are discussed in Section 2.5.

The Bruker D8 powder diffractometer employs the Bragg-Brentano (reflection) geometry. The arrangement of the Bragg-Brentano geometry is described in Figure 2.2 (Jenkins & Snyder, 1996). The instrument has a vertical θ - 2θ configuration, where the sample position and receiving slit vary as θ and 2θ, respectively, while the X-ray source remains stationary. The X-ray source and the receiving slits are at equal distances from the specimen so that a parafocusing geometry is established.

A divergent beam from the X-ray source (F) first goes through a divergence slit (DS), then a set of soller slits (collimator) (SS1) before hitting the sample (S) at an angle θ. The soller slits are used to minimize the axial divergence of the beam, thus to partially control the line shape of the diffraction profile. The diffracted X-ray beam then leaves the sample and passes through a second set of soller slits (SS2), through the receiving slit (RS). A monochromator (C) is placed between the receiving slit and the detector to remove Kβ radiation and sample fluorescence. Finally the diffracted beams are collected by a scintillation counter.

The diffraction patterns were usually measured over a 2θ range of 10.00° - 130.00° with a stepsize of 0.03° and a counting time of 13 seconds per step. Since the D8

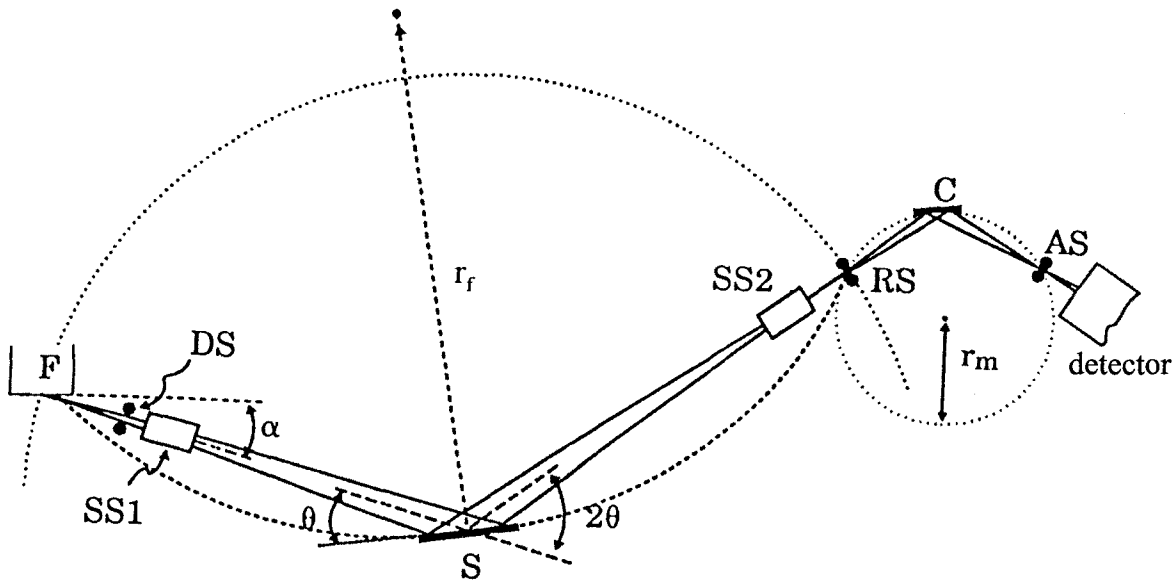

Figure 2.2 A schematic diagram of a powder X-ray diffractometer with θ - 2θ Bragg-Brentano geometry (Jenkins & Snyder, 1996)

instrument provides a diffraction pattern with high resolution and good signal-to-noise ratio, the data can be used for Rietveld analysis and structure refinement.

2.5 Single Crystal X-ray Diffraction

All single crystal X-ray data were collected by Dr. J. F. Britten of Department of Chemistry, McMaster University, with a Siemens P4 diffractometer equipped with a MoKα rotating anode and a SMART 1K CCD area detector. A schematic diagram of the single crystal X-ray diffractometer is shown in Figure 2.3. The instrument has four circles, each with unique rotating axis (ϕ, χ, ω, 2θ), which allows to adjust the orientation of the crystal in order to bring any desired plane into a reflecting position and measure this reflection. The raw intensity data were first corrected for Lorentz and polarization effects using the computer software SAINT (Siemens, 1996). Absorption corrections were applied either by an empirical method, SADABS (Sheldrick, 2001), or by integration (face-indexing). With the software package SHELXTL (Sheldrick, 1997), the structures were then solved by direct methods and the least-squares refinements were carried out.

2.6 Structure Determination from Powder Diffraction Data

Although single crystal X-ray diffraction is the most powerful technique for the elucidation of a new crystal structure, it is not always applicable since many compounds cannot be prepared as single crystals of sufficient size and quality. As a result, the use of powder diffraction data has become more recognized in recent years as a tool for structure determination of new crystalline solids (Clearfield & Poojary, 1997; Harris *et*

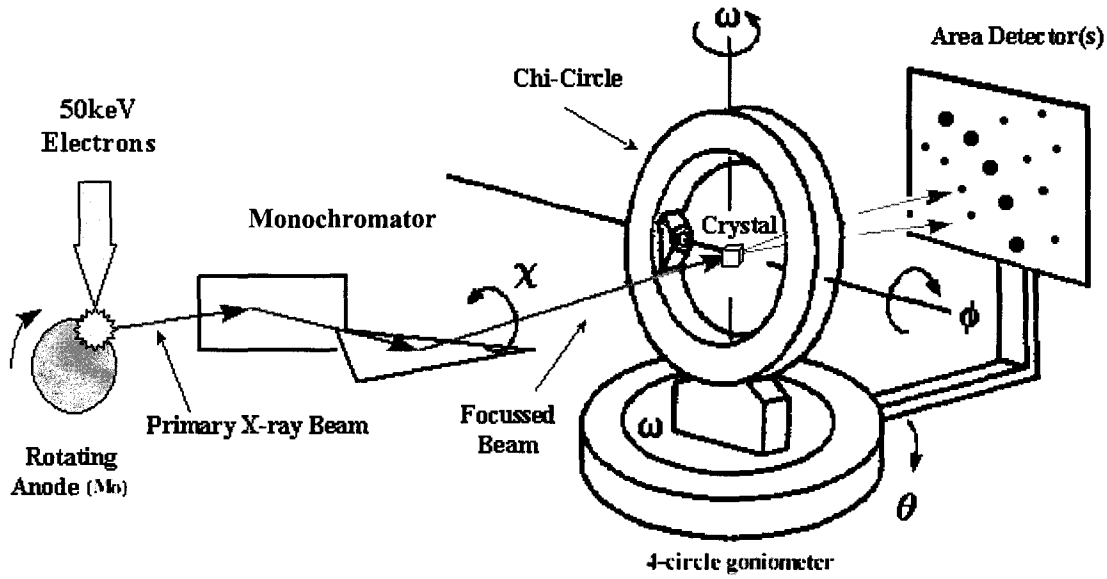

Figure 2.3 A sketch of a single crystal X-ray diffractometer setup

al., 2001). Substantial progresses have been made in the development of the design and implementation of computer software for the *ab-initio* structure determination from powder data.

Crystal structure determination from powder diffraction can be divided into three stages: (1) unit-cell determination and space group assignment, (2) structure solution, and (3) structure refinement. A schematic diagram of the structure determination procedure is given in Figure 2.4. The unit-cell parameters can be found by indexing the diffraction peaks, then possible space groups can be assigned by careful examination of systematic absences present in the pattern. A number of computer programs have been employed to determine unit-cell parameters; VISSER (Visser, 1969) was used to calculate the unit-cell dimensions; LSUDF (Evans *et al.*, 1963) and CHEKCELL (Laugier & Bochu, 2001) were applied to index the patterns as well as to perform least-squares refinements of the unit-cell parameters. CHEKCELL also searches for the possible space group for a given cell based on the extinction conditions.

There are two currently available approaches for structure solution: "traditional" and "direct-space" methods. The traditional method is based on the extraction of the intensities of individual reflections, which can be used to solve the structure. As in the case of single crystal X-ray diffraction, this technique utilizes either direct or Patterson methods for phasing to solve the structure. However, problems arise with the traditional method due to peak overlap which leads to inaccurate intensities. Several peak extraction methods have been developed in order to overcome these difficulties (Pawley, 1981; Le Bail *et al.*, 1988). The "direct-space" approach does not depend on the intensity extraction from the powder pattern at all. This method generates numerous trial

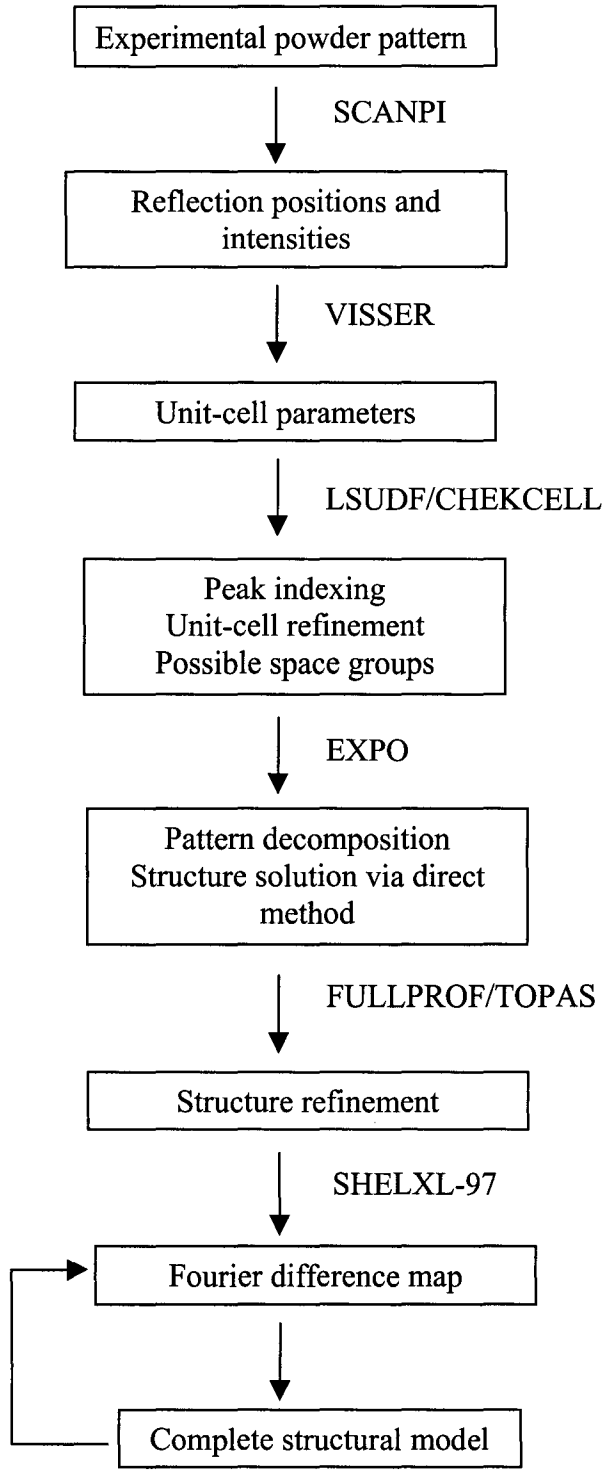

Figure 2.4 Procedures of structure determination from powder X-ray diffraction data

structures whose calculated powder patterns can be compared to the experimental pattern for acceptance or rejection. This approach includes the Monte Carlo (Harris *et al.*, 1994), Simulated Annealing (Andreev *et al.*, 1999) and Genetic Algorithm (Harris *et al.*, 1998) methods.

The structure determinations from powder data in this work employed the "traditional" method using EXPO, a computer program based on direct methods (Altomare *et al.*, 1999). The EXPO package consists of EXTRA and SIRPOW.92. In EXTRA, the whole powder pattern is decomposed to extract the intensities of individual reflections via the Le Bail algorithm (Le Bail *et al.*, 1988). The output from EXTRA serves as an input for SIRPOW.92, which then solves the structure by direct methods. A number of trial structures are generated by magic integer approach or by random phasing. The best model with the highest figure-of-merit is automatically chosen and processed through structure factor calculation, least-squares refinement and Fourier synthesis. The final solution is a set of the x, y, z coordinates with atomic species. Once most of the atomic positions are determined, a Rietveld structure refinement can be carried out using this structure as a starting model. The missing atoms can be located by examining a Fourier electron density difference map.

2.7 Rietveld Structure Refinement

The Rietveld method is based on a least-squares refinement analysis of powder diffraction data (Rietveld, 1969). This technique utilizes the entire powder pattern, unlike other profile-fitting methods. During the refinement, a number of parameters are varied so that the best match between the observed pattern and the calculated pattern is

obtained. Since it is a refinement procedure, the method requires a starting model which is close to the actual structure. In addition, it is necessary to start with reasonable values for profile parameters, such as the scale factor, the background function and the peak shape function.

The quantity which is minimized is defined as (Young, 1993):

$$R = \sum_i w_i (Y_{io} - Y_{ic})^2$$

where Y_{io} is observed intensity at step i, Y_{ic} is calculated intensity at i and w_i is weight factor at i. The calculated intensity Y_{ic} is defined by:

$$Y_{ic} = Y_{ib} + \sum_{k1}^{k2} G_{ik} I_{ik}$$

where Y_{ib} is the background intensity at i, G_{ik} is a normalized peak shape function, I_{ik} is the Bragg intensity, and k1..k2 are the reflections contributing intensity to i.

The background can be modelled as a polynomial function with various degrees or as a cosine Fourier series. It is imperative to depict accurately the peak shape of the profile in order to achieve a satisfactory refinement. The peak shape is described by a number of analytical functions. For a neutron diffraction profile, where the peaks are symmetric, the Gaussian function provides a good approximation of the peak shape. For X-ray, a convoluted function of Gaussian and Lorentzian is applied, such as the pseudo-Voigt and the Pearson VII functions. The peak width is usually expressed as the full width at half maximum (FWHM) as a function of tanθ (Caglioti *et al.*, 1958):

$$H^2 = U \tan^2\theta + V \tan\theta + W$$

where H is FWHM and U, V, W are refinable parameters.

The quality of the refinement result is indicated by several agreement factors of which the most meaningful are R_{wp} and S. The weighted pattern R index, R_{wp} is defined as:

$$R_{wp} = \left[\frac{\sum_i w_i (Y_{io} - Y_{ic})^2}{\sum_i w_i (Y_{io})^2} \right]^{1/2}$$

The final R_{wp} should ideally approach the statistically expected R value, R_{exp},

$$R_{e\,xp} = \left[\frac{(N-P)}{\sum_i w_i Y_{io}^{\ 2}} \right]^{1/2}$$

where N is the number of the observation and P is the degree of freedom.

The goodness-of-fit, χ^2, is then given as:

$$\chi^2 = \left[\frac{R_{wp}}{R_{e\,xp}} \right]^2$$

There are a number of computer software packages available for Rietveld refinement. In this work, FULLPROF (Roisnel & Rodriguez-Carvajal, 2001) and TOPAS2 (Bruker-AXS, 2000) were employed for structure refinements of both X-ray and neutron diffraction data.

2.8 Powder Neutron Diffraction

All powder neutron diffraction measurements were performed by Dr. Robert Hammond of the Neutron Program for Materials Research at the Chalk River Laboratories. The Dualspec C2 high-resolution powder diffractometer was used to obtain diffraction patterns. A schematic diagram of the experimental set-up is shown in Figure

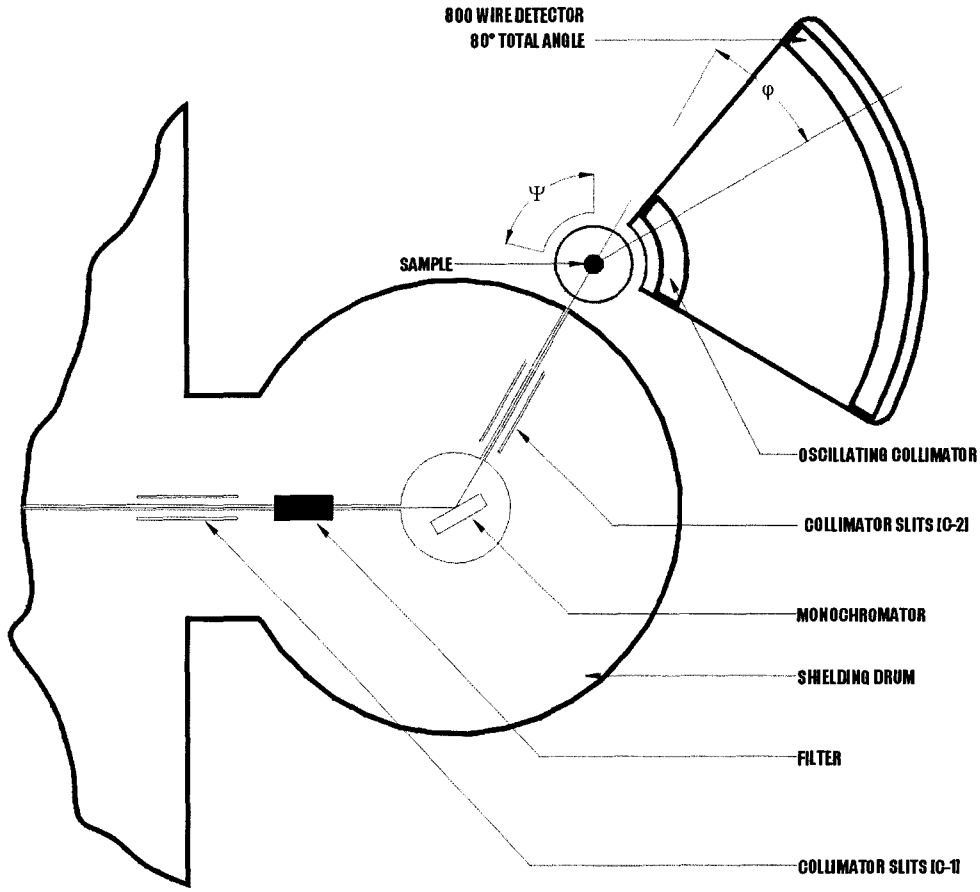

Figure 2.5 A schematic diagram of the C2 high resolution powder neutron diffractometer at Chalk River Laboratories

2.5. The instrument is equipped with a Si single crystal monochromator, which is rotated to give (5 3 1) orientation to achieve a wavelength of 1.324 Å with take-off angle of 92.7°. For *in-situ* diffraction measurements at high temperatures, the sample was placed in the F3 furnace with tungsten carbide heating elements. A thermocouple was attached to the vanadium sample container to monitor the temperature of the sample. A curved 800-wire BF_3 position-sensitive detector was used to record the diffracted beams. The wire spacing of the detector is 0.1°, which enables the simultaneous measurement of 80° of scattering angle. Therefore, two sets of data were collected over 2θ ranges of 5.0° - 83.9° and 30.0° - 116.9°, and they were merged into one data set for a Rietveld refinement. The samples for powder neutron diffraction were prepared with ^{11}B-enriched boric acid (99.27 at. %) in order to prevent the strong absorption of neutrons by the ^{10}B nuclei.

2.9 Bond Valence Analysis

Before the development of the bond valence model, it was often difficult to obtain satisfactory accounts of the bonding and structure of non-molecular inorganic compounds without referring to more than one theory, whereas most organic structures could be readily rationalized by well-developed valence models. The bond valence model is a very useful tool to describe the bonds and their strengths in inorganic solids (Brown & Shannon, 1973; Brown, 1978; Brown, 1981). It is now widely applied as a check on the reliability of a determined structure.

The bond valence model is based on Pauling's electrostatic valence rule for ionic compounds (Pauling, 1928). Pauling's 2nd rule is modified so that the electrostatic bond

strength and the formal charge of an atom are replaced by the bond valence and the valence of that atom, respectively. The valence of a bond between atoms i and j is defined by:

$$V_i = \sum_j s_{ij}$$

where V_i is the valence of the atom i and is equivalent to the formal oxidation state of i, and s_{ij} is the bond valence between i and j. This relation, called the valence sum rule, thus indicates that the valence of an atom i must be equal to the sum of bond valences for all bonds that i forms with. It has been shown experimentally that there is an inverse relationship between the bond valence and the bond length of a given pair of elements. The most commonly used expression is given by Brown and Altermatt (1985):

$$s_{ij} = \exp\left[\frac{(r_o - r_{ij})}{b}\right]$$

where r_o is the bond valence parameter, r_{ij} is the bond length of i – j, and b is a constant, universally taken as 0.37 Å. The values of bond valence parameters have been derived empirically and tabulated according to the type of the anion that the central cation bonds with (Brese & O'Keefe, 1991).

The bond valence model provides an excellent prediction and understanding of crystal structures of inorganic solids in terms of bond lengths and strengths. As the model treats each bond individually, distortions and irregularity in a cation coordination environment can be explained. It can be also applied to analyze different oxidation states and to identify correct atomic positions. In this thesis, the bond valence analysis has been applied to confirm the validity of the structures determined from powder X-ray

diffraction methods. It was also found to be very useful to understand the strains and distortions present in the various borate structures discussed in this work.

Chapter 3

SYNTHESIS AND STRUCTURE OF $PbMBO_4$ (M = Cr, Mn, Fe, Ga)

3.1 Introduction

This chapter is focused on the studies of the PbO – M_2O_3 – B_2O_3 systems (M = Cr, Mn, Fe, Ga). Although there have been numerous investigations of the binary PbO – B_2O_3 system (McMurdie, 1941; Krogh-Moe & Wold-Hansen, 1973), a survey of inorganic databases indicates that no ternary lead borates have been yet reported (ICSD, 2001; PC-PDF, 1999). Four new compounds, $PbMBO_4$, have been discovered, and the details of their syntheses and structural characterizations are presented in this chapter.

3.2 Sample preparation

3.2.1. Solid-State Syntheses

a) $PbGaBO_4$

The compound was synthesized from a stoichiometric mixture of PbO, Ga_2O_3 and H_3BO_3 powders. A small pellet of 0.50-g was initially fired slowly (1°C min^{-1}) up to 500°C to dehydrate H_3BO_3, then the sample was heated up to 800°C, since the compound starts to melt incongruently at 825°C. The mixing and firing steps were repeated until no further reaction was observed by powder X-ray diffraction. The final product consisted of a well-crystallized, white-coloured $PbGaBO_4$ powder. The following equation describes the reaction involved to prepare $PbGaBO_4$:

$$2PbO + Ga_2O_3 + 2H_3BO_3 \rightarrow 2PbGaBO_4 + 3H_2O$$

b) $PbFeBO_4$

The polycrystalline compound was prepared by heating a stoichiometric mixture of PbO and $FeBO_3$ powders at 700°C for 3 days with daily remixings. Calcite-type $FeBO_3$ was easily made by heating appropriate amounts of Fe_2O_3 and H_3BO_3 powders at 700°C (Joubert *et al.*, 1968). It was necessary to use the pre-reacted $FeBO_3$ compound in order to avoid the formation of $Pb_2B_2O_5$, which melts at 497°C (McMurdie, 1941), resulting in the formation of glass before the desired reaction takes place. Dark green-coloured $PbFeBO_4$ powders were obtained as a final product. The reactions are summarized as follows:

$$Fe_2O_3 + 2H_3BO_3 \rightarrow 2FeBO_3 + 3H_2O$$

$$PbO + FeBO_3 \rightarrow PbFeBO_4$$

c) $PbCrBO_4$

As in the case of $PbFeBO_4$, the compound was obtained by heating stoichiometric quantities of PbO and pre-reacted $CrBO_3$ powders. $CrBO_3$ was prepared from firing stoichiometric amounts of Cr_2O_3 and H_3BO_3 at 850°C in air for 4 days. The formation of the compound was confirmed by comparing its powder X-ray diffraction pattern with that calculated from the single crystal X-ray data for $CrBO_3$ (Tombs *et al.*, 1963). The Cr_2O_3 compound was obtained by heating $Cr(NO_3)_3 \cdot 9H_2O$ powder gently on a hot plate, followed by firing it at 800°C for 1 day. Its purity was checked by powder X-ray diffraction. The equations below show the synthesis of $CrBO_3$.

$$2Cr(NO_3)_3.9H_2O \rightarrow Cr_2O_3 + 3N_2O_5 + 9H_2O$$

$$Cr_2O_3 + 2H_3BO_3 \rightarrow 2CrBO_3 + 3H_2O$$

A 0.5-g pellet of PbO and $CrBO_3$ was heated at 850°C for 3 days under flowing high-purity argon in order to prevent the oxidation of Cr^{3+} to Cr^{6+} and the formation of $PbCrO_4$. The sample was re-mixed and re-pelletized daily. The $PbCrBO_4$ compound was obtained as a dark green powder.

$$PbO + CrBO_3 \xrightarrow{Ar} PbCrBO_4$$

d) $PbMnBO_4$

The synthesis of $PbMnBO_4$ was carried out by reacting PbO and a pre-reacted Mn_2O_3 - $2H_3BO_3$ mixture. The Mn_2O_3 compound was prepared by reducing MnO_2 in air at 800°C for 1 day, and its purity was checked by powder X-ray diffraction. When the 1:2 molar ratio mixture of Mn_2O_3 and H_3BO_3 was heated at 700°C, no formation of $MnBO_3$ was observed; the only crystalline species formed was Mn_2BO_4, as indicated in the literature (Norrestam *et al.*, 1995). A 0.50-g pellet of PbO and "$MnBO_3$" (i.e. $Mn_2BO_4 + 1/2B_2O_3$) was heated at 800°C in air for 4 days with intermediate re-mixings. The final product was a red-brown powder of $PbMnBO_4$. The preparation of $PbMnBO_4$ is summarized by the following reactions:

$$2MnO_2 \rightarrow Mn_2O_3 + 1/2O_2$$

$$Mn_2O_3 + 2H_3BO_3 \rightarrow \text{“}2MnBO_3\text{”}\ (Mn_2BO_4 + 1/2B_2O_3) + 3H_2O$$

$$PbO + \text{“}MnBO_3\text{”} \rightarrow PbMnBO_4$$

3.2.2. Single Crystal Growth

Crystal growth experiments of the $PbMBO_4$ (M = Mn, Fe, Ga) compounds were carried out by slow-cooling of melts using excess PbO as a flux. A 10.0 – 12.0 g mixture with a composition $4PbO\text{-}M_2O_3\text{-}2H_3BO_3$ was melted in a covered platinum crucible at 900 - 1000°C. The melt was kept at this temperature for approximately 2 – 3 hours to ensure homogeneity, and was then cooled down slowly to 500°C at a rate of 3°C hr^{-1}. The exact conditions of each experiment are given in Table 3.1. Transparent, prismatic sub-millimeter sized crystals of $PbMBO_4$ were separated from the matrix by dissolving unreacted PbO in 1.0 M aqueous HNO_3 at room temperature. A photograph of the crystals is shown in Figure 3.1. In the case of $PbMnBO_4$, a small amount of black, needle-shaped crystals of $Pb_3Mn_7O_{15}$ (Darriet *et al.*, 1978; LePage & Calvert, 1984) was also obtained.

The single crystal growth of $PbCrBO_4$ was not attempted since the experimental conditions require an inert atmosphere throughout the whole crystal growth in order to prevent the oxidation of Cr^{3+} to Cr^{6+}.

Table 3.1: Crystal growth conditions and crystal colours of $PbMBO_4$ (M = Ga, Fe, Mn)

Compound	Weight of starting materials	Crystal growth temperature (°C)	Crystal colour
$PbMnBO_4$	9.123 g PbO 1.613 g Mn_2O_3 1.264 g H_3BO_3 (total 12.000 g)	1000 – 500	Dark red
$PbFeBO_4$	9.109 g PbO 1.629 g Fe_2O_3 1.262 g H_3BO_3 (total 12.000 g)	900 – 500	Dark green
$PbGaBO_4$	7.416 g PbO 1.557 g Ga_2O_3 1.027 g H_3BO_3 (total 10.000 g)	900 – 500	Colourless

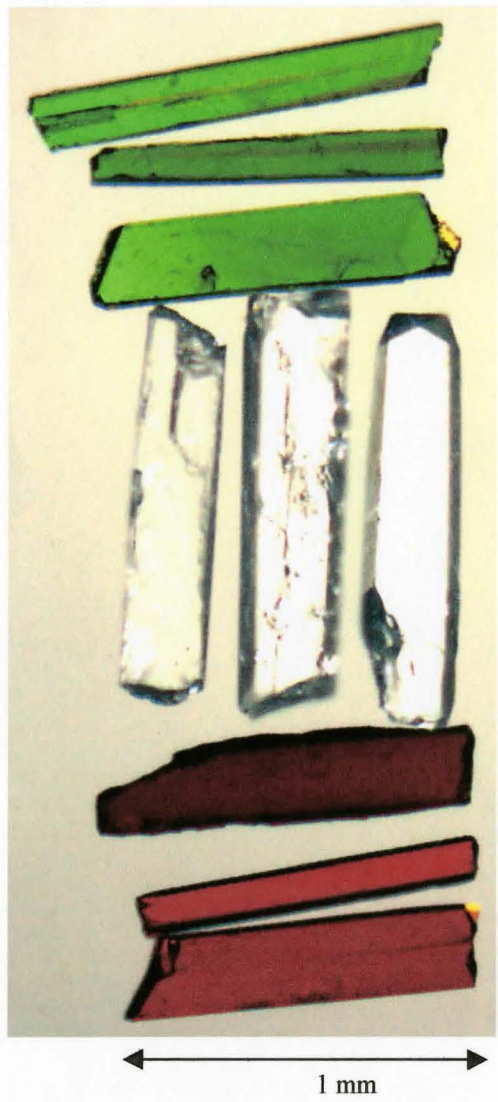

Figure 3.1 Photograph of $PbFeBO_4$ (green), $PbGaBO_4$ (colourless) and $PbMnBO_4$ (red) crystals grown from a PbO flux

3.3 Structure Determination and Refinement

3.3.1 $PbMBO_4$ (M = Mn, Fe, Ga)

The structures of $PbGaBO_4$, $PbFeBO_4$ and $PbMnBO_4$ were determined by single crystal X-ray diffraction. The details of the data collection and refinements are given in Table 3.2. Prior to the single crystal data collection, the unit-cell dimensions of these compounds were determined using powder X-ray data recorded with a Guinier-Hägg camera.

The raw intensity data were corrected for Lorentz and polarization effects with the computer software SAINT (Siemens, 1996), and the absorption correction was applied by using the program SADABS (Sheldrick, 2001) or by indexing the crystal faces. The observed systematic absences $k + l = 2n + 1$ in $0kl$ and $h = 2n + 1$ in $hk0$ corresponded to the Pnma or $Pn2_1a$ space group. Both space groups were used to solve the structure, however attempts to refine the structures based on the non-centrosymmetric space group $Pna2_1$ led to a poor convergence with non-positive definite values of atomic displacement parameters. The structure solutions were carried out by direct methods to locate the positions of Pb, M and O atoms with the computer software SHELXS (Sheldrick, 1997). The position of boron atoms was determined by calculating subsequent Fourier difference maps. The structural model was then fully refined with extinction coefficients and anisotropic displacement parameters, U_{ij}. For all three structures, the maximum and minimum peaks in the residual electron density maps are located near Pb sites (Table 3.2). The crystal data for $PbMBO_4$ are shown in Table 3.3. The atomic coordinates are listed in Table 3.4, and the anisotropic displacement parameters are given in Table 3.5.

Table 3.2 Details of structure refinements (single crystal)

	$PbGaBO_4$	$PbFeBO_4$	$PbMnBO_4$
Wavelength	MoKα	MoKα	MoKα
Absorption coefficient (mm^{-1})	57.22	52.48	52.33
2θ max (°)	90.72	73.74	66.26
Index ranges	$-14 < h < 11$ $-7 < k < 11$ $-16 < l < 15$	$-10 < h < 11$ $-8 < k < 9$ $-13 < l < 11$	$-10 < h < 10$ $-9 < k < 7$ $-12 < l < 13$
Unique reflections	1493	900	690
Absorption correction	SADABS	Face-indexing	Face-indexing
Transmission min and max	0.016, 0.101	0.055, 0.365	0.013, 0.091
R_{int}	0.042	0.071	0.068
Refined parameters	41	41	41
Goodness-of-fit	1.136	1.088	1.210
R [$F > 4\sigma(F)$]	0.028 (for 1336 reflections)	0.026 (for 800 reflections)	0.022 (for 674 reflections)
$wR(F^2)$	0.066	0.062	0.054
Difference map ($eÅ^{-3}$)	5.73 (0.56Å from Pb) -6.70 (0.84 Å from Pb)	4.17 (0.69 Å from Pb) -2.30 (0.55 Å from Pb)	2.53 (0.58 Å from Pb) -2.33 (0.75 Å from Pb)

Details of structure refinement (powder)

	$PbCrBO_4$
Wavelength (Å)	CuKα
2θ range (°)	10.00 – 96.50
Stepsize (°)	0.03
Counting time	13 seconds/step
R_p	0.158
R_{wp}	0.201
R_{exp}	0.116
R_{Bragg}	0.049
χ^2	3.03
preferred orientation	1.027(4) for (110) direction
Number of reflections	347
Refined parameters	33

Table 3.3 Crystal data for $PbMBO_4$

	α-Al*	Cr	Ga	Fe	Mn
Unit cell (Å)					
a	6.9209(5)	6.9860(3)	6.9944(10)	7.0089(14)	6.7062(9)
b	5.7134(4)	5.9398(2)	5.8925(8)	5.9412(12)	5.9429(8)
c	8.0215(6)	8.1149(3)	8.2495(11)	8.3339(17)	8.6418(11)
Volume ($Å^3$)	317.19	336.73	340.00	347.03	344.41
Calc. density ($g\ cm^{-3}$)	6.473	6.588	6.871	6.466	6.498
r (M^{3+} for CN = 6, Å; Shannon, 1976)	0.675	0.755	0.760	0.785 (high spin)	0.785 (high spin)

*α-$PbAlBO_4$ is discussed in Chapter 4.

Table 3.4 Atomic coordinates and isotropic displacement parameters of $PbMBO_4$

$PbCrBO_4$*

	x	y	z	B ($Å^2$)
Pb	0.0623(3)	1/4	0.3644(2)	1.9(4)
Cr	0	0	0	1.6(4)
B	-0.205(8)	1/4	-0.261(7)	1.0**
O1	0.109(3)	-1/4	-0.118(3)	1.3(7)
O2	0.173(2)	-0.053(3)	0.196(2)	1.0(6)
O3	-0.170(3)	-1/4	0.097(3)	1.6(7)

* Rietveld refinement of powder X-ray data
** Fixed at 1.0 $Å^2$ during the refinement

$PbMnBO_4$

	x	y	z	U_{eq} ($Å^2$)
Pb	0.03542(4)	1/4	0.35174(3)	0.0126(1)
Mn	0	0	0	0.0082(2)
B	-0.2089(9)	1/4	-0.2611(8)	0.010(1)
O1	0.1090(7)	-1/4	-0.1043(6)	0.0101(7)
O2	0.1681(5)	-0.0463(5)	0.1871(4)	0.0128(6)
O3	-0.2160(8)	-1/4	0.0929(6)	0.0133(8)

$PbFeBO_4$

	x	y	z	U_{eq} ($Å^2$)
Pb	0.05624(4)	1/4	0.35702(3)	0.0105(1)
Fe	0	0	0	0.0040(2)
B	-0.2200(11)	1/4	-0.2657(9)	0.009(1)
O1	0.1071(8)	-1/4	-0.1155(6)	0.0077(8)
O2	0.1697(6)	-0.0494(6)	0.1950(4)	0.0122(7)
O3	-0.1820(8)	-1/4	0.0894(6)	0.0107(9)

$PbGaBO_4$

	x	y	z	U_{eq} ($Å^2$)
Pb	0.06200(2)	1/4	0.35878(2)	0.00640(5)
Ga	0	0	0	0.00398(8)
B	-0.2237(7)	1/4	-0.2639(6)	0.0036(6)
O1	0.1013(5)	-1/4	-0.1146(4)	0.0041(4)
O2	0.1717(4)	-0.0466(4)	0.1922	0.0073(3)
O3	-0.1783(5)	-1/4	0.0921(4)	0.0069(5)

Table 3.5 Anisotropic displacement parameters ($Å^2$) for $PbMBO_4$ (M = Mn, Fe, Ga)

$PbMnBO_4$

	U_{11}	U_{22}	U_{33}	U_{23}	U_{13}	U_{12}
Pb	0.0137(2)	0.0160(2)	0.0081(2)	0	0.00054(7)	0
Mn	0.0088(3)	0.0081(3)	0.0077(4)	-0.009(3)	-0.0011(3)	0.0009(3)
B	0.006(3)	0.013(2)	0.010(3)	0	0.001(2)	0
O1	0.009(2)	0.011(2)	0.011(2)	0	0.001(2)	0
O2	0.017(1)	0.010(1)	0.011(1)	0.000(1)	-0.005(1)	0.001(1)
O3	0.014(2)	0.015(2)	0.011(2)	0	0.004(1)	0

$PbFeBO_4$

	U_{11}	U_{22}	U_{33}	U_{23}	U_{13}	U_{12}
Pb	0.0116(1)	0.0132(1)	0.0067(1)	0	0.00081(8)	0
Fe	0.0058(4)	0.0029(3)	0.0033(3)	-0.0009(3)	-0.0009(3)	0.0008(3)
B	0.011(3)	0.009(3)	0.007(3)	0	-0.001(2)	0
O1	0.008(2)	0.008(2)	0.007(2)	0	-0.002(2)	0
O2	0.016(1)	0.009(1)	0.010(1)	0.000(1)	-0.006(1)	0.003(1)
O3	0.014(2)	0.010(2)	0.008(2)	0	0.006(2)	0

$PbGaBO_4$

	U_{11}	U_{22}	U_{33}	U_{23}	U_{13}	U_{12}
Pb	0.00665(7)	0.00891(7)	0.00364(7)	0	0.00060(4)	0
Ga	0.0050(2)	0.0033(1)	0.0037(2)	-0.0009(1)	-0.0007(1)	0.0009(1)
B	0.003(1)	0.004(1)	0.003(2)	0	-0.001(1)	0
O1	0.0025(9)	0.0038(9)	0.006(1)	0	0.0005(8)	0
O2	0.0103(9)	0.0052(7)	0.0064(9)	-0.0001(6)	-0.0051(7)	0.0016(7)
O3	0.009(1)	0.007(1)	0.005(1)	0	0.004(1)	0

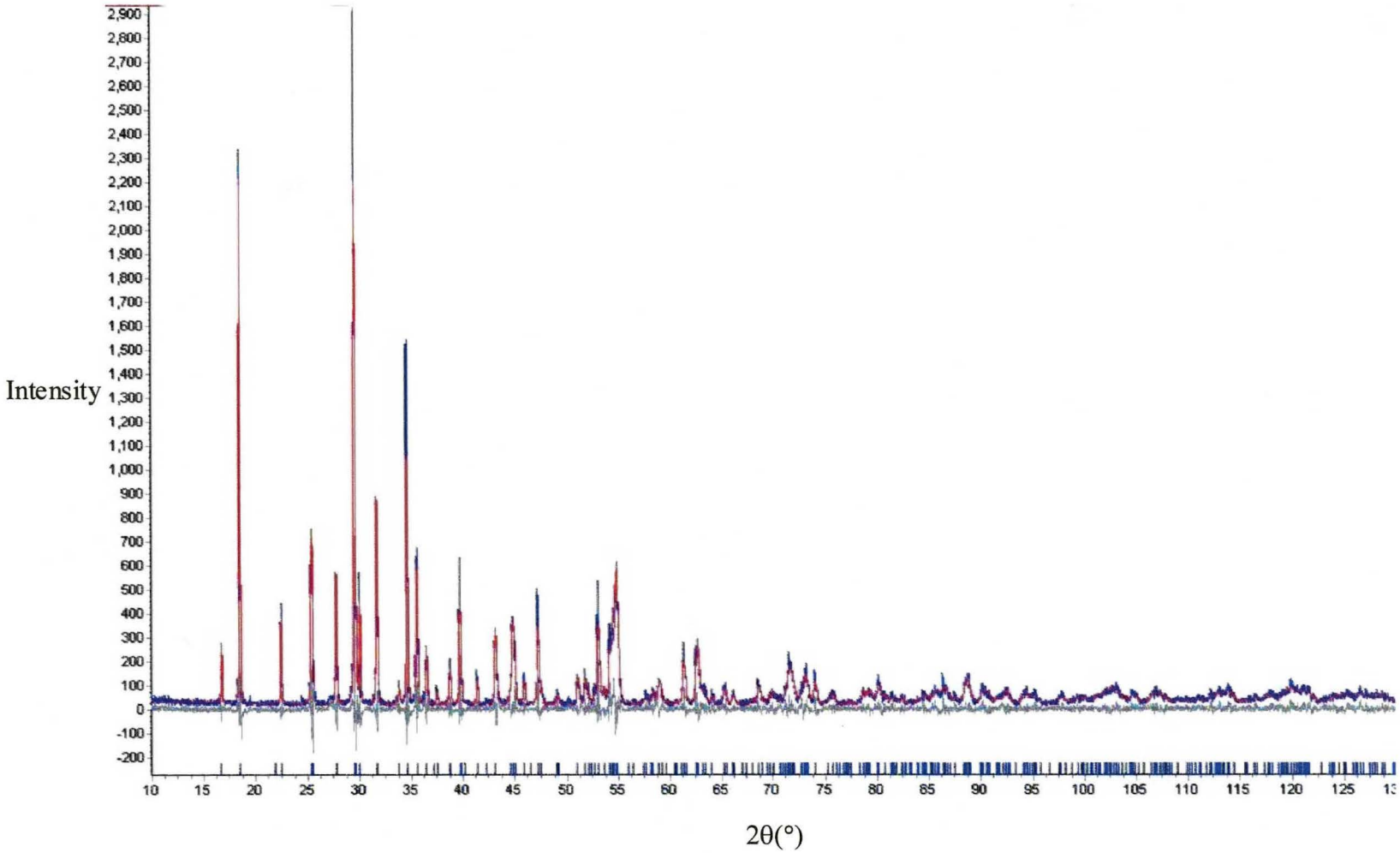

Figure 3.2 Observed (blue) and calculated (red) profiles for the Rietveld refinement of $PbCrBO_4$. The difference between the observed and the calculated is plotted as a gray line below the profiles. The vertical bars depict the Bragg peak positions.

3.3.2. $PbCrBO_4$

For $PbCrBO_4$, powder X-ray diffraction data were collected using a Bruker D8 diffractometer with CuKα radiation. The Rietveld refinement was carried out using the structural parameters of $PbGaBO_4$ as a starting model with the computer program TOPAS2 (Bruker-AXS, 2000). A total of 33 parameters were refined including 19 structural parameters, 13 profile parameters and one parameter for a weak (110) preferred orientation. A pseudo-Voigt function was chosen to describe the peak shape and the background was estimated by a 5^{th} order Chevychev polynomial. All the isotropic displacement parameters, B, were refined except that for the boron atom for which it was fixed at 1.0 $Å^2$. During the refinement, the three B – O bond lengths were constrained to be equal to 1.35 Å in order to keep a regular triangular coordination environment around the B atoms. The final refinement details are given in Table 3.2. The crystal data for $PbCrBO_4$ are given in Table 3.3. The atomic coordinates and isotropic displacement parameters are listed in Table 3.4. The plot of the calculated and the observed profiles is shown in Figure 3.2.

3.4 Description of the $PbMBO_4$ Structure

The crystal data of all four $PbMBO_4$ compounds are listed in Table 3.2. Selected bond distances and bond valence sums are given in Table 3.6, and selected bond angles are listed in Table 3.7. The $PbMBO_4$ structure is described in Figures 3.3 and 3.4.

All four $PbMBO_4$ compounds are isostructural. Their structure is based on a distorted octahedral coordination of M, a regular trigonal planar coordination of B and the expected four-fold square pyramidal geometry around the Pb^{2+} ion with a stereoactive

Table 3.6 Selected bond distances and valences in $PbMBO_4$

Dist (Å)	$PbCrBO_4$*		$PbMnBO_4$		$PbFeBO_4$		$PbGaBO_4$	
		s		s		s		s
Pb – O1	2.33(2)	0.55	2.347(5)	0.530	2.316(6)	0.576	2.316(4)	0.576
Pb – O1	2.35(2)	0.53	2.414(5)	0.442	2.370(6)	0.498	2.365(3)	0.505
Pb – O2 x2	2.37(2)	0.50	2.433(3)	0.420	2.370(4)	0.498	2.352(2)	0.523
	Σs	**2.1**	**Σs**	**1.79**	**Σs**	**2.07**	**Σs**	**2.13**
M – O1 x2	1.89(2)	0.64	1.885(3)	0.713	1.923(3)	0.643	1.888(1)	0.652
M – O2 x2	1.99(2)	0.49	1.990(3)	0.537	2.035(4)	0.474	2.008(2)	0.472
M – O3 x2	2.11(2)	0.35	2.225(4)	0.285	2.095(4)	0.403	2.074(2)	0.395
	Σs	**3.0**	**Σs**	**3.07**	**Σs**	**3.04**	**Σs**	**3.04**
B – O2 x2	1.34(2)	1.09	1.396(5)	0.935	1.376(5)	0.987	1.385(2)	0.963
B – O3	1.36(6)	1.03	1.358(8)	1.036	1.389(9)	0.953	1.372(6)	0.997
	Σs	**3.2**	**Σs**	**2.91**	**Σs**	**2.93**	**Σs**	**2.92**
O1 – Pb	2.33(2)	0.55	2.347(5)	0.530	2.316(6)	0.576	2.316(4)	0.576
Pb	2.35(2)	0.53	2.414(5)	0.442	2.370(6)	0.498	2.365(3)	0.505
M x2	1.89(2)	0.64	1.990(3)	0.713	1.923(3)	0.643	1.888(1)	0.652
	Σs	**2.4**	**Σs**	**2.40**	**Σs**	2.36	**Σs**	**2.39**
O2 – Pb	2.37(2)	0.50	2.433(3)	0.420	2.370(4)	0.498	2.352(2)	0.523
M	1.99(2)	0.49	1.990(3)	0.537	2.035(4)	0.474	2.008(2)	0.472
B	1.34(2)	1.09	1.396(5)	0.935	1.376(5)	0.987	1.385(2)	0.963
	Σs	**2.1**	**Σs**	**1.89**	**Σs**	**1.96**	**Σs**	**1.96**
O3 – M x2	2.11(2)	0.35	2.225(4)	0.285	2.095(4)	0.403	2.074(2)	0.395
B	1.36(6)	1.03	1.358(8)	1.036	1.389(9)	0.953	1.372(6)	0.997
	Σs	**1.7**	**Σs**	**1.61**	**Σs**	**1.76**	**Σs**	**1.76**

* From Rietveld refinement of powder X-ray diffraction data

Table 3.7 Selected bond angles (°) in $PbMBO_4$

	$PbCrBO_4$*	$PbMnBO_4$	$PbFeBO_4$	$PbGaBO_4$
O1 – M – O1	180(1)	180.0(3)	180.0(4)	180.0(3)
O1 – M – O2	93(1)	93.5(2)	93.4(2)	93.7(1)
O1 – M – O2	87(1)	86.6(2)	86.6(2)	86.3(1)
O1 – M – O3	82(1)	84.2(1)	82.4(1)	81.7(1)
O1 – M – O3	98.0(7)	95.8(1)	97.6(2)	98.4(1)
O2 – M – O2	180(2)	180.0(1)	180.0(2)	180.0(1)
O2 – M – O3	86(1)	89.0(2)	88.3(2)	88.5(1)
O2 – M – O3	94(1)	91.0(2)	91.8(2)	91.5(1)
O3 – M – O3	180(1)	180.0(1)	180.0(2)	180.0(1)
M – O1 – M	103	104	101	103
M – O3 – M	89	84	90	90
O2 – B – O2	125(3)	120.2(5)	120.1(6)	119.8(4)
O2 – B – O3	117(3)	119.9(3)	119.9(3)	120.1(2)
Dihedral angles				
O2 – O1 – O2	50	51	49	50
O2 – O3 – O2	50	48	49	50
O2 – O3 – O2	73	72	74	73
O2 – O1 – O2	83	83	82	82

* Larger esd's are attributed to the refinement of powder X-ray data

lone pair. The structure consists of infinite chains of edge-sharing MO_6 octahedra parallel to the b-axis. These compounds, formulated as orthoborates, $PbM(BO_3)O$, represent a new structure-type for the family of anhydrous borates, based on recent reviews of known borate structures (Heller, 1986; Grice *et al.*, 1999). However, the $PbMBO_4$ structure shows some similarities with the well-known rutile structure-type (TiO_2). Like the $PbMBO_4$ structure, the rutile structure is built of chains of edge-sharing TiO_6 octahedra along the [001] direction. One notable structural difference between $PbMBO_4$ and rutile corresponds to the bridging of the octahedral chains. In rutile, adjacent chains are linked by their corners to create a three-dimensional framework, whereas, in $PbMBO_4$, BO_3 triangles bridge the neighbouring chains. Moreover, the $PbMBO_4$ structure still retains a strong one-dimensional character.

As illustrated by the M – O bond lengths and O – M – O bond angles (Tables 3.6 and 3.7), all $PbMBO_4$ structures display strong distortions in the MO_6 octahedra with two short M – O1 and two long M – O3 bonds. These distortions can be understood in terms of the coordination environment around the O1 and O3 atoms. The four-coordinated O1 atom (2Pb + 2M) receives no bonding contributions from the B atom, therefore the M – O1 bonds are shorter and stronger. However, the M – O3 bonds are longer and weaker since the three-coordinated O3 (2M + B) atom is bonded to B to form strong B – O bonds. The variations in M – O bond lengths are even more prominent in $PbMnBO_4$ due to the Jahn-Teller effect associated with the presence of the high-spin Mn^{3+} ions with d^4 configuration in octahedral coordination. As a result, the MnO_6 octahedra are significantly distorted with two much longer Mn – O3 lengths of 2.23 Å, and Mn – O – Mn angles deviate from the ideal 90.0°, to give 83.8° and 104.1°. The bonding

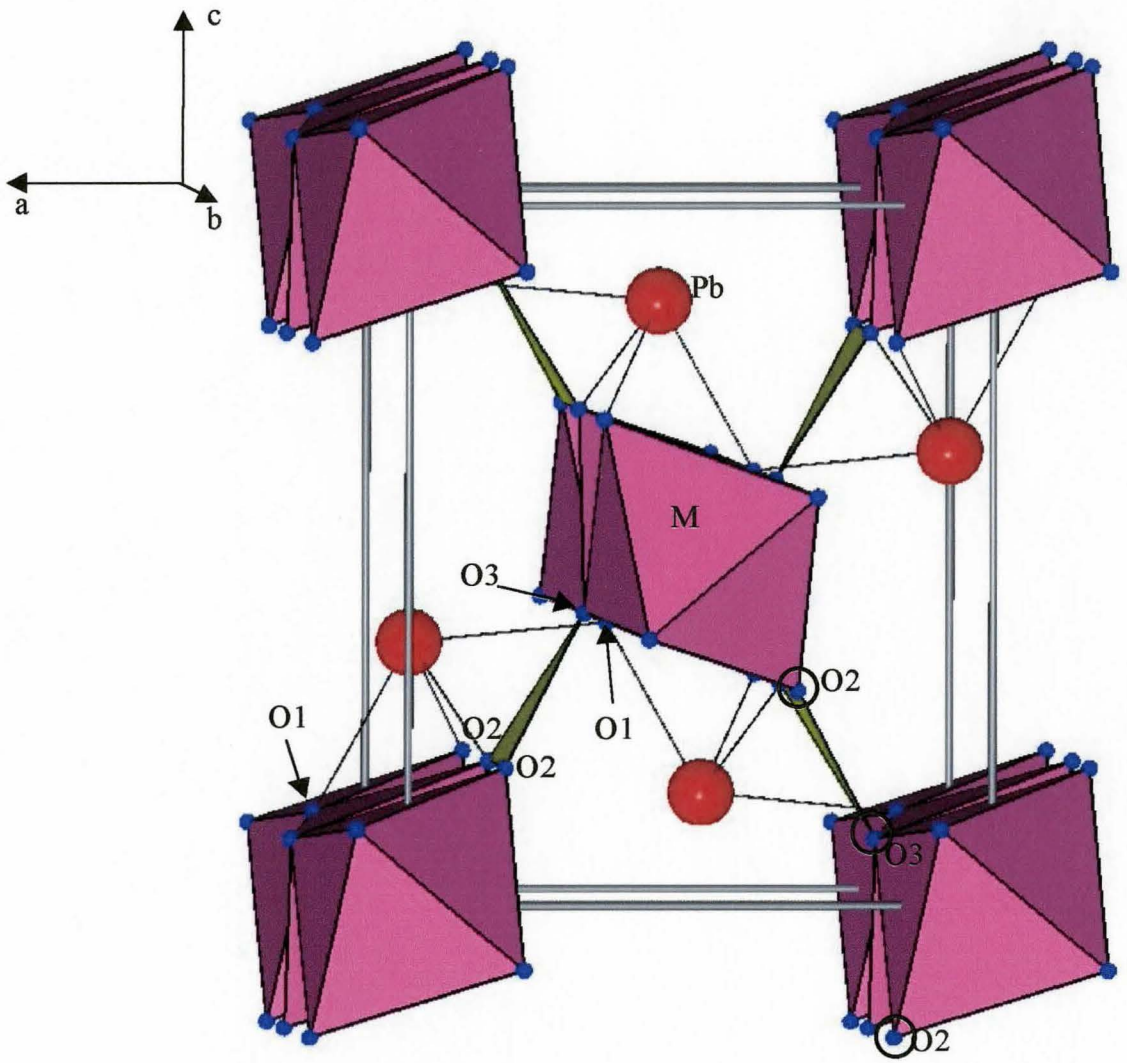

Figure 3.3 Crystal structure of $PbMBO_4$ viewed approximately along the [010] direction. Pb^{2+} cations, depicted by red circles, show 4-fold coordination. Purple MO_6 octahedral chains are bridged by yellow BO_3 triangles.

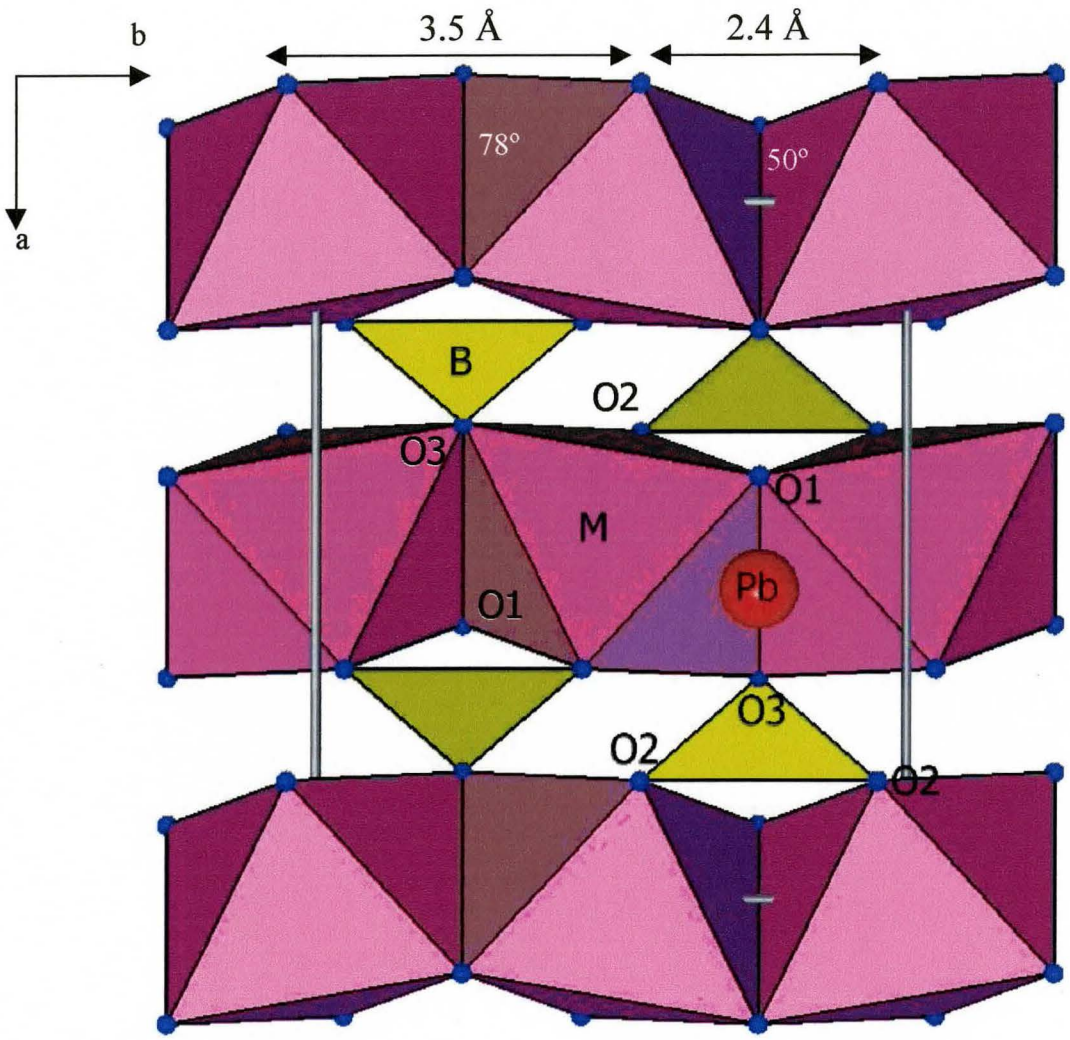

Figure 3.4 Structure of $PbMBO_4$ viewed along the c-axis. Strong angular distortions along the MO_6 chains caused by the briding BO_3 triangles are observed.

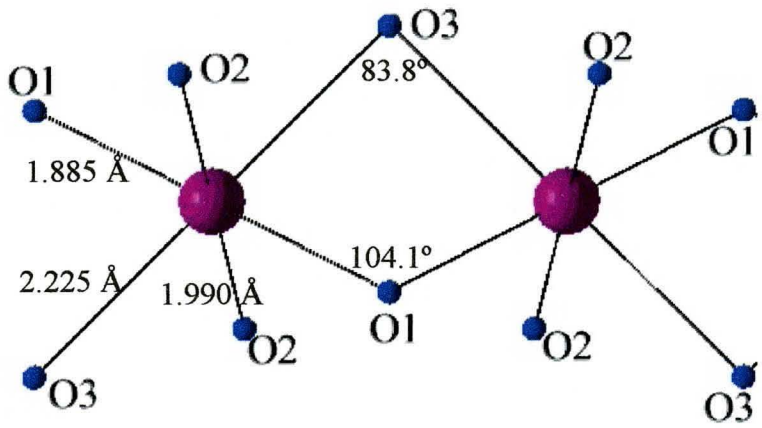

Figure 3.5 Bonding environment around the Mn^{3+} ion in $PbMnBO_4$. Due to the Jahn-Teller effect, the MnO_6 octahedra are strongly distorted.

environment around the Mn^{3+} ion in $PbMnBO_4$ is depicted in Figure 3.5. Nevertheless, the bond valence analysis around the Mn^{3+} ion gives an adequate sum of 3.07. The distorted geometry of the MnO_6 octahedra affects the unit-cell dimensions of the compound. The dimension along the a-axis is much shorter while that along the c-axis is larger than the other $PbMBO_4$ compounds. A low bond-valence sum (Brese and O'Keefe, 1991) around the Pb^{2+} ion in $PbMnBO_4$ indicates that it is somewhat under-bonded (Σs = 1.79) compared to the $PbFeBO_4$ structure (Table 3.6). This can be ascribed mostly to the stretching of the Pb – O1 and Pb – O2 bonds as a result of the Jahn-Teller distortion of the MnO_6 octahedra which leads to the contraction of the Mn – O1 and Mn – O2 bonds.

The presence of short and strong B – O bonds in the BO_3 groups leads to a buckling along the octahedral chains in all $PbMBO_4$ compounds, since the borate groups bridge adjacent octahedra along the chains (Figure 3.4). In order to provide a regular triangular coordination environment around B, the octahedral chains need to be tilted such that the dihedral angles between two adjacent MO_6 octahedra considerably deviate from the ideal value of 60° with values of 49.8 – 50.9° and 71.6 – 82.9°. In other words, the apical oxygens (O2) of two adjacent MO_6 octahedra which are bonded to the B atom are brought closer together (O2 ··· O2 distance = 2.39 to 2.43 Å) whereas those bonded to Pb are moved further apart (O2 ··· O2 distance = 3.50 to 3.60 Å).

The variations in the bond valence sums around the oxygen atoms in the $PbMBO_4$ structure suggest the presence of structural strain. A large bond valence sum (Σs = 2.3 to 2.4) around the 4-coordinated O1 atom (2Pb + 2M) indicates that it is over-bonded due to two short M – O1 bonds (1.89 to 1.92 Å; Table 3.6). In contrast, the three-coordinated O3 atom (2M + B) is under-bonded (Σs = 1.7) because of long M – O3 bonds (2.07 to

2.22 Å). However, the O2 atoms, bonded to Pb, M and B, achieve satisfactory bond valence sums ranging from 1.9 to 2.1. All M atoms also attain the expected bond valence sums of 3.0 due to the averaging of M – O lengths.

The unit-cell volumes of the $PbMBO_4$ compounds increase with the size of the M^{3+} cation (Table 3.3). The expansion of the unit-cell is highly anisotropic with the most pronounced increase occurring along the c-axis ($\Delta c / c = 3.7$ %). On the other hand, the a-axis remains nearly constant throughout the whole series, except in $PbMnBO_4$, where it actually contracts due to the Jahn-Teller distortion. It is not simple to relate the unit-cell expansion with a particular bond length or bond angle since the effect appears to be a combination of various geometrical changes. However, it is noted that the O3 – O2 – O3 angle (shown in circles in Figure 3.3) becomes slightly larger (151° - 158°, from $PbAlBO_4$ to $PbFeBO_4$) with increasing size of the M^{3+} ion. This indicates that the position of the planar BO_3 group becomes more parallel to the c-axis as the volume of the MO_6 octahedra increases, contributing to the expansion of the c-axis as well as to the reduction of the a-axis. This trend is also observed in the α-$PbAlBO_4$ structure at high temperatures (cf. Chapter 4). In this case, the expansion of the unit-cell volume is caused by the expansion of the c-axis with the increasing temperatures.

Attempts to prepare Sc, Y and In analogues of the $PbMBO_4$ compounds via solid-state reactions have been unsuccessful due to the melting of the samples at 700 - 750°C, without the formation of any ternary compounds. These results suggest that the ionic radius of M^{3+} may play an important role in determining the stability of a $PbMBO_4$ compound, since the Sc^{3+}, Y^{3+} and In^{3+} ions (0.885 Å, 1.040 Å and 0.940 Å, respectively; Shannon, 1976) are significantly larger than Fe^{3+} or Mn^{3+} (0.785 Å for high-spin). The

size limit for the M^{3+} ion in the octahedral environment may be understood by considering geometrical constraints imposed by the bridging BO_3 groups. The expansion of M – O distances, and thus, the enlargement of the MO_6 octahedra may not be able to provide appropriate triangular coordinations around the B atoms with B – O lengths of approximately 1.36 Å, even with a strong buckling of the octahedral chains.

In spite of the more appropriate size of the Ti^{3+} cation (0.81 Å), it was not possible to prepare a Ti-analogue of the $PbMBO_4$ compounds because of the internal redox reaction between Pb^{2+} and Ti^{3+}. When a PbO – $TiBO_3$ mixture was reacted at 750°C under argon, Pb^{2+} was partially reduced to give Pb metal while Ti^{3+} was oxidized to Ti^{4+} to form $PbTiO_3$.

The uniqueness of the $PbMBO_4$ structure may be associated with the stereochemistry of the Pb^{2+} cation with a lone pair. The syntheses of the solid-solutions $Pb_{1-x}Sr_xGaBO_4$ and $Pb_{1-x}Ba_xGaBO_4$ (x = 0.1, 0.15 and 0.2) were attempted by firing stoichiometric mixtures of $SrCO_3$ (or $BaCO_3$), PbO, Ga_2O_3 and H_3BO_3 at 700°C. Due to the melting of the samples at low temperatures (~725°C), only limited substitutions with a maximum value of x = 0.15 were achieved. By powder X-ray diffraction, the unit-cell parameters of these compounds were determined to be a = 6.967(1) Å, b = 5.879(2) Å, c = 8.268(2) Å, V = 338.7 $Å^3$ for $Sr_{0.15}Pb_{0.85}GaBO_4$, and a = 6.984(2) Å, b = 5.892(2) Å, c = 8.249(1) Å, V =339.4 $Å^3$ for $Ba_{0.15}Pb_{0.85}GaBO_4$. The unit-cell dimensions of these solid-solutions do not differ significantly from those of $PbGaBO_4$, due to relatively low concentrations of the Sr^{2+} or Ba^{2+} ions. Unsuccessful incorporation of a higher concentration of Sr^{2+} may not be because of its size, since the ionic radius of Sr^{2+} (1.32 Å for CN = 6) is comparable to that of Pb^{2+} (1.12 Å for 4-fold square pyramidal

coordination). However, it can be attributed to the very distinct bonding geometry around the Pb^{2+} ions. The closed-shell Sr^{2+} and Ba^{2+} ions tend to lie in more symmetrical bonding environments with higher coordination numbers, usually ranging from 6 to 12, whereas the Pb^{2+} ion prefers an asymmetrical 4-fold square pyramidal coordination. Indeed, the structure of $SrGaBO_4$ bears little resemblance to that of $PbGaBO_4$ (cf. Chapter 5).

Chapter 4

SYNTHESIS AND STRUCTURES OF α- AND β-$PbAlBO_4$

4.1 Introduction

The $PbAlBO_4$ compound was studied as a part of the investigation of the $PbMBO_4$ compounds (M = Cr, Mn, Fe, Ga), as described in Chapter 3. Although there are known compounds with composition of $M'AlBO_4$ in the $M'O$-Al_2O_3-B_2O_3 (M' = Ca, Sr) systems (Schäfer & Kuzel, 1967; Schuckmann, 1968; Nagai & Ihara, 1971), no PbO-based alumino-borates have yet been reported according to the inorganic structure databases (ICSD, 2001; PC-PDF, 1999). This chapter discusses the solid-state synthesis and the characterization of $PbAlBO_4$ as well as its polymorphism at high temperatures.

4.2 Sample Preparation

As indicated in the solid-state syntheses of $PbMBO_4$ (M = Cr, Mn, Fe, Ga) in Chapter 3, it was necessary to pre-react PbO and Al_2O_3 prior to the addition of H_3BO_3 in order to avoid the formation of $Pb_2B_2O_5$ which melts at 497°C (McMurdie, 1947). A powder sample with a nominal composition of $Pb_2Al_2O_5$ was fired at 850°C for 3 days with daily re-mixing. By powder X-ray diffraction, the product was in fact identified to be a mixture of $Pb_9Al_8O_{21}$ and Al_2O_3, as the $Pb_2Al_2O_5$ compound does not exist (Plötz & Müller-Buschbaum, 1981). The preparation of pre-reacted $2PbO$-Al_2O_3 is shown in the following equation:

$$18PbO + 9Al_2O_3 \rightarrow \text{“}9Pb_2Al_2O_5\text{”}\ (2Pb_9Al_8O_{21} + Al_2O_3)$$

Polycrystalline samples of α- and β-$PbAlBO_4$ were synthesized by heating a 0.5-g pellet containing stoichiometric amounts of pre-reacted $2PbO\text{-}Al_2O_3$ and H_3BO_3 powders. The sample was first heated at 500°C for 1 day in order to dehydrate H_3BO_3. It was subsequently fired at 750°C for 5 days to obtain the α-phase. A well-crystallized, white-coloured α-$PbAlBO_4$ powder was obtained as a final product. The α → β phase transformation was observed within a very narrow temperature range with the β-phase forming at 775°C, just before the incongruent melting of the sample at 810°C. The β-$PbAlBO_4$ phase was obtained by quenching the sample from 775°C to room temperature. The purities of both phases were checked by their X-ray diffraction pattern. The reversal of the phase transformation was also attempted by annealing the β-$PbAlBO_4$ at 700°C for 10 days, but the β to α transformation was not observed. The following equation describes the reaction to prepare the $PbAlBO_4$ compound:

$$Pb_2Al_2O_5 + 2H_3BO_3 \rightarrow 2PbAlBO_4 + 3H_2O$$

Boric acid enriched with ^{11}B (99.27 at. %) was also used to prepare the same compounds for powder neutron diffraction experiments in order to minimize the absorption of neutrons by ^{10}B.

4.3 Structure Determination and Refinement

4.3.1 α-$PbAlBO_4$ at Room Temperature

The structure of α-$PbAlBO_4$ was successfully refined using powder neutron diffraction data. The diffraction data were collected by Dr. Robert Hammond at the Chalk River Laboratories using the C2 high-resolution powder diffractometer. The

Rietveld refinement was carried out using the structural parameters of $PbGaBO_4$ as an initial model with the computer program FULLPROF (Roisnel & Rodriguez-Carvajal, 2001). A total of 29 parameters were refined including 20 structural parameters and 9 profile parameters. The peak shape was described by a Gaussian function and the background was fitted with a 5^{th} order polynomial. After a number of refinement cycles, a good agreement between the observed and calculated profiles was achieved confirming that α-$PbAlBO_4$ is indeed isostructural with $PbGaBO_4$. Figure 4.1 shows the plots of the calculated and observed profiles. The details of the refinement are given in Table 4.1a. The crystal data for $PbAlBO_4$ are presented in Table 4.2. The atomic coordinates and isotropic temperature factors are listed in Table 4.3.

4.3.2 α-$PbAlBO_4$ at High Temperatures

In-situ powder neutron diffraction of α-$PbAlBO_4$ was carried out in order to investigate the structural changes taking place at high temperatures. Six data sets were collected between 500K and 1000K with a stepsize of 100K by heating the sample in the F2 furnace mounted on the C2 diffractometer. The Rietveld refinements of these diffraction data were performed with the atomic parameters of α-$PbAlBO_4$ at room temperature as a starting model. Only the low bank data corresponding to the 2θ range of $5.00 - 83.90^{\circ}$ was used for the refinements due to difficulties associated with merging the low- and high-angle data sets because of greater background noise at higher angles. A weak extra reflection between 32.2° and 33.7° was excluded from each profile. The details of the refinements are shown in Table 4.1b. The refinement plots are given in Figure 4.2. It was observed that the signal-to-noise ratio became poorer with increasing

Table 4.1 Details of the structure refinements

a) α-$PbAlBO_4$ at room temperature

	α-$PbAlBO_4$
Neutron wavelength (Å)	1.3240
2θ range (°)	3.00 – 116.90
Stepsize (°)	0.10
R_p	0.0565
R_{wp}	0.0748
R_{exp}	0.0231
R_{Bragg}	0.0944
χ^2	10.5
Number of reflections	412
Refined parameters	29

b) α-$PbAlBO_4$ at high temperatures

- Neutron wavelength = 1.3289Å
- 2θ range = 5.00 – 83.90°*
- Stepsize = 0.10°

	500K	600K	700K	800K	900K	1000K
R_p	0.0703	0.0654	0.0655	0.0607	0.0639	0.0652
R_{wp}	0.0922	0.0830	0.0892	0.0902	0.0863	0.0867
R_{exp}	0.0553	0.0564	0.0563	0.0567	0.0561	0.0574
R_{Bragg}	0.0796	0.0862	0.0927	0.0921	0.0881	0.107
χ^2	2.77	2.17	2.51	2.53	2.37	2.28
Number of reflections	215	205	207	207	206	206
Refined parameters	27	30	30	29	29	30
Excluded regions (°, 2θ)	32.30 – 33.70	32.25 – 33.60	32.20 – 33.80	32.20 – 33.60	32.20 – 33.70	32.15 – 33.75

* Only low-angle data sets were used because of higher background at high angles which led to difficulties in merging the low and high angle data sets.

c) β-$PbAlBO_4$ at room temperature

Neutron wavelength (Å)	1.3310
2θ range (°)	5.00 – 113.90
Stepsize (°)	0.10
R_p	0.0356
R_{wp}	0.0463
R_{exp}	0.0214
R_{Bragg}	0.0510
χ^2	4.69
Number of reflections	709
Refined parameters	49

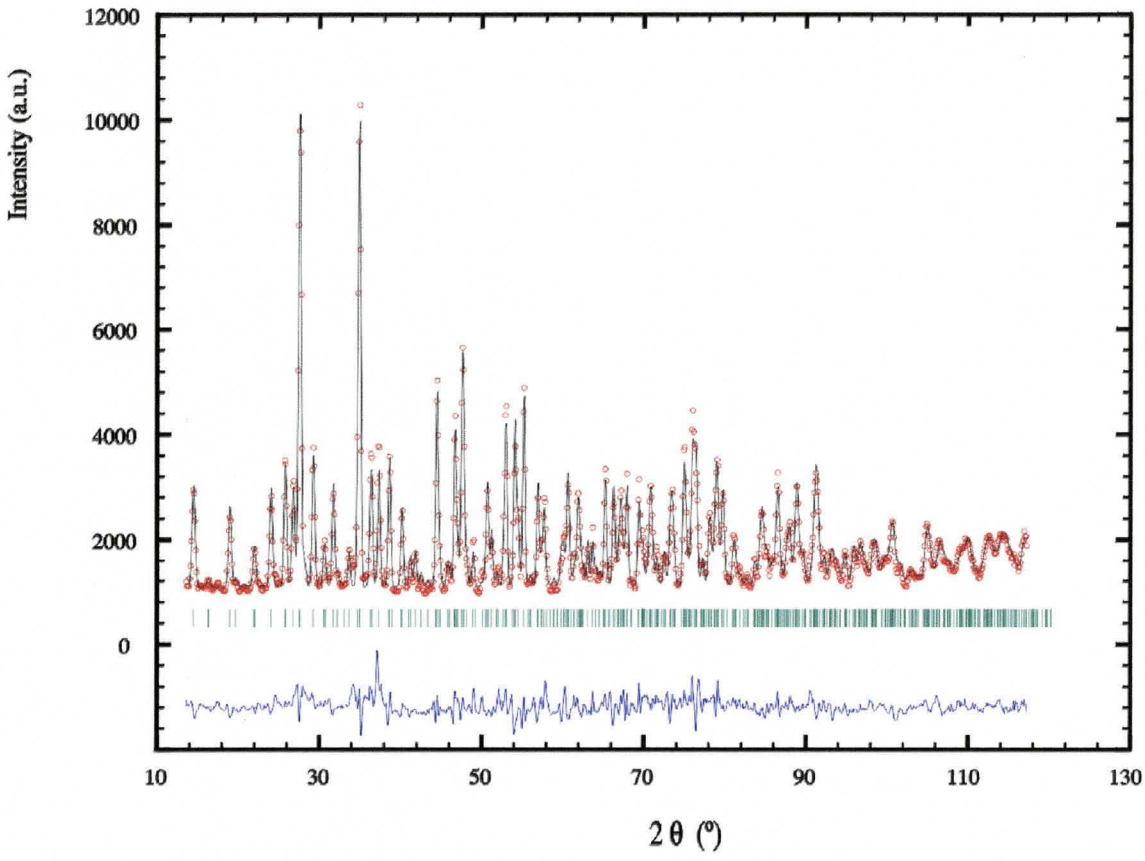

Figure 4.1 Observed (red circles) and calculated (black solid line) profiles for the Rietveld refinement of α-$PbAlBO_4$ at room temperature. The difference between the observed and the calculated profiles is plotted at the bottom. The vertical bars indicate the Bragg peak positions.

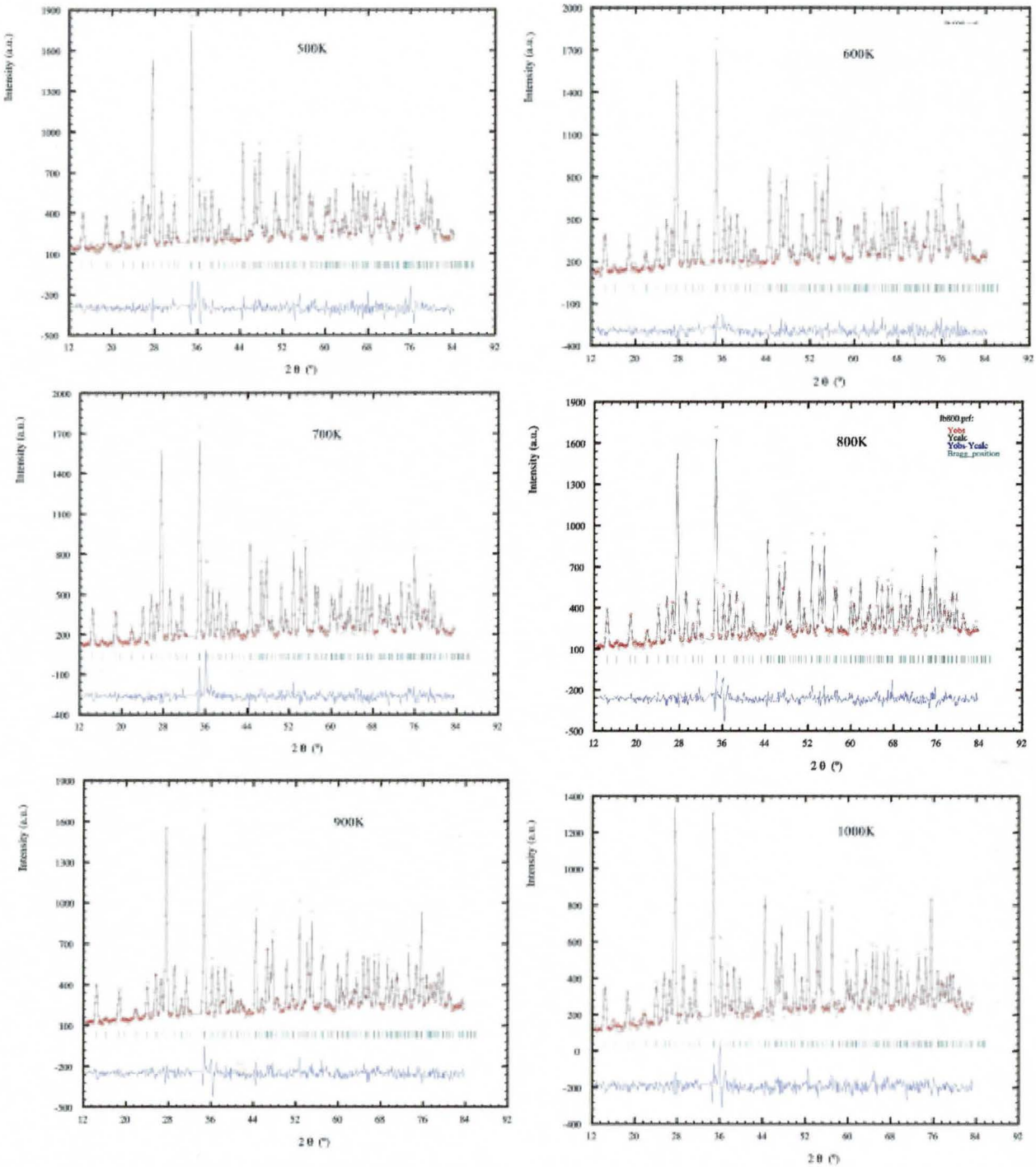

Figure 4.2 Rietveld refinements of α-$PbAlBO_4$ at high temperatures. A small, unidentified peak at 32.2 – 33.7° was excluded from the refinements.

temperature, especially at 1000K. The atomic coordinates and the isotropic displacement parameters are given in Table 4.4. The relatively large esd's on the atomic coordinates can be attributed to the limited data sets used for the refinements. As expected, the isotropic temperature factors (B) became larger with increasing temperature.

4.3.3 β-$PbAlBO_4$ at Room Temperature

The structure of β-$PbAlBO_4$ was initially solved from a powder X-ray diffraction pattern recorded using a Guinier-Hägg camera. The unit-cell dimensions were calculated and refined with the programs VISSER (Visser, 1963) and LSUDF (Evans *et al.*, 1963) by indexing 79 reflections. The solution which indexed all the reflections corresponded to a primitive orthorhombic cell with a = 7.022(1) Å, b = 9.869(1) Å, c = 9.401(1) Å. The Pbcn space group was suggested by the observation of the extinction conditions $k = 2n + 1$ in $0kl$, $l = 2n + 1$ in $h0l$ and $h + k = 2n + 1$ in $hk0$. The number of formula units per unit-cell was assumed to be 8 by comparison of the unit-cell volumes of the α- and β-phases. Based on this information, the *ab-initio* structure determination was then carried out via direct methods using the program EXPO (Altomare *et al.*, 1999). The positions of two Pb atoms, two Al atoms and four O atoms were identified and subsequently used as a starting model for a Rietveld refinement of powder X-ray data collected with a Bruker D8 diffractometer. The atomic coordinates of boron were later determined by locating the centre of gravity of a triangle formed by three oxygen atoms of a BO_3 group.

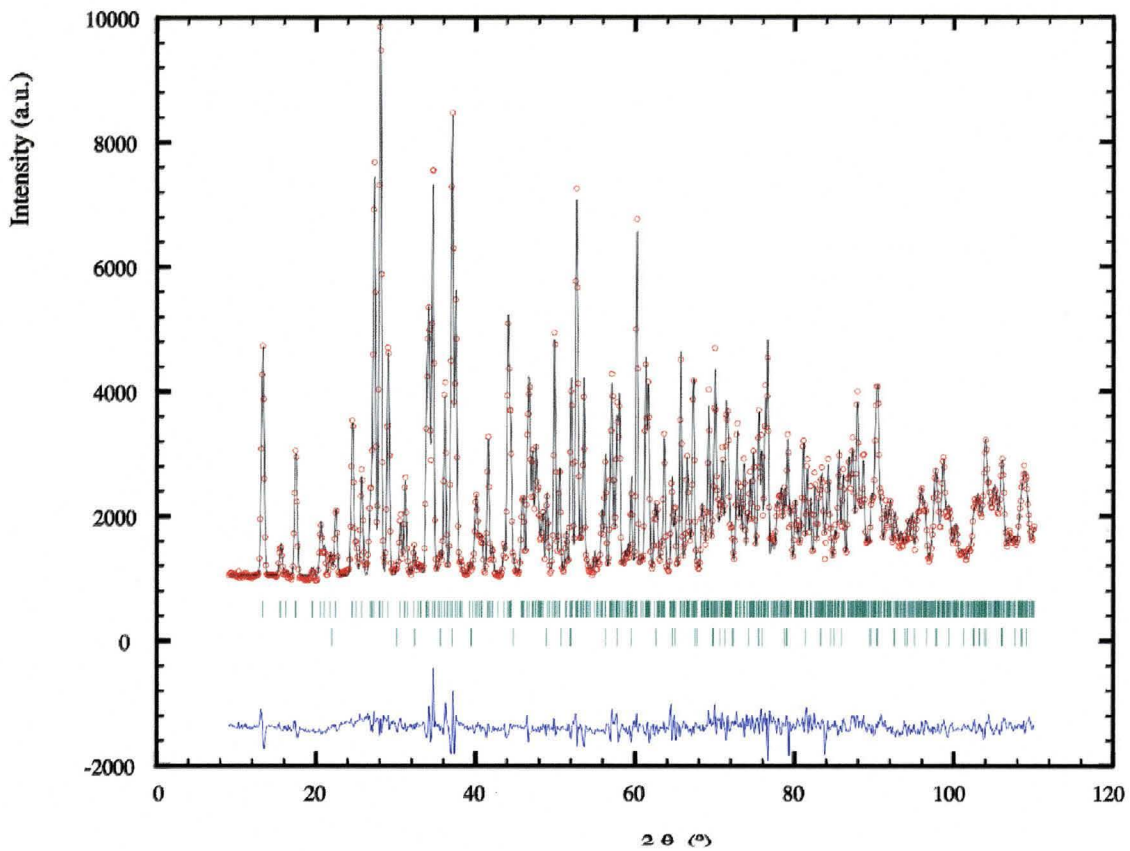

Figure 4.3 Rietveld refinement of β-$PbAlBO_4$ at 300K. A small amount of α-Al_2O_3 in the sample was included in the refinement (lower set of Bragg peaks).

In order to obtain more accurate atomic positions, a Rietveld refinement of β-$PbAlBO_4$ was carried out using powder neutron diffraction data collected at room temperature. The sample contained a small amount of α-Al_2O_3 (2.7 vol. %), which was taken into account during the refinement. A total of 49 parameters were refined, including 36 structural parameters (unit-cell dimensions, atomic positions and temperature factors for both $PbAlBO_4$ and Al_2O_3 phases) and 13 profile parameters. A Gaussian function was chosen to model the peak shape. The final refinement details are listed in Table 4.1c. The plots of the observed and calculated profiles of the refinement are given in Figure 4.3. The good agreement between the observed and the calculated confirms the structure of β-$PbAlBO_4$ determined from the powder X-ray diffraction data. The crystal data are listed in Table 4.2. The atomic coordinates and isotropic displacement parameters of β-$PbAlBO_4$ are given in Table 4.3b.

4.4 Description of the $PbAlBO_4$ Structures

4.4.1 α-$PbAlBO_4$

Selected bond lengths, bond valences and bond angles are shown in Tables 4.5 and 4.6. The structure drawing of α-$PbAlBO_4$ is given in Figure 4.4. The α-$PbAlBO_4$ compound is isostructural with the other $PbMBO_4$ compounds (M = Cr, Mn, Fe, Ga) which are described in Chapter 3. It is based on infinite chains of edge-sharing AlO_6 octahedra parallel to the b-axis, bridged by BO_3 groups. The Pb^{2+} ion occupies four-coordinated sites, displaying a square pyramidal geometry with a non-bonding pair of electrons. As BO_3 triangles bridge adjacent octahedra in the chain, a significant buckling along the chain is again observed with resulting dihedral angles of 49.8° and 77.7°.

Table 4.2 Crystal Data for α and β-$PbAlBO_4$

	α-$PbAlBO_4$ (Pnma)							β-$PbAlBO_4$ (Pbcn)
Temperature (K)	300	500	600	700	800	900	1000	300
Unit cell (Å)								
a	6.9209(5)	6.9255(8)	6.9299(9)	6.9288(9)	6.9272(7)	6.9229(7)	6.9133(11)	7.0423(3)
b	5.7134(4)	5.7318(6)	5.7394(7)	5.7449(7)	5.7520(5)	5.7584(5)	5.7662(8)	9.8989(3)
c	8.0215(6)	8.0611(10)	8.0749(11)	8.0905(11)	8.1076(8)	8.1282(8)	8.1545(12)	9.4281(3)
Volume ($Å^3$)	317.19(4)	319.99(6)	321.16(7)	322.05(7)	323.05(6)	324.03(5)	325.07(8)	657.24(4)
Z	4	4	4	4	4	4	4	8
Calc. density ($g\ cm^{-3}$)	6.470	6.414	6.390	6.373	6.353	6.334	6.314	6.245

Table 4.3a Atomic coordinates and isotropic displacement parameters for α-$PbAlBO_4$ at room temperature

Atom	x	y	z	B ($Å^2$)
Pb	0.0623(5)	1/4	0.3619(4)	0.54(8)
Al	0	0	0	0.6(1)
B	-0.2299(8)	1/4	-0.2585(7)	0.52(9)
O1	0.0998(8)	-1/4	-0.1115(8)	0.4(1)
O2	0.1722(6)	-0.0436(7)	0.1844(5)	0.55(7)
O3	-0.1669(8)	-1/4	0.0961(7)	0.6(1)

Table 4.3b Atomic coordinates and isotropic displacement parameters for β-$PbAlBO_4$ at room temperature

Atom	x	y	z	B ($Å^2$)
Pb	0.9300(3)	0.6705(3)	0.0485(2)	0.51(4)
Al1	1/2	0.332(1)	3/4	0.9(2)
Al2	1/2	1/2	1/2	0.4(1)
B	0.2783(4)	0.4068(4)	0.2472(3)	0.56(6)
O1	0.6003(5)	0.3428(4)	0.5708(4)	0.29(6)
O2	0.3316(5)	0.3906(4)	0.3873(4)	0.56(7)
O3	0.3331(6)	0.5176(4)	0.1700(5)	0.44(8)
O4	0.1722(6)	0.3049(4)	0.1845(4)	0.64(7)

Table 4.4 Atomic coordinates and isotropic displacement parameters for α-$PbAlBO_4$ at high temperatures

500K	x	y	z	B* ($Å^2$)
Pb	0.0621(8)	1/4	0.3632(7)	0.5
Al	0	0	0	0.5
B	-0.229(1)	1/4	-0.260(1)	0.5
O1	0.102(1)	-1/4	-0.112(1)	0.5
O2	0.1729(9)	-0.043(1)	0.1832(8)	0.5
O3	-0.166(1)	-1/4	0.098(1)	0.5

* They were kept constant during the refinement

600K	x	y	z	B ($Å^2$)
Pb	0.0621(8)	1/4	0.3631(7)	0.7(1)
Al	0	0	0	0.3(3)
B	-0.227(1)	1/4	-0.260(1)	0.3(2)
O1	0.101(1)	-1/4	-0.112(1)	0.1(2)
O2	0.1747(9)	-0.042(1)	0.1841(8)	0.6(1)
O3	-0.167(1)	-1/4	0.097(1)	0.4(2)

700K	x	y	z	B ($Å^2$)
Pb	0.0605(8)	1/4	0.3621(7)	1.0(1)
Al	0	0	0	0.5(3)
B	-0.230(1)	1/4	-0.258(1)	0.3(2)
O1	0.101(1)	-1/4	-0.112(1)	0.3(2)
O2	0.1735(9)	-0.043(1)	0.1843(8)	0.7(1)
O3	-0.168(1)	-1/4	0.097(1)	0.8(2)

800K	x	y	z	B ($Å^2$)
Pb	0.0610(9)	1/4	0.3623(8)	1.2(1)
Al	0	0	0	0.4(3)
B	-0.227(1)	1/4	-0.257(1)	0.6(2)
O1	0.100(1)	-1/4	-0.113(1)	0.7(2)
O2	0.176(9)	-0.044(1)	0.1816(8)	1.1(2)
O3	-0.170(1)	-1/4	0.098(1)	0.9(2)

900K	x	y	z	B ($Å^2$)
Pb	0.0598(9)	1/4	0.3618(8)	1.2(1)
Al	0	0	0	0.5(3)
B	-0.229(1)	1/4	-0.256(1)	0.6(2)
O1	0.099(1)	-1/4	-0.111(1)	0.5(2)
O2	0.176(1)	-0.045(1)	0.1807(8)	1.1(1)
O3	-0.169(1)	-1/4	0.098(1)	0.9(2)

1000K	x	y	z	B ($Å^2$)
Pb	0.057(1)	1/4	0.3593(9)	1.4(2)
Al	0	0	0	0.6(3)
B	-0.228(1)	1/4	-0.256(1)	0.7(2)
O1	0.101(1)	-1/4	-0.109(1)	0.3(2)
O2	0.176(9)	-0.043(1)	0.183(1)	1.4(1)
O3	-0.169(1)	-1/4	0.096(1)	0.9(2)

The examination of Al – O bond lengths (Table 4.5) reveals similar distortion of the AlO_6 octahedra as those observed in the other $PbMBO_4$ series (M = Cr, Mn, Fe, Ga). As discussed in Chapter 3, the distorted geometry around the Al^{3+} ion can be rationalized by considering the coordination environments around the oxygen atoms. Since O2 and O3 are bonded to the B atom to form a rigid BO_3 triangle, they receive relatively small bond valence contributions from the Al – O2 and Al – O3 bonds. On the other hand, the O1 atom, bonded to two Pb and two Al, receives no contribution from B, therefore shorter and stronger Al – O1 bonds are needed. However, the bond valence sum around each O atom (Brese & O'Keefe, 1991) indicates that the Al – O1 bonds are too short while the Al – O3 bonds are too long, leading to the over-bonding around O1 and the under-bonding around O3, respectively (Table 4.6). These discrepancies result in the structural strain in the octahedral chains, as seen in the other $PbMBO_4$ compounds.

It is also observed from the bond valence analysis that the Pb^{2+} ions are somewhat over-bonded ($\Sigma s = 2.27$) by comparison with the other isostructural $PbMBO_4$ series where the corresponding sum ranges from 1.79 to 2.13. This can be attributed to compressed Pb – O bond distances due to the reduction of the unit-cell dimensions arising from the relatively small radius of the Al^{3+} ion (0.675 Å; Shannon, 1976). The Al^{3+} ion, however, attains an adequate bond valence sum of 3.04 in spite of the variations in the Al – O bond lengths.

Table 4.5 Bond Distances (l), Bond Valences (s) and Bond Angles (°) in α-$PbAlBO_4$ at 300K

l (Å)		s		
Pb – O1	2.300(7)	0.602	O1 – Al – O1	180.0(4)
Pb – O1	2.348(7)	0.528	O1 – Al – O2	92.3(3)
Pb – O2 x2	2.328(5)	0.558	O1 – Al – O2	87.7(3)
		Σs 2.25	O1 – Al – O3	81.0(3)
Al – O1 x2	1.821(4)	0.632	O1 – Al – O3	99.0(2)
Al – O2 x2	1.916(4)	0.489	O2 – Al – O2	180.0(4)
Al – O3 x2	1.992(4)	0.398	O2 – Al – O3	88.0(3)
		Σs 3.04	O2 – Al – O3	92.0(3)
B – O2 x2	1.380(5)	0.976	O3 – Al – O3	180.0(3)
B – O3	1.367(8)	1.011		
		Σs 2.96	O2 – B – O2	118.4(5)
			O2 – B – O3	120.8(6)

Table 4.6 Bond valences around oxygen atoms in α-$PbAlBO_4$ at 300K

	s		s		s
O1 – Pb	0.602	O2 – Pb	0.558	O3 – Al x2	0.398
Pb	0.528	Al	0.489	B	1.011
Al x2	0.632	B	0.976		
Σs	**2.39**	**Σs**	**2.02**	**Σs**	**1.81**

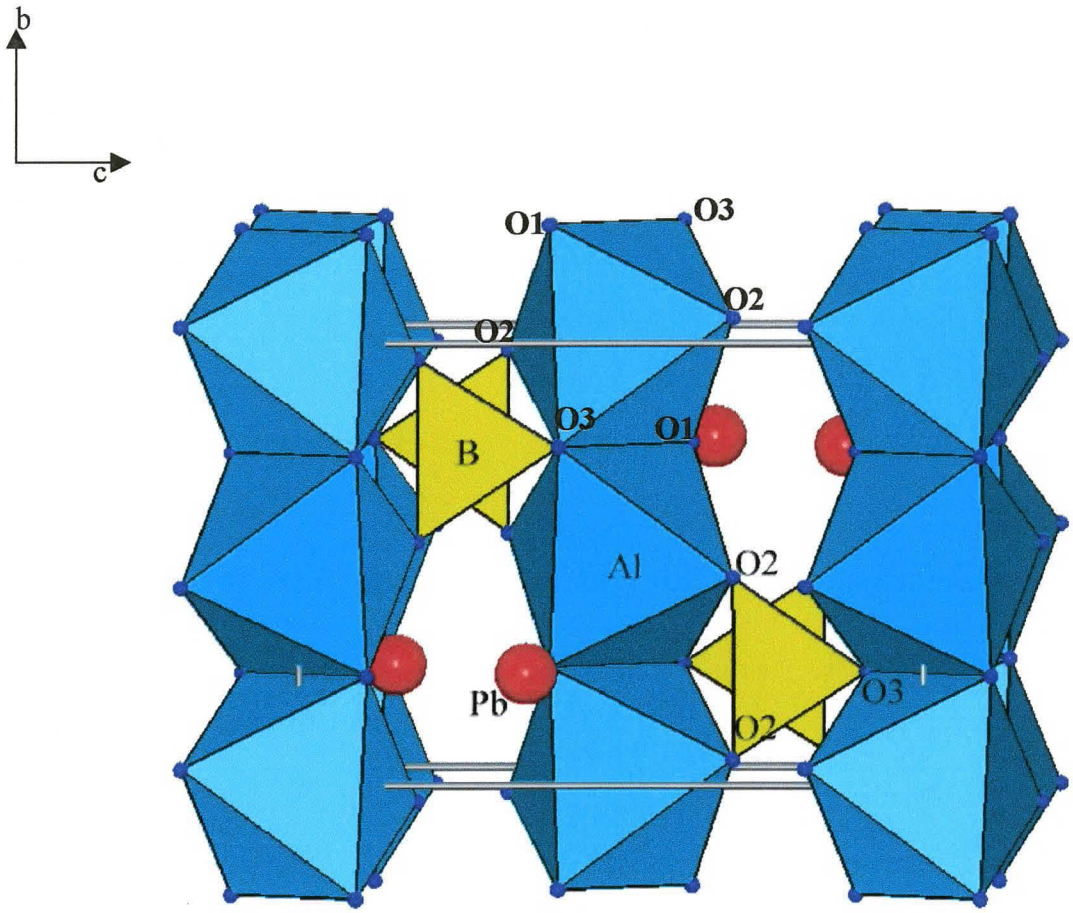

Figure 4.4 Structure of α-$PbAlBO_4$ viewed approximately along the [100] direction. Chains of edge-sharing AlO_6 octahedra run parallel to the b-axis. BO_3 groups are shown by yellow triangles, and Pb^{2+} ions are depicted by red circles.

4.4.2 α-$PbAlBO_4$ at High Temperatures

The unit-cell data for α-$PbAlBO_4$ at high temperatures are listed in Table 4.2. Selected bond distances and bond valences are shown in Tables 4.7 and 4.8, respectively. The Rietveld refinements of the powder neutron diffraction data at high temperatures reveal that there are no significant structural changes, apart from the slight expansion of the unit-cell volume ($\Delta V / V = 2.5$ %). As expected, the isotropic temperature factors become larger at high temperatures, especially for the Pb and Al atoms (Table 4.4). The examination of the dihedral angles (51° - 52° and 76° - 77°) indicates that the tilting of the octahedra along the chains remains similar to what is observed at the room temperature structure as well as to those in the other $PbMBO_4$ compounds. As the bond lengths do not vary significantly over the temperature range, no notable variations were observed in the bond valence sum around each atom.

The expansion of the unit-cell volume is highly anisotropic with the largest increase occurring along the c-axis ($\Delta c / c = 1.7$ %). A smaller increase along the b-axis ($\Delta b / b = 0.9$ %) also contributes to the enlargement of the unit-cell. The a-axis, however, remains nearly constant. The effect of increasing temperature on the unit-cell volume is analogous to the increasing size of M^{3+} ion in the $PbMBO_4$ compounds (Chapter 3). In both cases, the most significant expansion is observed along the c-axis while the a-axis remains relatively unchanged. Again, the similar trend in the small expansion of the O2 – O3 – O2 angle (shown in Figure 3.3) is observed in the α-$PbAlBO_4$ structure (151.4° at 300K vs. 152.5° at 1000K).

The unit-cell volume per oxygen atom increases from 19.82 $Å^3$ at 300K to 20.32 $Å^3$ at 1000K. This corresponds to a small decrease in the density from 6.470 g cm^{-3} at 300K to

Table 4.7 Bond distances in α-$PbAlBO_4$ at high temperatures

	500K	600K	700K	800K	900K	1000K
Pb – O1	2.32(1)	2.32(1)	2.31(1)	2.31(1)	2.32(1)	2.31(1)
Pb – O1	2.34(1)	2.342(9)	2.36(1)	2.36(1)	2.37(1)	2.38(1)
Pb – O2 x2	2.347(7)	2.341(7)	2.347(7)	2.375(8)	2.386(8)	2.367(9)
Al – O1 x2	1.835(6)	1.834(5)	1.835(6)	1.841(6)	1.832(6)	1.833(7)
Al – O2 x2	1.918(6)	1.932(6)	1.931(6)	1.929(9)	1.927(7)	1.939(9)
Al – O3 x2	1.996(9)	2.003(6)	2.008(6)	2.019(6)	2.016(7)	2.014(7)
B – O2 x2	1.394(8)	1.391(7)	1.387(8)	1.381(8)	1.381(8)	1.38(1)
B – O3	1.36(1)	1.37(1)	1.37(1)	1.37(1)	1.38(1)	1.40(2)

Table 4.8 Bond valence sums in α-$PbAlBO_4$ at high temperatures

	500K	600K	700K	800K	900K	1000K
Pb – O1	0.57	0.57	0.58	0.58	0.57	0.58
Pb – O1	0.54	0.54	0.50	0.50	0.50	0.48
Pb – O2 x2	0.53	0.54	0.50	0.49	0.48	0.50
Σs	**2.2**	**2.2**	**2.1**	**2.1**	**2.0**	**2.1**
Al – O1 x2	0.61	0.61	0.61	0.60	0.61	0.61
Al – O2 x2	0.49	0.47	0.47	0.47	0.47	0.46
Al – O3 x2	0.39	0.39	0.38	0.38	0.37	0.37
Σs	**3.0**	**2.9**	**2.9**	**2.9**	**2.9**	**2.9**
B – O2 x2	0.94	0.95	0.99	0.97	0.97	0.98
B – O3	1.03	1.00	0.95	1.00	0.98	0.92
Σs	**3.0**	**3.0**	**2.9**	**3.0**	**2.9**	**2.8**

6.314 g cm^{-3} at 1000K, and is consistent with the general trend that the density of a compound increases with increasing temperature.

Unfortunately, the phase transformation from α to β could not be observed during the *in-situ* neutron diffraction experiments due to the apparent partial melting of the sample between 1000 and 1050K.

4.4.3 β-$PbAlBO_4$ at Room Temperature

Selected bond lengths, bond valences and bond angles are listed in Tables 4.9 and 4.10. The crystal structure of β-$PbAlBO_4$ is depicted in Figure 4.5. The β-phase was obtained by heating the α-phase at 1048K for 12 hours, followed by quenching to room temperature. Therefore, this β-form may be resulted from quenching the sample to room temperature or it may truly represent the structure of $PbAlBO_4$ at high temperatures. The structure of β-$PbAlBO_4$ shares many similarities with that of the α-phase. Both structures are also based on an octahedral coordination of Al^{3+}, a triangular coordination of B^{3+} and a four-fold distorted square pyramidal geometry around Pb^{2+} with a stereoactive lone pair. The β-$PbAlBO_4$ structure can be also viewed as a new orthoborate structure-type with the occurrence of isolated BO_3 groups. The most notable structural difference between the α- and β-phases is seen in the geometry of the AlO_6 chains. The α-phase consists of linear chains which run parallel to the b-axis. However, in the β-phase, the octahedral chains run in a zigzag fashion along the (001) direction as alternate $Al(1)O_6$ and $Al(2)O_6$ octahedra share a pair of opposite or skew edges (Figure 4.6).

Table 4.9 Bond Distances (l), Bond Valences (s) and Bond Angles (°) in β-$PbAlBO_4$ at 300K

l (Å)		s		
			O1 – Al1 – O1	173.3(4)
Pb – O1	2.335(4)	0.547	O1 – Al1 – O3 x2	94.4(4)
Pb – O1	2.369(5)	0.499	O1 – Al1 – O3 x2	80.8(3)
Pb – O2	2.365(5)	0.505	O1 – Al1 – O4 x2	95.5(4)
Pb – O4	2.324(5)	0.564	O1 – Al1 – O4 x2	89.2(4)
		Σs 2.12	O3 – Al1 – O3	86.3(4)
			O3 – Al1 – O4 x2	92.0(4)
Al1 – O1 x2	1.834(4)	0.610	O3 – Al1 – O4 x2	175.7(5)
Al1 – O3 x2	2.040(9)	0.349	O4 – Al1 – O4	89.9(5)
Al1 – O4 x2	1.923(9)	0.479		
		Σs 2.88	O1 – Al2 – O1	180.0(4)
			O1 – Al2 – O2 x2	87.8(3)
Al2 – O1 x2	1.834(4)	0.610	O1 – Al2 – O2 x2	92.2(3)
Al2 – O2 x2	1.926(4)	0.476	O1 – Al2 – O3 x2	97.9(3)
Al2 – O3 x2	1.996(4)	0.394	O1 – Al2 – O3 x2	82.1(3)
		Σs 2.96	O2 – Al2 – O2	180.0(4)
			O2 – Al2 – O3 x2	88.2(3)
B – O2	1.383(5)	0.968	O2 – Al2 – O3 x2	91.8(3)
B – O3	1.371(5)	1.000	O3 – Al2 – O3	180.0(4)
B – O4	1.387(5)	0.958		
		Σs 2.93	O2 – B – O3	121.5(5)
			O2 – B – O4	118.2(5)
			O3 – B – O4	120.3(5)

Table 4.10 Bond valences around oxygen atoms in β-$PbAlBO_4$ at 300K

	s		s		s		s
O1 – Pb	0.547	O2 – Pb	0.505	O3 – Al1	0.349	O4 – Pb	0.564
Pb	0.499	Al1	0.476	Al2	0.394	Al1	0.479
Al1	0.610	B	0.968	B	0.968	B	0.958
Al2	0.610						
Σs	**2.27**	**Σs**	**1.95**	**Σs**	**1.71**	**Σs**	**2.00**

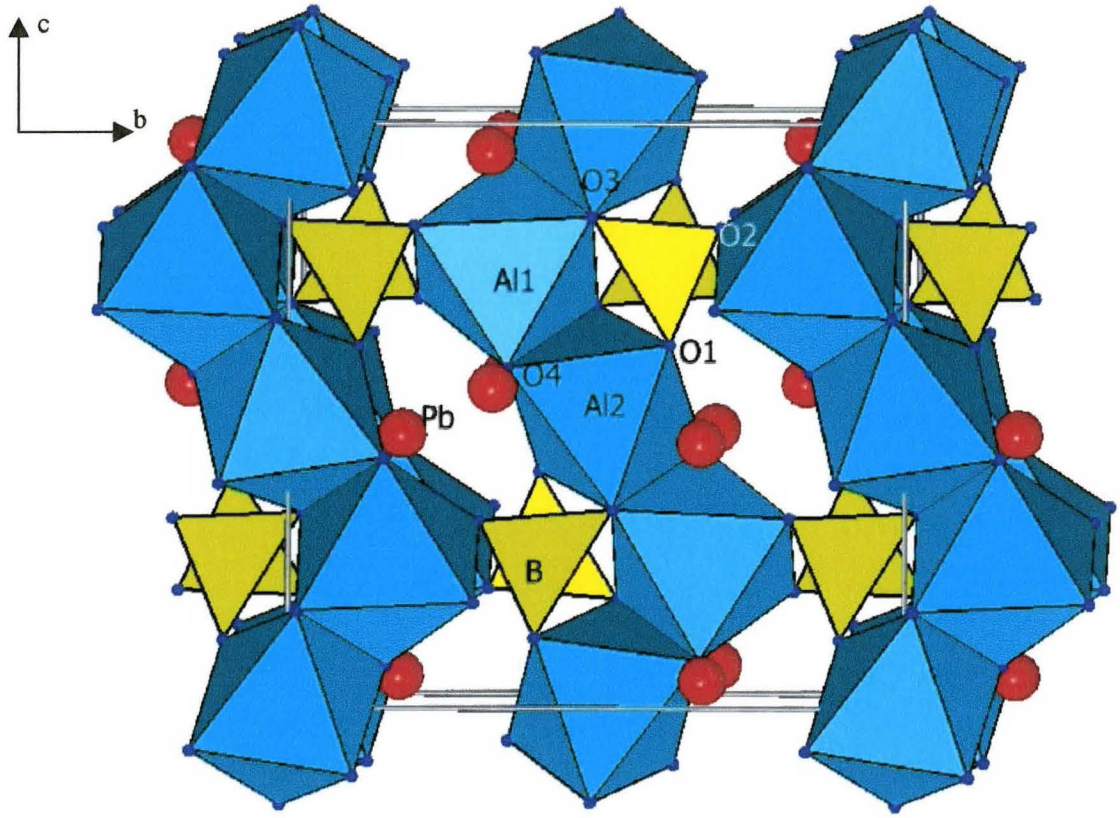

Figure 4.5 Crystal structure of β-$PbAlBO_4$ viewed approximately parallel to the a-axis. Now AlO_6 chains run in a zigzag fashion along the c-axis due to kinks at every third octahedron.

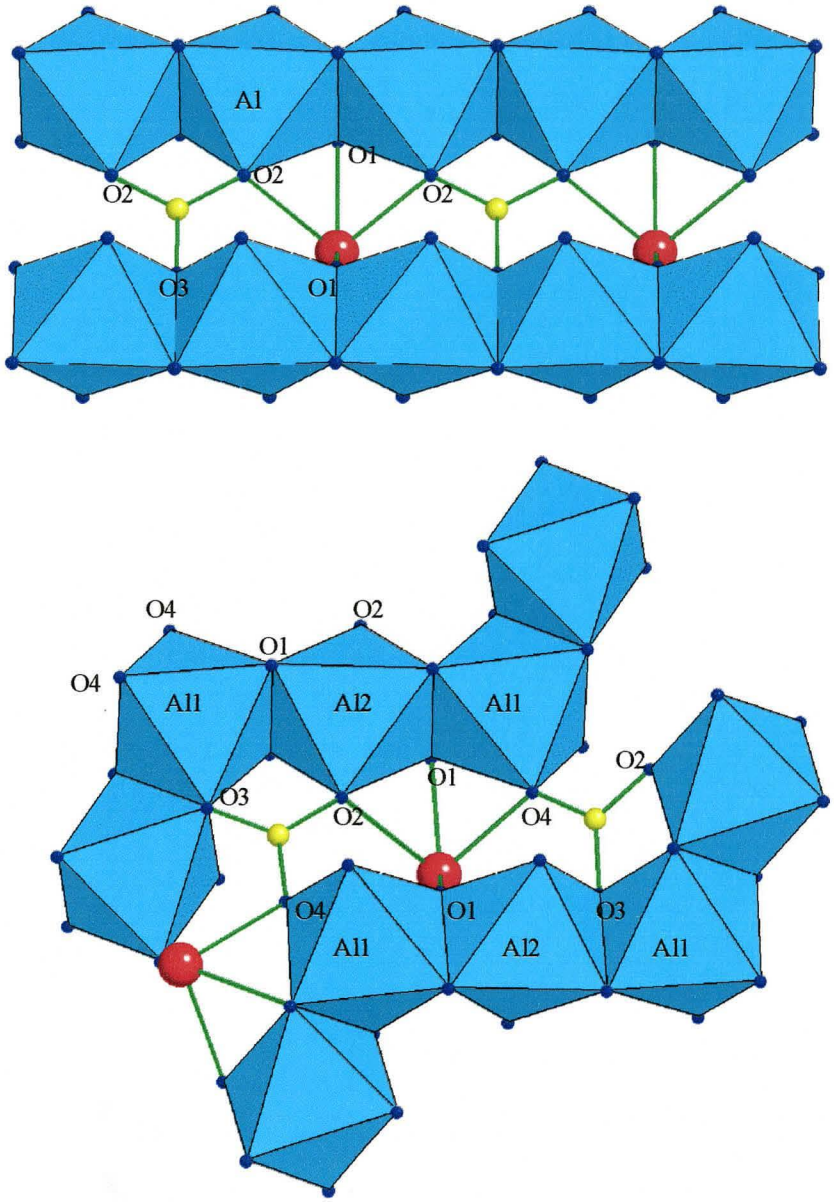

Figure 4.6 Parts of AlO_6 chains bridged by BO_3 groups in α- (top) and β (bottom)-$PbAlBO_4$.

Like the α-phase, the β-$PbAlBO_4$ structure displays a strong buckling along the octahedral chains. Similar deviations of the dihedral angles (51.3° and 77.4°) are again necessary so that a proper triangular coordination environment around the B atom can be achieved. Both $Al(1)^{3+}$ and $Al(2)^{3+}$ ions exhibit distorted octahedral coordination environments with two long Al – O3 bonds and two short Al – O1 bonds. As illustrated in the cases of α-$PbAlBO_4$ as well as the other $PbMBO_4$ compounds, the O1 atom forms stronger bonds with Al, since it does not receive any contribution from the B atom. In contrast, the O3 atom, bonded to B, gets only small bonding contributions from the Al^{3+} ions.

The bond valence analysis around the oxygen atoms (Table 4.11) reveals the presence of a similar structural strain as observed in α-$PbAlBO_4$. The three-coordinated O2 and O3 atoms (Pb + Al + B) attain the expected bond valence sums of 1.95 and 2.01, respectively. However, the bond valence sums around the O1 and O3 atoms significantly deviate from the theoretical value. Due to two long Al – O3 bonds, the three-coordinated O3 atom (Al1 + Al2 + B) is under-bonded ($\Sigma s = 1.74$) while the four-coordinated O1 atom (2Pb + Al1 + Al2) is over-bonded ($\Sigma s = 2.26$) because of relatively short Al – O1 bonds.

4.5 $\alpha \rightarrow \beta$ Phase Transformation of $PbAlBO_4$

Although the α to β phase transformation occurs relatively fast (in 12 hours at 1048K), attempts to reverse the transformation by annealing the β-phase below the transformation temperature at 973K for 10 days have been unsuccessful. The phase reversal from β to α may be very sluggish at low temperatures since it involves the reconstruction of the AlO_6 octahedral chains (i.e. breaking and re-forming of Al – O bonds) in order to introduce or remove kinks along the chains.

It is of interest to ask what is the driving force for the phase transformation in $PbAlBO_4$ between 1023 and 1048K, since the α- and β-phases display very similar structures. The comparison of both polymorphs reveals that the average Al – O distance is slightly larger in the β-phase (1.93 Å vs. 1.91 Å). In addition, longer Pb – O bond distances in the β-form (2.35 Å vs. 2.33 Å) lead to a better bonding environment around the Pb^{2+} ions, since a more proper bond valence sum of 2.12 is now achieved in comparison with 2.27 in the α-phase.

As expected, the volume per oxygen atom is larger in the β-phase (20.54 $Å^3$ vs. 19.82 $Å^3$), corresponding to a decrease in the density from 6.470 g cm^{-3} (α-phase) to 6.245 g cm^{-3} (β-phase) at room temperature. It should be also noted that the density of the β-phase at room temperature is in fact slightly smaller than that of the α-form at 1000K (6.314 g cm^{-3}). This suggests that β-$PbAlBO_4$ must be less dense than the α-phase at the transformation temperature, which agrees with the general expectation that high-temperature polymorphs have lower densities than their low-temperature forms. This decrease in density may play a role in the phase transformation of $PbAlBO_4$, since the

less dense β-phase allows longer interatomic distances, and thus better bonding environments around atoms which, in turn, could lead to a greater stability of the structure.

However, it is interesting to note that a similar phase transformation has not been observed for any of the other $PbMBO_4$ compounds (M = Cr, Mn, Fe, Ga). A comparison of the M^{3+} ionic radii brings some insight which may account for this observation. The size of the Al^{3+} cation (0.675 Å for CN = 6) is significantly smaller than those of the other M^{3+} ions (0.755 - 0.785 Å; Table 3.3). A small M^{3+} cation size leads to a reduction of the unit-cell dimensions and, as a consequence, the average interatomic distances become more compressed. Although the first-nearest neighbour distances (i.e. bond lengths) are very similar in both α- and β-phases, more significant differences are observed in the second-nearest neighbour distances, such as cation – cation distances, particularly $Pb^{2+} \cdots Pb^{2+}$ distances.

In the α-$PbAlBO_4$ and the other $PbMBO_4$ structure, the Pb^{2+} ions are positioned such that their non-bonding electron pairs are anti-parallel to each other, inducing a possible repulsion between the lone pairs (Figure 4.7). The repulsion may be the largest in α-$PbAlBO_4$ since the distance between two neighbouring Pb^{2+} ions is only 3.72 Å, as compared to 3.80 - 3.95 Å in the other $PbMBO_4$ compounds. Inspection of the α-$PbAlBO_4$ structure at high temperatures reveals that the Pb^{2+} ions move further away from each other with increasing temperatures, resulting in the expansion of the Pb ··· Pb distance from 3.72 Å at 300K to 3.77 Å at 1000K. In addition, in the β-$PbAlBO_4$

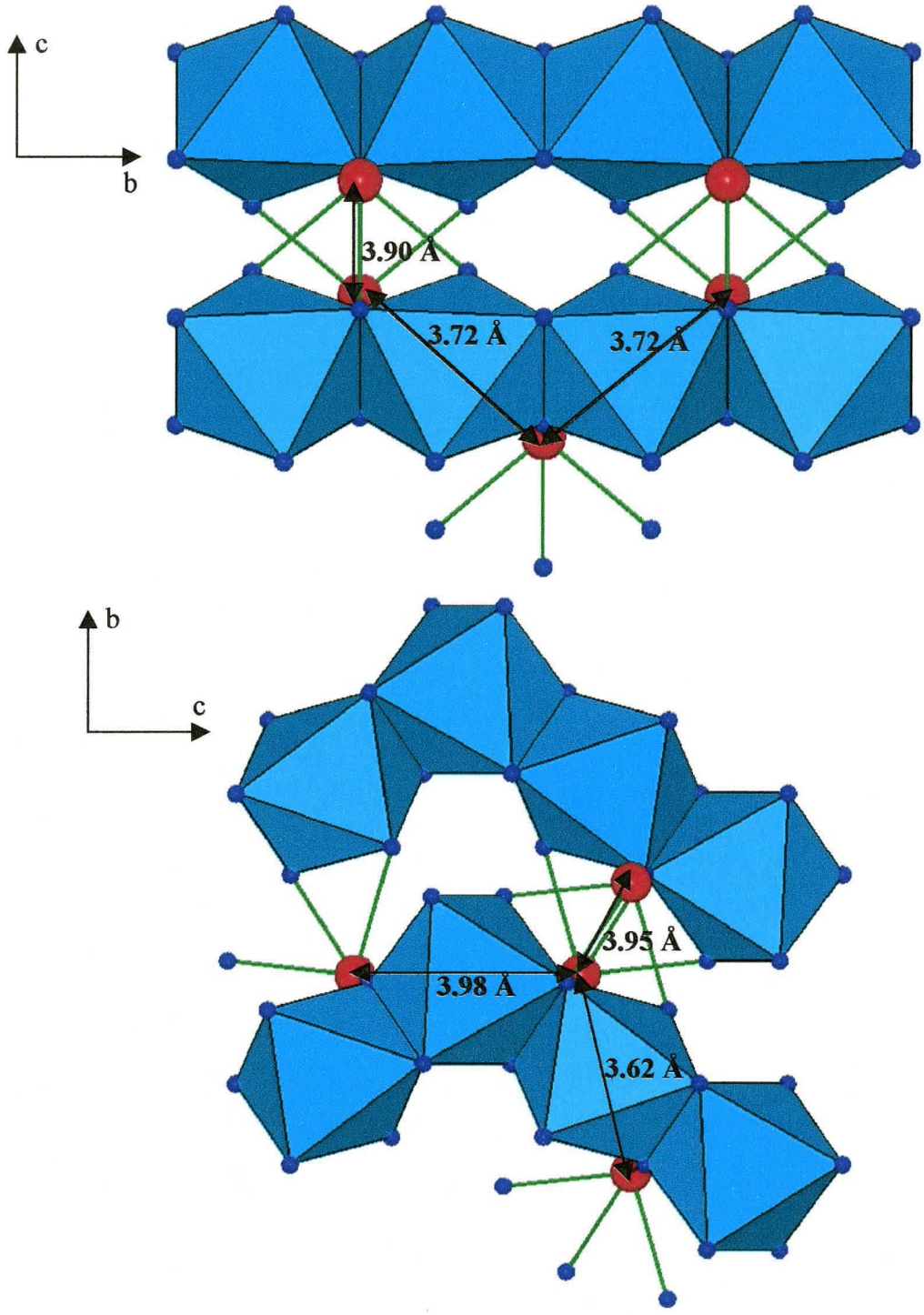

Figure 4.7 The Pb ··· Pb distances in α- (top) and β-(bottom) $PbAlBO_4$.

structure at room temperature, the corresponding $Pb^{2+} \cdots Pb^{2+}$ distances are now 3.62 Å and 3.98 Å due to the presence of kinks along the AlO_6 chains (Figure 4.7).

The above observation implies that the β-$PbAlBO_4$ structure at high temperatures may display the $Pb^{2+} \cdots Pb^{2+}$ distances which are significantly greater than those in the α- or β-phase at room temperature, in order to minimize the repulsion between the lone pairs and thus to increase the stability of the structure. Therefore, it may be suggested that the $Pb^{2+} \cdots Pb^{2+}$ distances and the interactions between the lone pairs may be one of the factors which influences the phase transformation of $PbAlBO_4$.

Chapter 5

SYNTHESIS AND STRUCTURAL CHARACTERIZATION OF $SrGaBO_4$

5.1 Introduction

This research is the continuation of the investigation in the MO – Ga_2O_3 – B_2O_3 system (M = Ca, Sr, Ba) which has already resulted in the synthesis of a new borate structure-type $MGa_2B_2O_7$ (Park & Barbier, 2000). The aim of the study was to prepare Ga-analogues of $CaAlBO_4$ (Schuckmann, 1968) and $SrAlBO_4$ (Nagai & Ihara, 1972). A new compound of composition $SrGaBO_4$ has been synthesized from solid-state reactions and its structure has been determined from powder X-ray diffraction data. However, very recent reports by Yang *et al.* (2001, 2002) have also described the structural characterization of $CaGaBO_4$ and β-$SrGaBO_4$. This chapter presents the solid-state synthesis and structure determination of $SrGaBO_4$ as well as the comparison of the structure with other related compounds. The powder X-ray structure refinement from this work is also compared with that carried out by Yang *et al.* (2002).

5.2 Sample Preparation

Polycrystalline $SrGaBO_4$ was prepared from stoichiometric amounts of $SrCO_3$ or $Sr(NO_3)_2$, Ga_2O_3 and H_3BO_3. A 0.50-g pellet was initially heated at 500°C for 1 day to decompose H_3BO_3. It was subsequently heated at 900°C, as the sample starts to melt incongruently at approximately 950°C. The sample was annealed at this temperature for 5 days with intermediate remixings. The $SrGaBO_4$ compound was obtained as a well-

crystallized, white powder. The purity of the sample was checked by Guinier X-ray diffraction. The following equations illustrate the solid-state synthesis of $SrGaBO_4$:

$$2SrCO_3 + Ga_2O_3 + 2H_3BO_3 \rightarrow 2SrGaBO_4 + 2CO_2 + 3H_2O$$

$$2Sr(NO_3)_2 + Ga_2O_3 + 2H_3BO_3 \rightarrow 2SrGaBO_4 + 2N_2O_5 + 3H_2O$$

Single crystal growth of $SrGaBO_4$ was also attempted using $LiBO_2$ as a flux. A melt consisting of a $3SrGaBO_4 - 2LiBO_2$ mixture was cooled slowly from 900°C to 600°C at a rate of 3.6°C hr^{-1}. However, no crystalline materials, except unreacted $LiBO_2$, were recovered due to the probable formation of borate glasses.

5.3 Structure Determination and Refinement from Powder X-ray Diffraction Data

The crystal structure of $SrGaBO_4$ was solved from a powder X-ray diffraction pattern recorded with a Guinier-Hägg camera. The unit-cell parameters were first determined with the program VISSER (Visser, 1968) and refined by indexing 59 reflections. The solution which indexed all the peaks corresponded to a primitive orthorhombic cell with a = 9.5367(7) Å, b = 15.375(1) Å, c = 5.9204(6) Å. The indexed powder X-ray pattern of $SrGaBO_4$ is given in Table 5.1. The Pbam and Pba2 space groups were suggested by observing the systematic absences $k = 2n + 1$ in $0kl$, $h = 2n + 1$ in $h0l$, $h = 2n + 1$ in $h00$ and $k = 2n + 1$ in $0k0$. The presence of a b-glide plane perpendicular to the a-axis was confirmed by electron diffraction, as shown in Figure 5.1. Considering the similarity in the unit-cell volume, the number of formula units per unit-cell was assumed to be the same (Z = 8) as those of the analogous compounds, $SrAlBO_4$

Table 5.1 Indexed powder X-ray diffraction pattern of $SrGaBO_4$

h	k	l	I(obs)	d(obs, Å)	d(cal, Å)	2θ(obs, °)	2θ(calc, °)
2	0	0	2	7.6873	7.6875	11.502	11.501
2	1	0	3	5.8467	5.8436	15.141	15.150
2	0	1	9	4.6980	4.6906	18.874	18.904
0	2	0	12	4.4960	4.4967	19.730	19.729
3	1	0	16	4.4542	4.4527	19.918	19.924
2	1	1	4	4.1601	4.1589	21.341	21.348
2	2	0	31	3.8822	3.8815	22.889	22.895
4	0	0	10	3.8439	3.8437	23.120	23.121
0	2	1	5	3.5810	3.5809	24.843	24.846
3	1	1	3	3.5569	3.5586	25.015	25.003
4	1	0	7	3.5353	3.5344	25.170	25.176
1	2	1	2	3.4871	3.4876	25.524	25.522
2	2	1	11	3.2453	3.2460	27.461	27.456
4	0	1	21	3.2241	3.2239	27.645	27.647
0	0	2	2	2.9608	2.9602	30.160	30.167
4	2	0	12	2.9226	2.9218	30.564	30.573
2	3	0	25	2.7928	2.7930	32.022	32.022
1	1	2	100	2.7654	2.7659	32.348	32.342
1	3	1	1	2.6349	2.6349	33.998	33.999
5	1	1	5	2.6122	2.6113	34.301	34.314
6	0	0	2	2.5643	2.5633	34.963	34.988
3	1	2	53	2.4652	2.4651	36.416	36.418
1	2	2	3	2.4419	2.4412	36.775	36.789
5	3	0	3	2.1471	2.1465	42.048	42.062
7	1	0	2	2.1336	2.1337	42.328	42.325
0	4	1	4	2.1018	2.1019	42.999	43.001
6	2	1	6	2.0833	2.0839	43.401	43.388
2	3	2	2	2.0314	2.0315	44.568	44.568
7	2	0	3	1.9737	1.9736	45.944	45.948
3	3	2	17	1.9483	1.9482	46.579	46.582
5	2	2	7	1.9267	1.9269	47.133	47.128
1	1	3	5	1.9126	1.9126	47.499	47.501
6	1	2	5	1.8938	1.8940	47.999	47.997
2	1	3	3	1.8705	1.8697	48.638	48.660
6	3	1	10	1.8499	1.8503	49.215	49.206
0	2	3	3	1.8066	1.8071	50.476	50.463
6	2	2	18	1.7789	1.7793	51.319	51.307
7	3	0	3	1.7716	1.7718	51.545	51.542
4	0	3	3	1.7555	1.7556	52.054	52.051
2	5	0	3	1.7516	1.7514	52.178	52.190
2	4	2	3	1.7436	1.7438	52.444	52.433
7	1	2	10	1.7310	1.7309	52.848	52.850
1	5	1	3	1.7108	1.7103	53.522	53.541
3	5	0	3	1.6963	1.6972	54.015	53.988
3	4	2	7	1.6902	1.6903	54.225	54.226

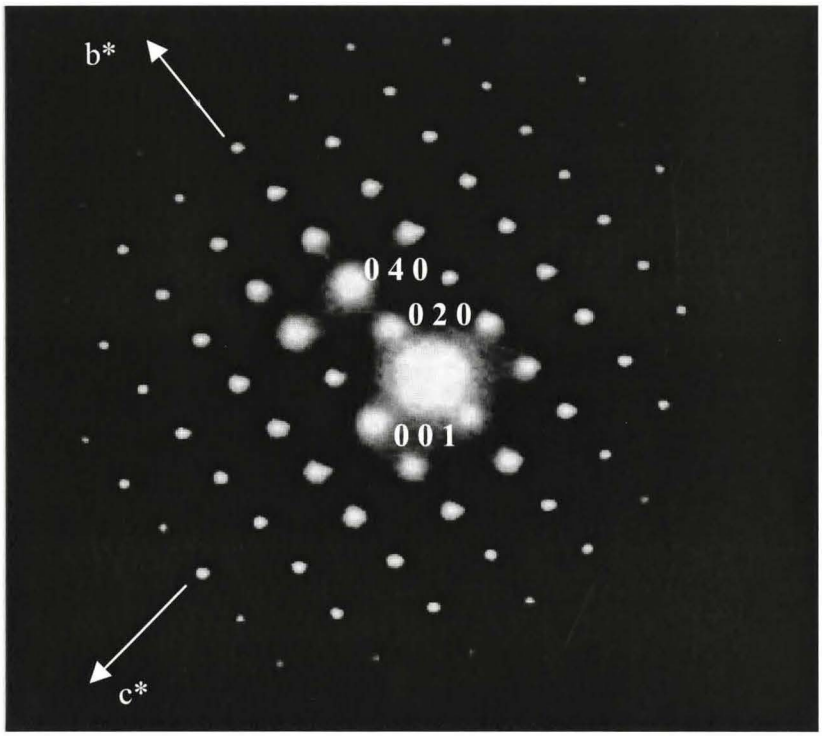

Figure 5.1 Electron diffraction pattern of $SrGaBO_4$. The extinction condition ($0kl$, $k = 2n + 1$) indicates the presence of a b-glide plane perpendicular to the a-axis.

(Nagai & Ihara, 1972) and $CaAlBO_4$ (Schuckmann, 1968). Based on this unit-cell information, an *ab-initio* structure determination was carried out in the Pbam space group, using the computer software EXPO (Altomare *et al.*, 1999). The solution with the highest figure-of-merit yielded the positions of two Sr, one Ga and five O atoms. These positions were taken as an initial model for the Rietveld refinement of the full X-ray powder pattern collected with a Bruker D8 diffractometer, with the program FULLPROF (Roisnel & Rodriguez-Carvajal, 2001). Subsequent Fourier difference maps revealed the location of the sixth O atom. The positions of two B atoms were then determined by calculating the centres of gravity of triangles formed by oxygen atoms, upon the assumption of the three-fold coordination around both B atoms.

Once all the atomic positions were determined, the full Rietveld refinement of the $SrGaBO_4$ structure was performed. A total of 43 parameters were refined including 31 structural parameters (unit-cell dimensions, atomic coordinates and isotropic temperature factors) and 11 profile parameters. A pseudo-Voigt function was used to describe the peak shape, and a fourth-order polynomial was applied to model the background. The lengths of two B – O bonds (B1 – O4 and B2 – O6) were constrained to be 1.36(1) Å in order to keep regular triangular coordination environments around the B atoms. One parameter, based on the March-Dollase function (Dollase, 1986), was refined to account for a strong (110) preferred orientation (G = 0.845(3)). The final refinement details are given in Table 5.2, and the plot of the observed and calculated profiles is shown in Figure 5.2. The good agreement between the observed and the calculated profiles, together with low R factors, confirms the validity of the structure of $SrGaBO_4$ solved from the powder X-ray diffraction data. The crystal data for $SrGaBO_4$ are listed in

Table 5.2 Details of Rietveld Refinements of $SrGaBO_4$

Wavelength (Å)	$CuK\alpha_1$	
2θ range (°)	10.00 – 90.00	
Stepsize (°)	0.02	
Counting time	13 seconds/step	
	Pbam	**Pba2**
R_p	0.124	0.124
R_{wp}	0.161	0.158
R_{exp}	0.105	0.105
R_{Bragg}	0.092	0.092
χ^2	2.33	2.31
Number of reflections	419	419
Refined parameters	43	62

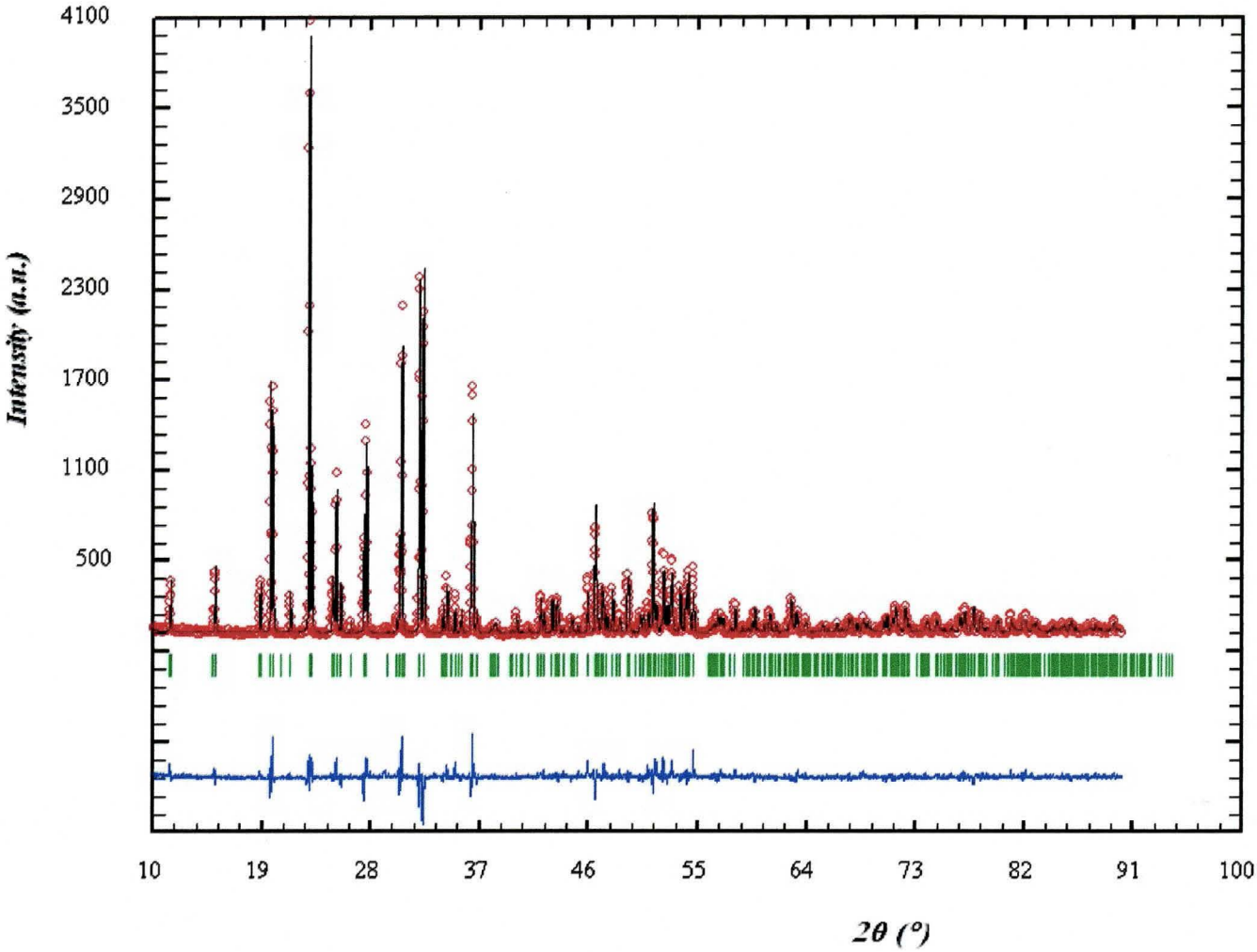

Figure 5.2 Observed (red circles) and calculated (black solid line) profiles for the Rietveld refinement of $SrGaBO_4$ in Pbam setting. The difference between the observed and the calculated profiles is plotted at the bottom. The green vertical bars represent the Bragg peak positions.

Table 5.3 Crystal Data for $SrGaBO_4$ and its related compounds

	$SrGaBO_4$		β-$SrGaBO_4$	$SrAlBO_4$	$CaAlBO_4$	$CaGaBO_4$
Space group	Pbam	Pba2	$P2_12_12$	Pccn	Ccc2	Ccc2
Unit cell (Å)						
a	15.3777(3)	15.3830(4)	15.3706(2)	15.23(3)	15.17(4)	15.473(1)
b	8.9935(2)	8.9965(2)	8.9921(1)	8.86(3)	8.27(3)	8.2940(8)
c	5.9221(1)	5.9232(2)	5.9191(1)	5.48(2)	5.73(3)	5.8392(6)
Volume ($Å^3$)	819.02	819.7	818.1	739.5	718.9	749.3
Z	8	8	8	8	8	8
Density ($g\ cm^{-3}$)	3.765	3.762	3.770	3.403	2.622	3.273
Reference	This work	This work	Yang *et al.*, 2002	Nagai & Ihara, 1972	Schuckmann, 1968	Yang *et al.*, 2001

Table 5.4. Atomic Coordinates and Isotropic Displacement Parameters of $SrGaBO_4$

a) Pbam space group

	x	y	z	B ($Å^2$)
Sr1	0.3784(2)	0.5726(4)	1/2	0.60(9)
Sr2	0.4793(2)	0.2847(4)	0	0.74(9)
Ga	0.3470(2)	-0.0383(3)	-0.2523(6)	1.00(8)
B1	0.926(2)	0.308(2)	1/2	1.0[1]
B2	0.6888(6)	0.461(4)	0	1.0[1]
O1	0.9016(8)	0.355(1)	0.293(2)	1.6(2)[2]
O2	0.354(1)	0.847(2)	1/2	1.6(2)[2]
O3	0.613(1)	0.118(2)	0	1.6(2)[2]
O4	0.7330(8)	0.483(1)	0.202(2)	1.6(2)[2]
O5	0.967(1)	0.174(2)	1/2	1.6(2)[2]
O6	0.5999(5)	0.470(2)	0	1.6(2)[2]

1. The isotropic displacement parameter was set at 1.0$Å^2$ for boron atoms
2. A common parameter was refined for all O atoms

b) Pba2 space group

	x	y	z	B ($Å^2$)
Sr1	0.3785(2)	0.5725(3)	1/2[1]	1.2(1)
Sr2	0.4786(2)	0.2854(3)	0.015(3)	1.6(1)
Ga1	0.3480(8)	-0.034(1)	-0.260(3)	1.30(8)[2]
Ga2	0.3462(7)	-0.043(1)	0.247(3)	1.30(8)[2]
B1	0.924(2)	0.311(2)	0.530(1)	1.0[3]
B2	0.6820(5)	0.461(3)	0.014(1)	1.0[3]
O1	0.893(2)	0.385(3)	-0.284(3)	0.9(2)[2]
O11	0.908(2)	0.348(3)	0.310(2)	0.9(2)[2]
O2	0.355(1)	0.848(2)	0.527(8)	0.9(2)[2]
O3	0.617(1)	0.114(2)	-0.023(8)	0.9(2)[2]
O4	0.742(2)	0.483(4)	0.183(3)	0.9(2)[2]
O44	0.719(2)	0.480(4)	-0.195(3)	0.9(2)[2]
O5	0.966(1)	0.177(1)	0.51(1)	0.9(2)[2]
O6	0.5945(6)	0.471(2)	0.058(4)	0.9(2)[2]

1. The z-coordinate of Sr1 was fixed at 1/2 to keep the other atoms from floating along the z-axis
2. Common B parameters were refined for the Ga and O atoms, respectively
3. The parameter was fixed at 1.0 $Å^2$ for both B atoms

Table 5.3. The atomic coordinates and isotropic temperature parameters are presented in Table 5.4a.

Based on the very recent report of the observation of weak non-linear optical effects in β-$SrGaBO_4$ (Yang *et al.*, 2002), the structure refinement was also attempted with the non-centrosymmetric Pba2 space group. It was carried out based on the structural parameters determined from the Pbam refinement. In this case, three additional atomic positions were generated by splitting each of the Ga, O1 and O4 positions into two due to the absence of a mirror plane perpendicular to the c-axis. A total of 62 parameters (45 structural and 17 profile) were refined in this case. The z-coordinate of the Sr1 atom was fixed at 1/2 in order to keep all the other atoms from floating along the z-axis. All B – O bond lengths were constrained to be 1.36(1) Å to achieve regular triangular coordination environments around B1 and B2. However, no significant improvements were observed in terms of agreement factors by comparison with the Pbam refinement. In fact, the refinement in the Pba2 space group led to poor convergence with larger esd's on the atomic positions (cf. Table 5.4b).

The examination of the atomic coordinates in the Pba2 space group shows that the atoms located on special positions in Pbam are now slightly displaced from z = 0 or 1/2 along the c-axis, as the mirror planes perpendicular to the c-axis are removed. Although the positions of the heavier atoms (i.e. Sr and Ga) have remained essentially unchanged, most oxygen atoms have shifted from their corresponding positions in the centrosymmetric structure. The positions of the O1 and O4 atoms are also slightly displaced along the c- and b-axis, respectively, and the O6 atom is, in particular, significantly shifted from z = 0 to a new z-coordinate of 0.058(4).

Table 5.5 Bond distances, valences and angles for $SrGaBO_4$

a) Pbam space group

Distance (Å)		s	Angle (°)	
Sr1 – O2	2.50(2)	0.36	O1 – Ga – O2	112(1)
Sr1 – O4 x2	2.48(1)	0.38	O1 – Ga – O3	108(1)
Sr1 – O5	2.54(2)	0.32	O1 – Ga – O4	103(1)
Sr1 – O5	2.60(1)	0.27	O2 – Ga – O3	115.9(5)
Sr1 – O6 x2	3.004(2)	0.09	O2 – Ga – O4	110(1)
		Σs 1.9	O3 – Ga – O4	108(1)
Sr2 – O1 x2	2.45(1)	0.41		
Sr2 – O3	2.54(2)	0.32	O1 – B1 – O1	131(2)
Sr2 – O5 x2	2.990(2)	0.09	O1 – B1 – O5 x2	114(2)
Sr2 – O6	2.52(1)	0.34		
Sr2 – O6	2.49(1)	0.37	O4 – B2 – O4	122(2)
		Σs 1.9	O4 – B2 – O6 x2	117(1)
Ga – O1	1.86(1)	0.70		
Ga – O2	1.80(1)	0.83		
Ga – O3	1.77(1)	0.90		
Ga – O4	1.89(1)	0.65		
		Σs 3.1		
B1 – O1 x2	1.35(2)	1.06		
B1 – O5	1.37(3)	1.00		
		Σs 3.1		
B2 – O4 x2	1.37(1)	1.00		
B2 – O6	1.37(1)	1.00		
		Σs 3.0		

Bond	s	Bond	s
O1 – Sr2	0.41	O4 – Sr1	0.38
Ga	0.70	Ga	0.65
B1	1.06	B2	1.00
Σs	**2.2**	**Σs**	**2.0**
		O5 – Sr1	0.32
O2 – Sr1	0.36	Sr1 x2	0.27
Ga x2	0.83	Sr2	0.09
Σs	**2.0**	B	1.00
		Σs	**2.0**
		O6 – Sr1 x2	0.09
O3 – Sr2	0.32	Sr2	0.34
Ga x2	0.90	Sr2	0.37
Σs	**2.1**	B2	1.00
		Σs	**1.9**

b) Pba2 space group

l (Å)		s
Sr1 – O2	2.51(2)	0.35
Sr1 – O4	2.69(2)	0.22
Sr1 – O44	2.39(2)	0.47
Sr1 – O5	2.57(2)	0.30
Sr1 – O5	2.62(1)	0.26
Sr1 – O6	2.68(3)	0.22
		Σs 1.8
Sr2 – O1	2.69(3)	0.21
Sr2 – O11	2.38(3)	0.49
Sr2 – O3	2.64(2)	0.24
Sr2 – O5	3.01(8)	0.09
Sr2 – O5	2.96(8)	0.10
Sr2 – O6	2.45(1)	0.40
Sr2 – O6	2.48(2)	0.38
		Σs 1.9
Ga1 – O1	1.51(3)	1.81
Ga1 – O2	1.65(4)	1.22
Ga1 – O3	1.67(5)	1.21
Ga1 – O44	2.08(3)	0.39
		Σs 4.6
Ga2 – O11	2.03(3)	0.45
Ga2 – O2	1.93(5)	0.57
Ga2 – O3	1.82(5)	0.79
Ga2 – O4	1.74(3)	0.98
		Σs 2.8
B1 – O1	1.37(2)	1.00
B1 – O11	1.37(2)	1.00
B1 – O5	1.38(3)	1.06
		Σs 3.1
B2 – O4	1.37(3)	1.00
B2 – O44	1.37(1)	1.00
B2 – O6	1.37(1)	1.00
		Σs 3.0

These shifts in the atomic coordinates in the Pba2 space group lead to changes in the bonding environments around some atoms, particularly Sr1 and Ga1. As shown in Table 5.5b, the Sr1 atom is now octahedrally coordinated, while the corresponding atom in Pbam lies in a 7-fold position with 2 long Sr – O bonds. Although the Ga1 atom still attains a four-fold coordination, its bonding environment in the Pba2 case is highly irregular with 3 very short and 1 long Ga1 – O bonds, resulting in a significantly large bond valence sum. By comparison, the coordination environment around Ga in the Pbam structure is more regular with an adequate bond valence sum of 3.1.

The observation of a small SHG signal by Yang *et al.* (2002) could be attributed to local deviations from centrosymmetry due to various factors such as oxygen anion disorder. The refinement of anisotropic displacement parameters of the oxygen atoms would perhaps confirm the presence of a strong anisotropy, however such a structure refinement is quite difficult to achieve using powder X-ray diffraction data. Indeed, attempts to refine the anisotropic displacement parameters of Sr and Ga atoms did not result in any improvements, as some of the coefficients became negative. Nevertheless, based on the above observations, it can be proposed that the correct space group for the $SrGaBO_4$ structure should be Pbam since this centrosymmetric setting provides the description of a better bonding geometry overall.

5.4 Description of the $SrGaBO_4$ Structure (Pbam space group)

Selected bond lengths, bond valences and bond angles are presented in Table 5.5a. The structure drawing of $SrGaBO_4$ is given in Figure 5.3.

The structure of $SrGaBO_4$, which can be formulated as an orthoborate oxide, $SrGa(BO_3)O$, is based on one-dimensional chains of corner-sharing GaO_4 tetrahedra along the c-axis with Sr atoms occurring in the interstitial sites. The triangular BO_3 groups bridge adjacent GaO_4 tetrahedra by linking two O4 or two O1 atoms, creating Ga_2BO_8 rings.

The examination of the coordination environment around Ga shows that the GaO_4 tetrahedra are distorted with two short and two long Ga – O bonds. This distortion can be accounted for by considering the bond valence sums around the oxygen atoms as seen in Table 5.6a (Brese & O'Keefe, 1991). The O1 and O4 atoms receive strong contributions from the B atoms corresponding to short, rigid B – O bonds. As a result, the Ga – O1 and Ga – O4 bonds need to be relatively longer and weaker (1.86 – 1.89 Å) in order to achieve proper bond valence sums. On the other hand, the Ga - O2 and Ga - O3 bonds, which form the backbone of the tetrahedral chain, are shorter and stronger (1.77 – 1.80 Å) since these oxygen atoms are not bonded to the B atoms. Indeed, all the O atoms in the $SrGaBO_4$ structure attain adequate bond valence sums. The 5-coordinated O5 (3Sr1 + Sr2 + B1) and O6 (2Sr1 + 2Sr2 + B2) atoms achieve bond valences sums of 2.0 and 1.9, respectively.

Strong angular distortions are observed along the GaO_4 tetrahedral chains which are imposed by the bridging B(1)O3 and B(2)O3 groups (cf. Figure 5.4). The resulting dihedral angles along the chain backbone are 48° (O1 – O2 – O1 and O4 – O3 – O4) and 72° (O1 – O3 – O1 and O4 – O2 – O4), respectively. This distortion is similar to what is observed in the $PbMBO_4$ compounds (M = Al, Cr, Mn, Fe, Ga; cf. Chapters 3 and 4),

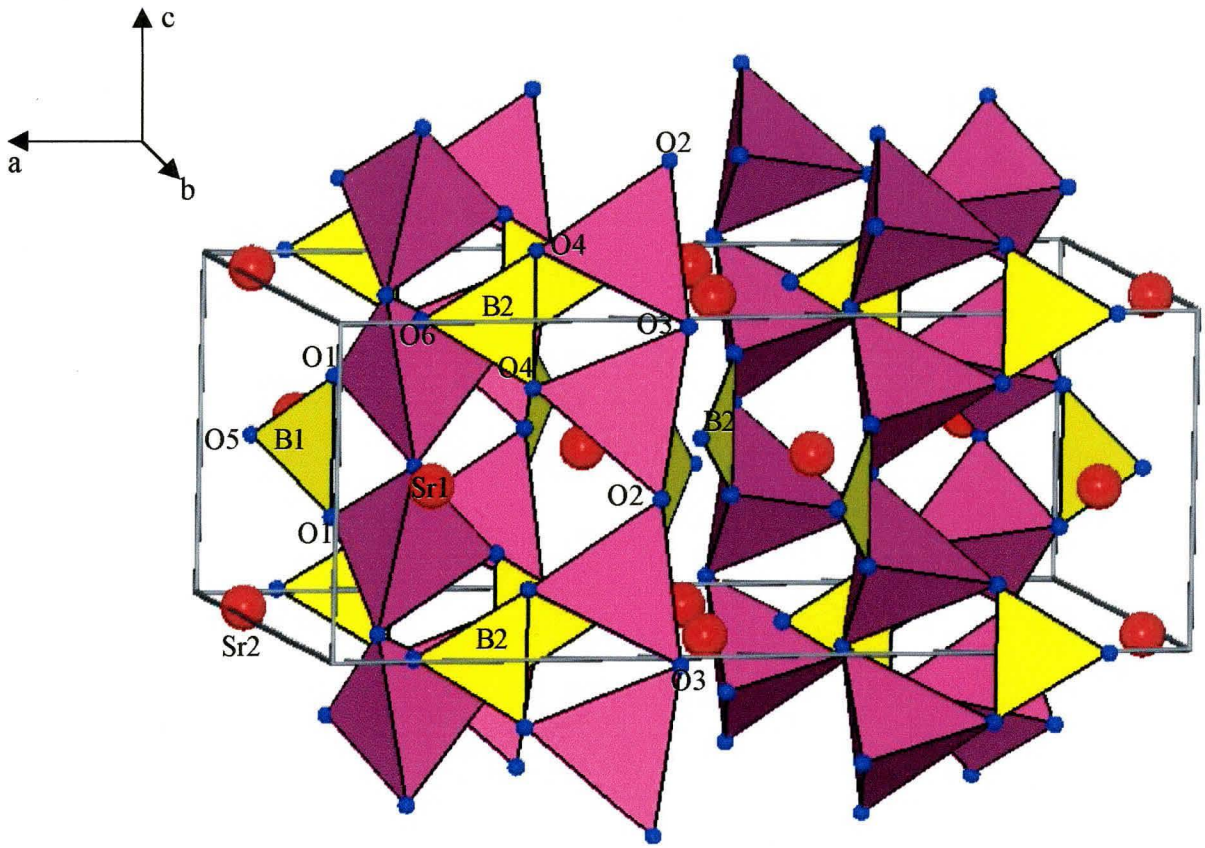

Figure 5.3 Crystal structure of $SrGaBO_4$. Two GaO_4 tetrahedra (pink) and one BO_3 triangle (yellow) form a 6-membered Ga_2BO_8 network, then the chains of GaO_4 tetrahedra run parallel to the c-axis. The Sr^{2+} ions (red circles) occur in the cavities surrounded by the tetrahedral chains.

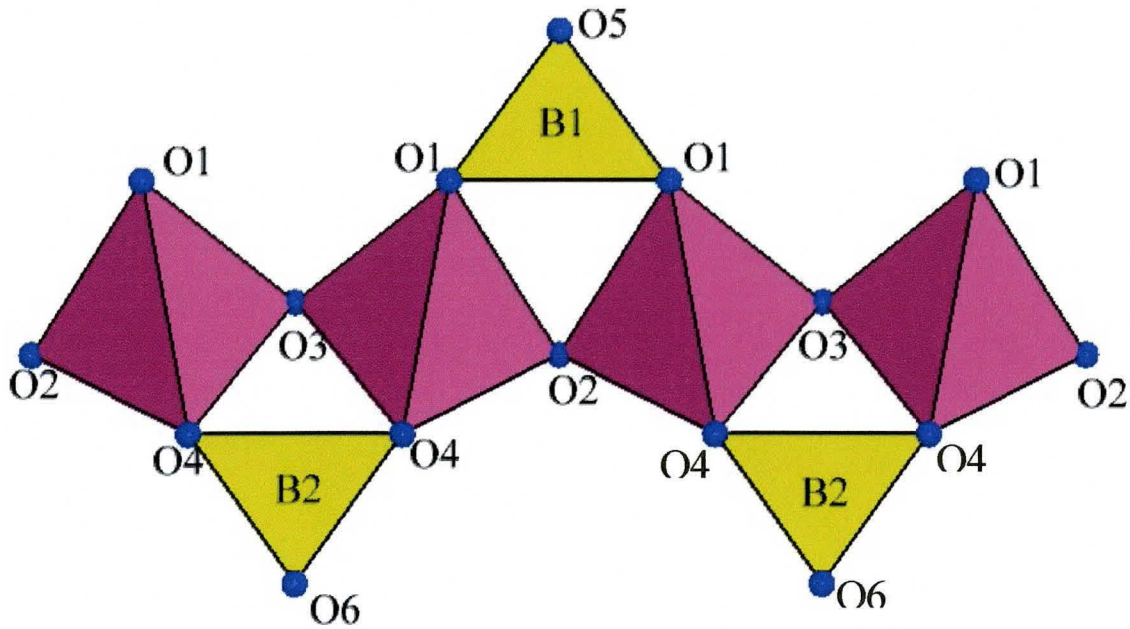

Figure 5.4 Part of the $SrGaBO_4$ structure showing GaO_4 chain and BO_3 groups. Angular distortions of the chain are caused by rigid BO_3 triangles.

where the octahedral MO_6 chains are tilted to provide regular triangular coordination environments around the bridging B atoms (cf. Figure 3.4).

The Sr atoms, coordinated to the oxygen atoms from $GaO_4 - BO_3$ chains, occupy two different sites whose positions differ by 1/2 along the c-axis. The Sr1 and Sr2 atoms, which are linked to each other through the bonds to O5 and O6, serve to interconnect the tetrahedral chains. Each Sr^{2+} ion is bonded to seven O atoms (monocapped trigonal prism) with two long and five short Sr – O bonds. Both Sr^{2+} ions achieve a sufficient bond valence sum of 1.9.

5.5 Comparison of $SrGaBO_4$ with Other Related Compounds

The structure of $SrGaBO_4$ displays close similarities with those of $CaMBO_4$ (M = Al, Ga) and $SrAlBO_4$ (cf. Figure 5.5). All these compounds crystallize in the orthorhombic symmetry with similar unit-cell dimensions but with different space groups (Table 5.3). The isostructural $CaAlBO_4$ (Schuckmann, 1968) and $CaGaBO_4$ (Yang *et al.*, 2001) are based on the non-centrosymmetric Ccc2 space group while the $SrAlBO_4$ structure (Nagai & Ihara, 1972) has been described in the Pccn space group. All four structures are made up of the same infinite chains of corner-sharing MO_4 tetrahedra and bridging BO_3 triangles. The Ca^{2+} or Sr^{2+} ions occupy the resulting interstitial cavities. Similar distortions along the tetrahedral chains are observed due to the bridging of rigid BO_3 groups.

The difference in space group symmetry among these structures is associated with the different coordination environments around the Sr^{2+} or Ca^{2+} ions. The Sr^{2+} ions in $SrAlBO_4$ and $SrGaBO_4$ are bonded to seven O atoms. In $CaMBO_4$, however, the smaller

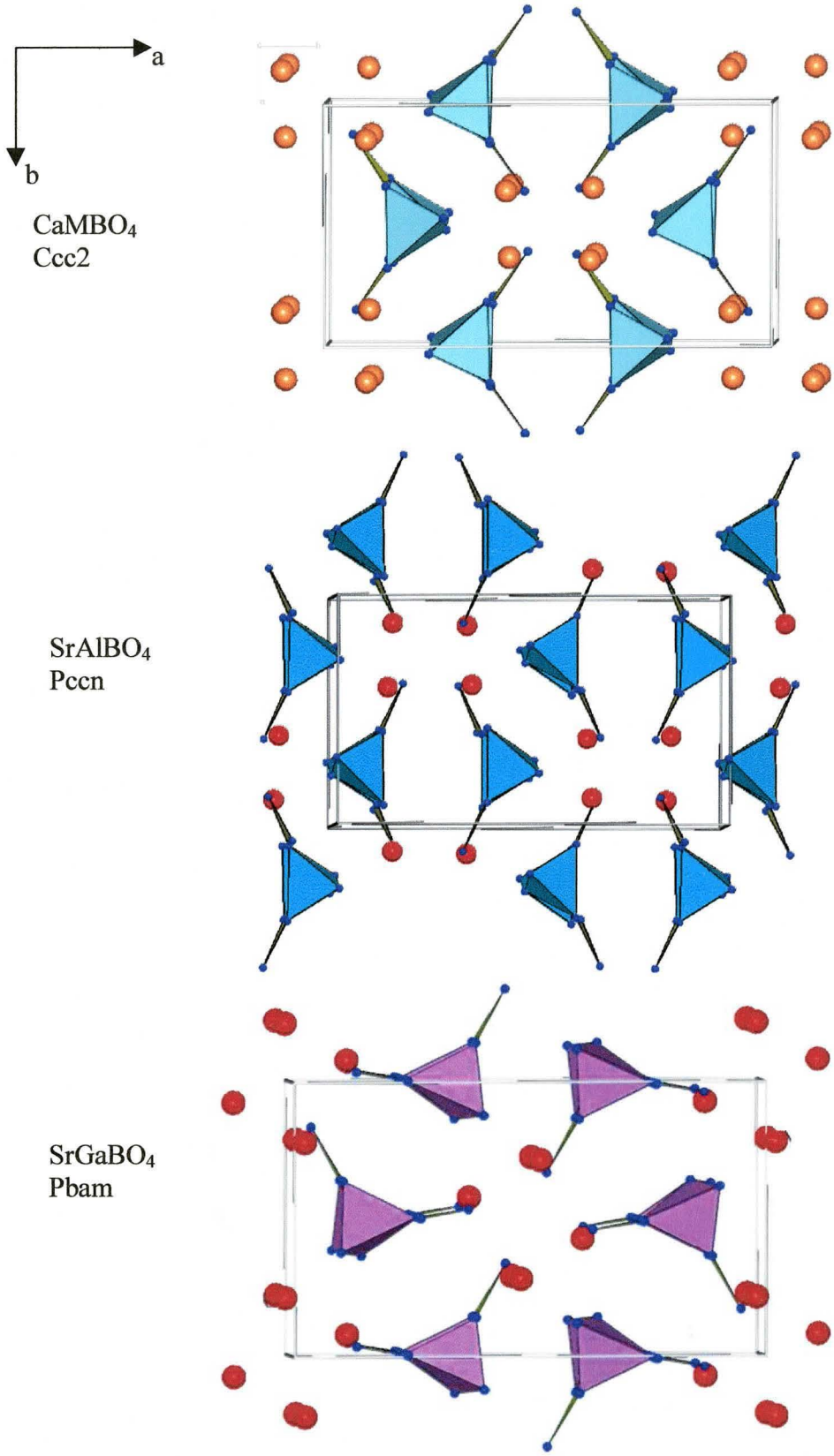

Figure 5.5 Structures of $CaMBO_4$, $SrAlBO_4$ and $SrGaBO_4$ approximately along the c-axis (M = Al, Ga). The Ca^{2+} or Sr^{2+} ions are located in the channels surrounded by MO_4 chains.

Ca^{2+} ions (1.14 Å vs. 1.32 Å, for CN = 6; Shannon, 1976) are bonded to only six O atoms, forming distorted octahedra. The GaO_4 tetrahedral chains are in turn tilted to provide adequate bonding environments of different alkaline-earth cations. The difference between $SrAlBO_4$ and $SrGaBO_4$ is probably due to the significantly different size of ionic radii of Al^{3+} and Ga^{3+} (0.675 Å vs. 0.760 Å; Shannon, 1976). However, it is difficult to make qualitative comparisons between the two structures because of the poor quality of the structure refinement results of $SrAlBO_4$ (R = 0.163) with unexpected geometries around Al and B atoms displaying large ranges of Al – O and B – O bond lengths, respectively (Nagai & Ihara, 1972).

In spite of similar chemical formulas, the structure of $SrGaBO_4$ exhibits very few similarities with that of $PbGaBO_4$ (cf. Chapter 3). The $SrGaBO_4$ structure is based on one-dimensional $GaBO_4^{2-}$ anionic chains whereas the structure of $PbGaBO_4$ is built of a three-dimensional framework of edge-sharing GaO_6 octahedral chains bridged by BO_3 triangles. The large difference between the two structures is due to the different coordination environments required by the Pb^{2+} and Sr^{2+} ions. The closed-shell Sr^{2+} cation usually lies in a more symmetrical bonding environment with a coordination number ranging from six to twelve. On the other hand, the Pb^{2+} ion contains a stereoactive lone pair which does not participate in bonding and prefers a 4-fold asymmetrical square pyramidal geometry. Indeed, $PbGaBO_4$ would not be very stable if it was to adopt the structure of $SrGaBO_4$, since the channel of GaO_4 chains could be too narrow for Pb^{2+} ions with lone pairs, resulting in large electrostatic repulsions. However, if the volume of the cavity was expanded by increasing the unit-cell dimensions to

provide enough space between the lone pairs, no suitable Pb – O bond could be achieved with reasonable distances (typically 2.3 – 2.4 Å).

5.6 Pbam vs. $P2_12_12$ space groups

A recent article by Yang *et al.* (2002) describes the *ab-initio* structure determination of β-$SrGaBO_4$ from powder X-ray diffraction data. They report that the attempts to refine the structure in the Pbam and Pba2 space groups have been unsuccessful, and thus concluded that the compound crystallizes in the non-centrosymmetric $P2_12_12$ space group. Their refined structure for β-$SrGaBO_4$ is essentially the same as that discussed in this work, with identical coordination geometry around each cation. Their refinement plot was also very similar to that presented in this thesis (cf. Figure 5.2), despite the low resolution of X-ray data. However, even though the values of the agreement factors from the two refinements are comparable, the quality of their Rietveld refinement is poorer than the one presented in this work. For instance, in their refinement, the isotropic displacement parameters of the all the atoms were fixed at 1.0 $Å^2$. The atomic coordinates of two B and two O atoms were not refined in order to obtain correct tetrahedral and triangular geometries around the Ga and B atoms, respectively. However, they do confirm the non-centrosymmetricity of the structure by observing a weak signal from second harmonic generation tests.

It is not clear why Yang *et al.* were not able to refine the β-$SrGaBO_4$ structure with the non-centrosymmetric Pba2 space group. Their refinement results do not provide any justification for the choice of the lower $P2_12_12$ symmetry. The z-coordinates of the Sr, B and some O atoms remain very close to 0 or 1/2 by taking account into the esd's.

This implies that the presence of a mirror plane perpendicular to the c-axis, and these atoms may be located on the mirror. In this work, electron diffraction technique was employed to confirm the presence of a b-glide plane normal to the a-axis (cf. Figure 5.1). Moreover, no extinction violations from extra symmetry elements, namely b-glide ($0kl$, $k = 2n + 1$) and a-glide ($h0l$, $h = 2n + 1$) planes, were observed in the diffractometer data when the Pbam or Pba2 space group was used to refine the structure (cf. Table 5.1).

In conclusion, it can be said that the structure of $SrGaBO_4$ is better described in the Pbam setting based on the comparison of the refinement details. However, more studies, such as synchrotron or single crystal X-ray diffraction, may be necessary to prove whether the true space group should be Pbam, Pba2 or $P2_12_12$.

Chapter 6

SYNTHESIS AND STRUCTURAL CHARACTERIZATION OF $Ba_3Ti_3B_2O_{12}$

6.1 Introduction

Previous studies on the $BaO - TiO_2 - B_2O_3$ system have identified $BaTiB_2O_6$ as a dolomite-type compound (Vicat & Aléonard, 1968) and another compound reported as $Ba_2Ti_2B_2O_9$ (Millet *et al.*, 1986). This chapter describes the re-investigation of the latter compound and its re-formulation as $Ba_3Ti_3B_2O_{12}$. This compound is shown to be isostructural to $K_3Ta_3B_2O_{12}$ (Abrahams *et al.*, 1981) and $K_3Nb_3B_2O_{12}$ (Becker *et al.*, 1996, 1997). It is also closely related to a number of silicate compounds, such as $Ba_{1.5}M_3Si_2O_{13}$ (Shannon & Katz, 1970) and $K_3M_3Si_2O_{13}$ (M = Ta, Nb) (Choisnet *et al.*, 1976; Jaulmes *et al.*, 1995).

6.2 Sample preparation

6.2.1 Solid-State Synthesis

A polycrystalline sample of $Ba_3Ti_3B_2O_{12}$ was obtained from the reaction between stoichiometric amounts of $BaCO_3$ (or $Ba(NO_3)_2$), TiO_2 and H_3BO_3 powders. After dehydrating H_3BO_3 at 500°C, the pelletized sample was fired up to 900°C for 5 days with daily regrinding. It was also prepared by firing a stoichiometric mixture of $BaTiO_3$ and H_3BO_3 at 500°C for 18 hours, followed by 900°C for 5 days. However, a small amount of $BaTiO_3$ remained persistently in the final products of both preparations, even after a long annealing period of 10 days. In an attempt to react the remaining $BaTiO_3$ present in the product, a small excess of H_3BO_3 (10% by mole) was also added to the sample.

However, the addition of H_3BO_3 resulted in the formation of $BaTiB_2O_6$ instead. The following equations depict the preparations of $Ba_3Ti_3B_2O_{12}$.

$$3BaCO_3 + 3TiO_2 + 2H_3BO_3 \rightarrow Ba_3Ti_3B_2O_{12} + 3H_2O + 3CO_2$$

$$3Ba(NO_3)_2 + 3TiO_2 + 2H_3BO_3 \rightarrow Ba_3Ti_3B_2O_{12} + 3N_2O_5 + 3H_2O$$

$$3BaTiO_3 + 2H_3BO_3 \rightarrow Ba_3Ti_3B_2O_{12} + 3H_2O$$

6.2.2 Single Crystal Growth

Small crystals of $Ba_3Ti_3B_2O_{12}$ were grown by slow-cooling of a melt of composition intermediate between $BaTiO_3$ and $BaTiB_2O_6$. The growth conditions for the desired compound were difficult to establish due to its incongruent melting at high temperatures (>950°C). In order to find optimal crystal growth conditions, a number of experiments were carried out by varying the x / y molar ratio of the $BaTiO_3$:$BaTiB_2O_6$ starting materials (x / y = 1, 1.3, 1.5 and 2), and the best result was obtained using a melt with a 1:1 molar ratio of $BaTiO_3$ and $BaTiB_2O_6$. The starting materials were synthesized by the following reactions:

$$BaCO_3 + TiO_2 \rightarrow BaTiO_3 + CO_2 \text{ (at 900°C, 3 days)}$$

$$BaCO_3 + TiO_2 + 2H_3BO_3 \rightarrow BaTiB_2O_6 + CO_2 + 3H_2O \text{ (at 850°C, 3 days)}$$

A 12.0-g mixture of the 1:1 molar ratio of $BaTiO_3$ and $BaTiB_2O_6$ was melted at 1100°C in a covered platinum crucible and soaked at the same temperature for 3 hours to ensure the homogeneity of the melt. It was subsequently cooled slowly down to 850°C at

Table 6.1 Products from single crystal growth of $Ba_3Ti_3B_2O_{12}$ by slow-cooling of a melt of $BaTiO_3$ and $BaTiB_2O_6$

Crystal	Colour and morphology
$BaTiB_2O_6$ (hexagonal, dolomite-type)	colourless prisms/plates (major phase)
$BaTiO_3$ (tetragonal, perovskite)	light yellow prisms
$BaTi_2O_5$ (monoclinic)	green-yellow prisms
$Ba_3Ti_3B_2O_{12}$ (hexagonal)	colourless plates (small amount)

a rate of 1°C hr^{-1}. The product consisted of single crystals of several different phases as shown in Table 6.1. Since both $Ba_3Ti_3B_2O_{12}$ and $BaTiB_2O_6$ crystallize in the hexagonal system, they had similar plate-like morphologies. Therefore, it was only possible to distinguish them by determining the unit-cell parameters of selected crystals by X-ray diffraction.

6.3 Structure Determination and Refinement from Single Crystal X-ray Diffraction Data

The structure of $Ba_3Ti_3B_2O_{12}$ was determined from single crystal X-ray diffraction data. The details of the refinement are given in Table 6.2. The unit-cell parameters were refined using Guinier powder X-ray diffraction data, based on the cell dimensions of $Ba_2Ti_2B_2O_9$ given by Millet *et al.* (1986). The raw intensity single crystal X-ray data were first corrected for Lorentz and polarization effects with the computer software SAINT (Siemens, 1996). An empirical absorption correction was applied using the program SADABS (Sheldrick, 2001). The structure solution was obtained in the non-centrosymmetric hexagonal space group $P\bar{6}2m$. The lack of a centre of symmetry was subsequently confirmed by observing a second harmonic generation signal using a polycrystalline sample (test performed by A. Kahn-Harari at Ecole Nationale Supérieure de Chimie de Paris, France). The atomic positions of Ba, Ti and O were determined via direct methods using the program SHELXTL (Sheldrick, 1997), and subsequent Fourier difference maps yielded the position of one B atom. The full least-squares refinement of 27 parameters was then carried out with anisotropic displacement parameters, secondary extinction and a chiral twin parameter. The final refinement

Table 6.2 Crystallographic data and refinement details for $Ba_3Ti_3B_2O_{12}$

Crystal system	Hexagonal
Space group	$P\bar{6}2m$
Unit cell (Å)	a = 8.7377(11)
	c = 3.9417(8)
Volume ($Å^3$)	260.62
Z	1
Calc. density (g cm^{-3})	4.902
Wavelength	MoKα
Crystal dimensions (mm)	0.15 x 0.20 x 0.30
Absorption coefficient (mm^{-1})	13.40
2θ max (°)	72.61
Index ranges	$-13 < h < 14$
	$-14 < k < 11$
	$-5 < l < 6$
Unique reflections	504
Absorption correction	SADABS (Sheldrick, 2001)
T_{min}/T_{max}	0.599
BASF (chiral twinning parameter)	0.965
R_{int}	0.036
Refined parameters	27
Goodness-of-fit	1.2
R [$F > 4\sigma(F)$]	0.016 (for 493 reflections)
$wR(F^2)$	0.039
Difference map (e $Å^{-3}$)	1.04 (1.38 Å from Ba)
	-1.00 (0.74 Å from Ba)

converged to $wR(F^2) = 0.0393$ for 504 unique reflections. The final Fourier difference map did not display any unusual features, except for small residual densities near Ba sites.

Upon the observation of somewhat large anisotropic U_{33} coefficients for all the atoms, the structure refinement was also attempted with different space groups of lower symmetry. Two subgroups of $P\bar{6}2m$, namely P31m and $P\bar{6}$, were tried since they converged to the lowest figures of merit with no extinction violations. The refinement of 39 parameters in the trigonal P31m space group converged to $wR(F^2) = 0.0394$ for 757 unique reflections. All the z-coordinates were found to be very close to 0 or 1/2, which indicates the existence of an additional 2-fold axis perpendicular to the c-axis. The refinement based on the hexagonal $P\bar{6}$ space group was also carried out with 42 parameters. The final refinement converged to $wR(F^2) = 0.0415$ for 921 independent reflections. All the x-coordinates in the general positions were located near 0, implying that these atoms lie on mirror planes parallel to the c-axis. Since these refinements did not produce any significant improvements, it was concluded that $Ba_3Ti_3B_2O_{12}$ crystallizes in the $P\bar{6}2m$ space group, and is therefore isostructural to $K_3Nb_3B_2O_{12}$ (Becker *et al.*, 1997) and $K_3Ta_3B_2O_{12}$ (Abrahams *et al.*, 1981).

The atomic positions and isotropic temperature parameters of $Ba_3Ti_3B_2O_{12}$ are given in Table 6.3. The anisotropic displacement parameters are listed in Table 6.4.

Table 6.3 Atomic coordinates and isotropic displacement Parameters for $Ba_3Ti_3B_2O_{12}$

Atom	x	y	z	$U_{eq}(Å^2)$
Ba	0	0.39979(4)	1/2	0.00860(9)
Ti	0	0.76337(11)	0	0.0087(2)
B	1/3	2/3	0	0.0057(10)
O1	0	0.7394(6)	1/2	0.0168(9)
O2	0	0.1897(4)	0	0.0076(6)
O3	0.3222(5)	0.5058(5)	0	0.0197(7)

Table 6.4 Anisotropic displacement parameters for $Ba_3Ti_3B_2O_{12}$

	U_{11}	U_{22}	U_{33}	U_{23}	U_{13}	U_{12}
Ba	0.0099(2)	0.0086(1)	0.0078(1)	0	0	0.00497(7)
Ti	0.0030(4)	0.0036(3)	0.0193(4)	0	0	0.0015(2)
B	0.004(2)	0.004(2)	0.009(2)	0	0	0.0021(8)
O1	0.017(2)	0.014(1)	0.020(2)	0	0	0.008(1)
O2	0.005(2)	0.005(1)	0.013(1)	0	0	0.0023(8)
O3	0.014(2)	0.008(1)	0.039(2)	0	0	0.007(1)

6.4 Description of $Ba_3Ti_3B_2O_{12}$ Structure

Selected bond lengths, bond valences and bond angles are listed in Table 6.5. The structure of $Ba_3Ti_3B_2O_{12}$ is illustrated in Figures 6.1 and 6.2.

The $Ba_3Ti_3B_2O_{12}$ compound crystallizes in the non-centrosymmetric $P\bar{6}2m$ space group. Its structure consists of trimers of corner-sharing TiO_6 octahedra which are interconnected by triangular BO_3 groups to form layers parallel to the (001) plane. Adjacent (001) layers are linked by the apical (O1) oxygen atoms of the TiO_6 octahedra to create a three-dimensional framework with [001] octahedral chains. The distorted octahedral geometry around the Ti^{4+} ion can be understood by considering the coordination environment around each oxygen atom (Table 6.5). The Ti – O3 bonds need to be weaker and longer because O3 is bonded to the B atom to create a rigid BO_3 triangle. On the other hand, the O1 and O2 atoms can form stronger bonds with Ti^{3+}, since they do not receive any bonding contributions from the B atom. The variations in Ti – O bond lengths can be also attributed to the fact that the Ti^{4+} ion does not occupy the centre of the octahedron. The inspection of the y-coordinates (Table 6.3) and the O1 – Ti – O1 angle (Table 6.5) indicates that the Ti^{4+} ion is not exactly aligned with the apical O1 atoms. It is actually displaced towards the O2 atoms, as indicated by the O3 – Ti – O3 and O2 – Ti – O2 angles of 84° and 98°, respectively.

The Ba^{2+} cations are located in the irregular pentagonal tunnel parallel to the c-axis. Their coordination can be regarded as a [10+3]-fold distorted tricapped pentagonal prism by including all the Ba – O bonds less than 3.32 Å, i.e. 3 Ba – O1, 2 Ba – O2 and 8 Ba – O3 bonds (cf. Table 6.5). The Ba – O2 bonds are particularly short (2.693 Å) because the Ba^{2+} ion does not lie in the centre of the pentagonal cavity. The

displacement of the Ba^{2+} ion can be understood by considering the bond valence sums around the oxygen atoms. Two short Ba – O2 bonds lead to the over-bonding of the O2 atom with a bond-valence sum of 2.24. However, if the Ba^{2+} ion were located in the centre of the cavity, this would result in shorter Ba – O3 bonds instead. The over-bonding of the O3 atom, in turn, would cause a greater instability of the structure since the site multiplicity of O3 (6j site) in the unit-cell is twice as large as that of O2 (3f site). Therefore, it is apparently energetically more favourable to have short Ba – O2 bonds rather than short Ba – O3 bonds.

The bond valence analysis (Brese & O'Keefe, 1991) indicates that the Ba^{2+} cation is somewhat over-bonded ($\Sigma s = 2.19$) while the Ti^{4+} ion is slightly under-bonded ($\Sigma s = 3.85$). These observations suggest that the Ba^{2+} cations may be too large (1.75 Å for CN = 12; Shannon, 1976) for the pentagonal channels of the TiO_6 and BO_3 framework. The smaller Sr^{2+} ion (1.58 Å for CN = 12) may be a better candidate for the cation in the interstitial holes in this structure. However, attempts to prepare a Sr-analogue of $Ba_3Ti_3B_2O_{12}$ via solid-state reactions have been unsuccessful due to the formation of the extremely stable $SrTiO_3$ compound which does not undergo any further reaction with B_2O_3 under normal conditions.

The variations in the bond valence sums around the O atoms illustrate the presence of strain in the structure. The five-coordinated O1 atom (3Ba + 2Ti) is significantly under-bonded ($\Sigma s = 1.68$) due to long Ba – O1 bonds. However, relatively short Ti – O2 and Ba – O2 bonds cause the four-coordinated O2 atom (2Ba + 2Ti) to be over-bonded ($\Sigma s = 2.28$). Although the O3 atom is coordinated to six atoms including B

Table 6.5 Bond distances (l), bond valences (s) and bond angles (°) in $Ba_3Ti_3B_2O_{12}$

l (Å)		s		
Ba – O1	2.968(5)	0.160	O1 – Ti – O1	167.9(3)
Ba – O1 x2	3.071(1)	0.121	O1 – Ti – O2 x2	94.0(1)
Ba – O2 x2	2.693(3)	0.336	O1 – Ti – O3 x2	85.5(1)
Ba – O3 x4	2.909(3)	0.188	O2 – Ti – O2 x2	98.4(2)
Ba – O3 x4	3.172(3)	0.092	O2 – Ti – O3 x2	88.9(1)
		Σs 2.19	O2 – Ti – O3	172.7(2)
			O3 – Ti – O3 x2	83.8(2)
Ti – O1 x2	1.9819(7)	0.637		
Ti – O2 x2	1.896(1)	0.803	O3 – B – O3 x3	120
Ti – O3 x2	2.081(3)	0.487		
		Σs 3.85		
B – O3 x3	1.360(3)	1.030		
		Σs 3.09		
O1 – Ba	2.968(5)	0.160		
Ba x2	3.071(1)	0.121		
Ti x2	1.9819(7)	0.637		
	Σs	**1.68**		
O2 – Ba x2	2.693(3)	0.336		
Ti x2	1.896(1)	0.803		
	Σs	**2.28**		
O3 – Ba x2	3.172(3)	0.092		
. Ba x2	2.909(3)	0.188		
Ti	2.081(3)	0.487		
B	1.360(3)	1.030		
	Σs	**2.08**		

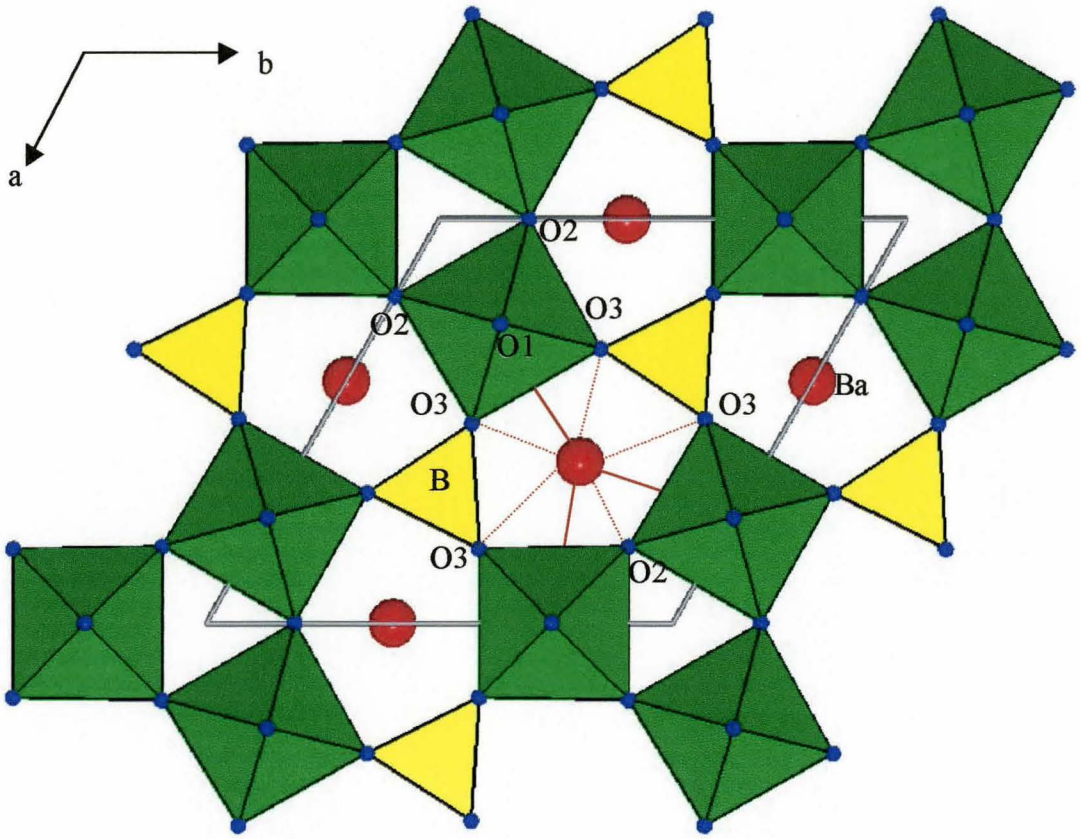

Figure 6.1 Crystal structure of $Ba_3Ti_3B_2O_{12}$ viewed along the [001] direction. Three TiO_6 octahedral chains, depicted by green polyhedra, are interconnected by BO_3 triangles. The Ba^{2+} ions are located in the resulting pentagonal channels.

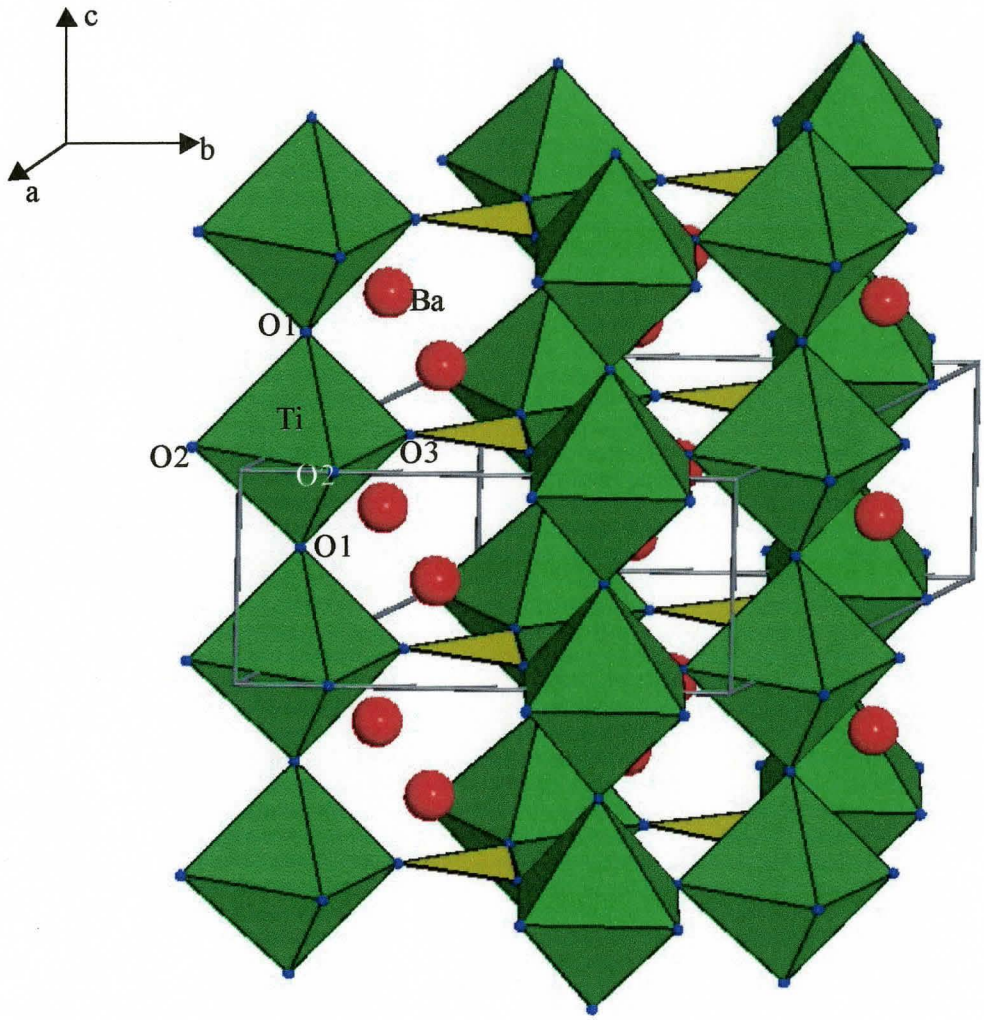

Figure 6.2 Structure of $Ba_3Ti_3B_2O_{12}$ viewed near the [111] direction. The octahedral chains run parallel to the c-axis, and the perfectly planar BO_3 triangles are perpendicular to the chain direction.

(4Ba + Ti + B), it attains the expected sum of 2.09 due to small contributions from the long, weak Ba – O3 and Ti – O3 bonds.

The compound $Ba_3Ti_3B_2O_{12}$ is isostructural to $K_3Ta_3B_2O_{12}$ (Abrahams *et al.*, 1981) and the high-temperature form of $K_3Nb_3B_2O_{12}$ (Becker *et al.*, 1997), which have been investigated for their piezoelectric properties. The crystal data of the three compounds are given in Table 6.6. In the K-based borates, the octahedral coordination environments around the Nb^{5+} and Ta^{5+} ions are more regular than that around the Ti^{4+} ion in $Ba_3Ti_3B_2O_{12}$. The O2 – Nb – O2 and O2 – Ta – O2 angles attain the expected angles (90.1° and 90.6°, respectively). This implies that the larger Nb^{5+} and Ta^{5+} ions remain in the centres of the NbO_6 and TaO_6 octahedra, respectively.

It is surprising to observe that the unit-cell volume of $Ba_3Ti_3B_2O_{12}$ is almost identical to that of $K_3Ta_3B_2O_{12}$ in spite of the presence of the smaller Ba^{2+} and Ti^{4+}cations (cf. Table 6.6). This can be attributed to the fact that the unit-cell dimension along the c-axis in $K_3Ta_3B_2O_{12}$ is actually the shortest with Ta – O1 and K – O1 bonds being slightly shorter than the corresponding bonds in $Ba_3Ti_3B_2O_{12}$ and $K_3Nb_3B_2O_{12}$. As a result, the short bond distances lead to over-bonding of the K^+ and Ta^{5+} ions with bond valence sums of 1.34 and 5.22 for K^+ and Ta^{5+}, respectively. This result indicates that the pentagonal cavities in $K_3Ta_3B_2O_{12}$ are too small for the K^+ ions.

In contrast, in the high temperature phase of $K_3Nb_3B_2O_{12}$, the pentagonal tunnels are sufficiently large to be occupied by the K^+ ions, as shown by more satisfactory bond valence sums of 1.10 and 4.96 around the K^+ and Nb^{5+} ions, respectively. Moreover, the oxygen atoms in this compound achieve the most adequate bond valence sums (1.83, 2.18

Table 6.6 Crystallographic data for $Ba_3Ti_3B_2O_{12}$ and its related compounds

Compound	S.G.	a (Å)	c (Å)	V (Å^3)	Z	Reference
$Ba_3Ti_3B_2O_{12}$	$P\bar{6}2m$	8.7377(11)	3.9417(8)	260.62	1	This work
$K_3Ta_3B_2O_{12}$	$P\bar{6}2m$	8.7816(0)	3.8990(0)	260.40	1	Abrahams *et al.* (1981)
$K_3Nb_3B_2O_{12}$ (high T)	$P\bar{6}2m$	8.779(1)	3.983(1)	265.85	1	Becker *et al.* (1997)
(low T)	$P2_1ma$	a = 17.506(2) b = 15.162(3)	3.968(4)	1053.2	4	Becker *et al.* (1996)
$Ba_{1.5}Nb_3Si_2O_{13}$	$P\bar{6}2m$	9.00(1)	7.89(1)	553.5	2	Shannon & Katz (1970)
$K_3Nb_3Si_2O_{13}$	$P\bar{6}2c$	9.012(1)	8.027(1)	564.6	2	Jaulmes *et al.* (1995)

and 2.11). This result suggests that the high-temperature $K_3Nb_3B_2O_{12}$ structure is the most stable and strain-free among the three borate structures.

The room temperature form of $K_3Nb_3B_2O_{12}$ (Becker *et al.*, 1996) shares many structural similarities with its high temperature form as well as with $Ba_3Ti_3B_2O_{12}$. This compound crystallizes in the pseudo-hexagonal symmetry where the unit-cell dimension ratio of a to b is equal to $2/\sqrt{3}$. The coordination environment around each cation is equivalent to that observed in $Ba_3Ti_3B_2O_{12}$ and in the high-temperature polymorph. However, the coordination environment around the Nb^{5+} ions in the room temperature $K_3Nb_3B_2O_{12}$ structure is more irregular with one short and one long apical Nb – O bonds. Nevertheless, all the Nb^{5+} cations still achieve the expected bond valence sums ($\Sigma s = 4.98$ to 5.15). Contrary to what is observed in the high-temperature phase, the K^+ ions are now over-bonded with bond valence sums ranging from 1.24 to 1.32 as the less symmetrical $NbO_6 – BO_3$ framework leads to contraction of the volume of the pentagonal cavity.

The three borates discussed above are also closely related to six alkali or alkaline-earth tantalum or niobium silicate compounds of composition, $Ba_{1.5}M_3Si_2O_{13}$ (Shannon & Katz, 1970a), $Sr_{1.5}Ta_3Si_2O_{13}$ (Shannon & Katz, 1970b), $K_3Ta_3Si_2O_{13}$ (Choisnet *et al.*, 1976) and $K_3Nb_3Si_2O_{13}$ (Jaulmes *et al.*, 1995). The structures of $Ba_{1.5}Nb_3Si_2O_{13}$ and $K_3Nb_3Si_2O_{13}$ are described in Figure 6.3. They crystallize in the hexagonal $P\bar{6}2m$ or $P\bar{6}2c$ space group with structures based on the triple chains of MO_6 octahedra bridged by Si_2O_7 dimers which effectively replace two BO_3 triangular groups, resulting in the doubling of the c-axis. The MO_6 octahedra are also subjected to similar distortions observed in the borates. In this case, the variations in M – O bond lengths are caused by

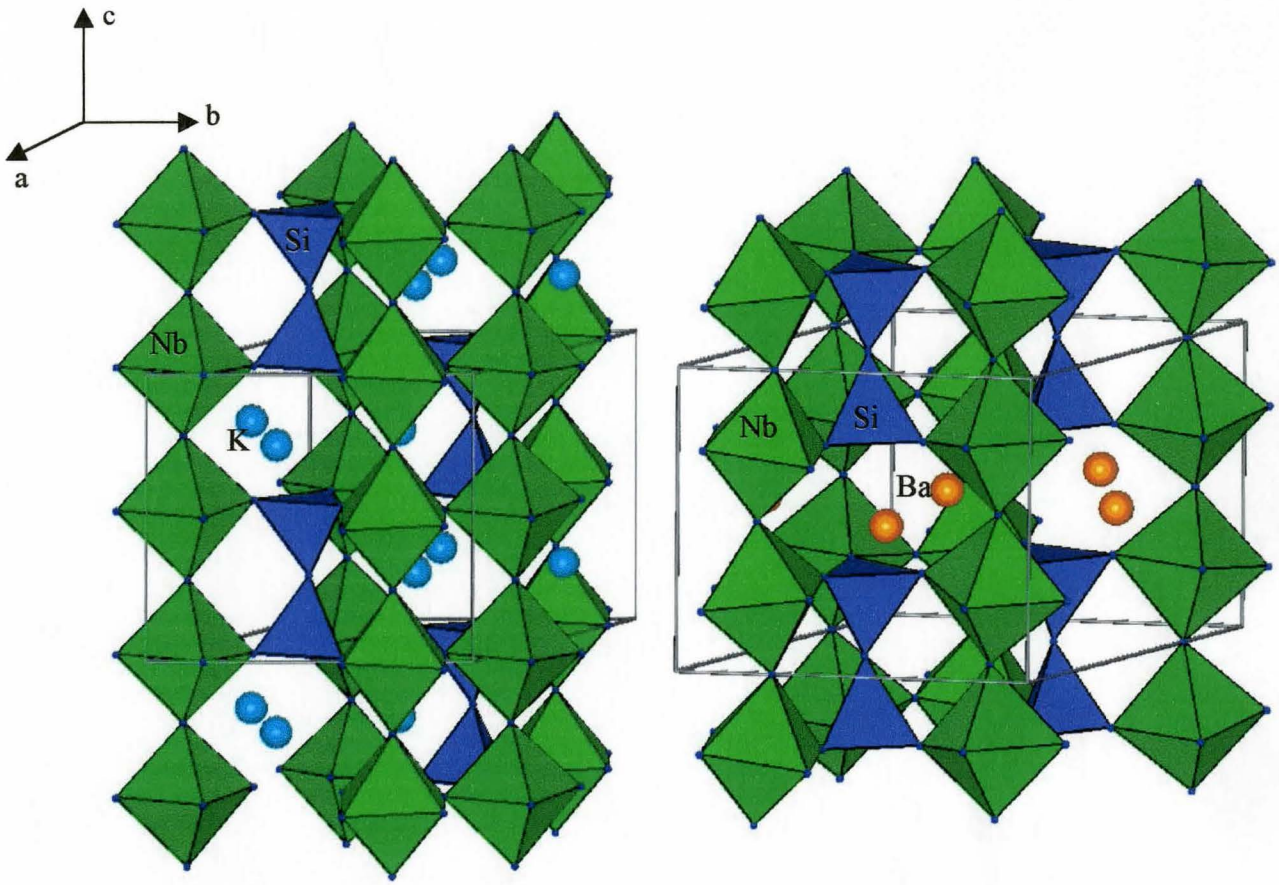

Figure 6.3 Structures of the P$\bar{6}$2c $K_3Nb_3Si_2O_{13}$ (left; Jaulmes *et al.*, 1995) and the P$\bar{6}$2m $Ba_{1.5}Nb_3Si_2O_{13}$ (right; Shannon & Katz, 1970). In both structures, the NbO_6 chains are held together by Si_2O_7 groups.

strong, covalent Si – O bonds from the SiO_4 tetrahedra. These borate and silicate structures display many similarities with tetragonal tungsten bronze structures, M'_xWO_3 (M' = alkali metal), where a three-dimensional network of WO_3 is formed by joining WO_6 octahedra through their vertices (Feger and Ziebarth, 1995). The M' atoms are located in tunnels of this framework.

CONCLUSION

In this thesis, three inorganic borate structure-types, $PbMBO_4$ (M = Al, Cr, Mn, Fe, Ga), $SrGaBO_4$ and $Ba_3Ti_3B_2O_{12}$, have been investigated. All these structures can be formulated as orthoborate oxides with occurrence of isolated BO_3 groups. It has been shown that the triangular coordination environment around the B atom with strong B – O bonds influences the bonding geometry of other atoms in the structure. All structures discussed in this work exhibit strong bucklings or distortions along the polyhedral chains so that a proper triangular geometry around the B atom can be attained.

Five new $PbMBO_4$ compounds have been synthesized and structurally characterized by X-ray and neutron diffraction techniques. The uniqueness of this structure can be attributed to the distinct square pyramidal coordination around the Pb^{2+} ion with a stereoactive lone pair. Further studies of the borate systems with different cations with non-bonding electrons, such as Bi^{3+} or Tl^{+}, can be carried out in order to observe the effects of lone pairs on the structure. The magnetic properties of $PbCrBO_4$, $PbMnBO_4$ and $PbFeBO_4$ are currently under investigation via SQUID and low-temperature powder neutron diffraction experiments.

The structure of $SrGaBO_4$ has been determined from powder X-ray diffraction data. Based on the structure refinement results with different space groups, it has been concluded that this structure is best described in the Pbam space group. However, more studies, such as single crystal X-ray diffraction, are required to confirm the presence of a centre of symmetry in the structure.

The re-investigation and the structural characterization of $Ba_2Ti_2B_2O_9$ via single crystal X-ray diffraction have shown that this compound should be re-formulated as $Ba_3Ti_3B_2O_{12}$. Since this structure is clearly non-centrosymmetric, future investigations on its non-linear optical properties may bring many interesting findings in the potential applications of SHG materials.

REFERENCES

Abrahams, S. C., Zyontz, L. E., Bernstein, J. L., Remeika, J. P., Cooper, A. S. (1981) *J. Chem. Phys.*, 75(11), 5456 – 5460

Altomare, A., Burla, M. C., Camalli, M., Carrozzini, B., Cascarano, G. L., Giacovazzo, C., Guagliardi, A., Moliterni, A. G., Polidori, G. and Rizzi, R. (1999) *J. Appl. Cryst.*, 32, 339 – 340

Andreev, Y. G., Lightfoot, P. and Bruce, P. G. (1997) *J. Appl. Crystallogr.*, 30, 294

Becker, P. (1998) *Adv. Mater.*, 10, 13, 979 - 992

Becker, P., Bohatý, L., Schneider, J. (1997) *Krystallografiya*, 42(2), 250 – 254

Becker, P., Held, P. and Bohatý, L. (1996) *Z. Kristallogr.*, 211, 449 – 452

Brese, N. E. and O'Keefe, M. (1991) *Acta Cryst.*, B47, 192 – 197

Brown, I. D. (1978) *Chem. Soc. Revs.*, 7(3), 359 – 376

Brown, I. D. (1981) *Structure and Bonding in Crystals*, Vol. II, Pg. 1 - 30, Academic Press

Brown, I. D. and Altermatt, D. (1985) *Acta Cryst.* B41, 244 – 247

Brown, I. D. and Shannon, R. D. (1973) *Acta Cryst.* A29, 266 – 282

Caglioti, G., Paoletti, A. and Ricci., F. P. (1958) *Nucl. Instrum.*, 3, 223 – 228

Chang, K.-S. and Keszler, D. A. (1998) *Mat. Res. Bull*, 33(2), 299 – 304

Chen, C., Wang, Y., Wu, B., Wu, K., Zeng, W. and Lu, L. (1995) *Nature*, 373, 322

Chen, C., Wu, B., Jiang, A., You, G. (1985) *Sci. Sin. B.* 28, 235

Chen, C., Wu, Y., Jiang, A., Wu, B., You, G., Li, R. and Lin, S. (1989) *J. Opt. Soc. Am.* B6, 616

Choisnet, J., Nguyen, N., Groult, D. and Raveau, B. (1976) *Mat. Res. Bull.*, 2, 887 – 894

Dariet, B., DeValette, M. and LaTourrette, B. (1978) *Acta Cryst.* B34, 3528 - 3532

Dollase, W. A. (1986) *J. Appl. Cryst.* 19, 267 – 272

Evans, H. T., Appleman, D. E. and Handwerker, D. S. (1963) *LSUCR*, Ann. Meeting, Pg. 42, Am. Crystallogr. Assoc., Cambridge, MA

Feger, C. R. and Ziebarth, R. P. (1995) *Chem. Mater.*, 7(2), 373 – 378

Grice, J. D., Burns, P. C., Hawthorne, F. C. (1999) *Canadian Mineralogist*, 37, 731 – 762

Harris, K. D. M., Johnston, R. L. and Kariuki, B. M. (1998) *Acta Cryst.* A54, 632 – 645

Harris, K. D. M., Tremayne, M. and Kariuki, B. M. (2001) *Angew. Chem. Int. Ed.*, 40, 1626 - 1651

Harris, K. D. M., Tremayne, M., Lightfoot, P., Bruce, P. G. (1994) *J. Am. Chem. Soc.*, 116, 3543

Heller, G. (1986) *Top. Curr. Chem.*, 131, 39

Hu, Z.-G., Higashiyama, T., Yoshimura, M., Mori, Y. and Sasaki, T. (1999) *Z. Kristallogr.* NCS, 214, 433 – 434

Hübner, K.-H. (1970) *N. Jb. Miner. Abh.*, 112, 150 – 160

Inorganic Crystal Structure Database (2001) Gmelin Institute, Karlsruhe, Germany

International Centre of Diffraction Data (1999) PC-PDF, Version 2.0

Jaulmes, S., Launay, S., Mahé, P. and Quarton, M. (1995) *Acta Cryst.* C51, 794 –796

Jenkins, R. and Snyder, R. (1996) *Introduction to X-ray Powder Diffractometry*, John Wiley and Sons, New York

Joubert, J. C., Shirk, T., White, W.B. and Roy, R. (1968) *Mat. Res. Bull.*, 3, 671 – 676

Krogh-Moe, J. and Wold-Hansen, P. S. (1973) *Acta Cryst.* B29, 2242 – 2246

Laugier, J. and Bochu, B. (2001) *CHEKCELL*, Laboratoire des Matérieux et du Génie Physique, INPG, France

Le Page, Y. and Calvert, L. D. (1984) *Acta Cryst.* C40, 1787 – 1789

Le Bail, A., Duroy, H. and Fourquet, J. L. (1988) *Mat. Res. Bull.*, 23, 447 – 452

Lucas, F., Jaulmes, S., Quarton, M., Le Mercier, T., Guillen, F. and Fouassier, C. (2000) *J. Solid State Chem.*, 150, 404 – 409

Machida, K., Adachi, G. and Shiokawa, J. (1979) *J. Lumin.*, 21, 101

Mamros, G. and Werner, P. E. (1973) *Acta Chem. Scan.*, 27, 493

McMurdie, J. (1941) *Res. Natl. Bur. Stand. (U.S.)*, 26, 492

Millet, J. M., Roth, R. S. and Parker, H. S. (1986) *J. Am. Ceram. Soc.*, 69(11), 811 - 814

Mori, Y., Kuroda, I., Nakajima, Sasaki, T. and Nakai, S. (1995) *Appl. Phys. Lett.*, 67, 1818

Nagai, T. and Ihara, M. (1972) *J. Ceram. Soc. Jpn.* 80, 432 - 437

Norrestam, R., Kritikos, M., Sjödin, A. (1995) *J. Solid State Chem.*, 114, 311 – 316

Pamplin, B. R. (1975) *Crystal Growth*, Pergamon Press, New York

Park, H. and Barbier, J. (2000) *J. Solid State Chem.*, 154, 598 – 602

Park, H. and Barbier, J. (2001) *Acta Cryst.* E57, i82 – i84

Pauling, L. (1929) *J. Am. Chem. Soc.*, 51, 1010

Pawley, G. S. (1981) *J. Appl. Cryst.*, 14, 357

Plötz, K.-B. and Müller-Buschbaum, Hk. (1981) *Z. Anorg. Allg. Chem.*, 480, 149 – 152

Poojary, D. M. and Clearfield, A. (1997) *Acc. Chem. Res.*, 30, 414

Rietveld, H. M. (1969) *J. Appl. Cryst.*, 2, 65 – 71

Roisnel, T. and Rodriguez-Carvajal, J. (2001) *FULLPROF*, Laboratoire Léon Brillouin, 91191, CEA, France

SAINT (1996), Release 4.05, Siemens Energy and Automation, Inc., Madison, WI

Shannon, J. and Katz, L., (1970a) *J. Solid State Chem.*, 1, 399 – 408

Shannon, J. and Katz, L., (1970b) *Acta Cryst.* B26, 105 – 109

Shannon, R. D. (1976) *Acta Crystallogr.* A32, 751 – 767

Schäfer, U. L. and Kuzel, H. J. (1970) *N. Jb. Miner. Mh.*, 4/5, 131 – 136

Schuckmann, W. (1968) *N. Jb. Miner. Mh.*, 80 – 86

Sheldrick, G. M. (2001) SADABS: Siemens Area Detector Absorption Correction Software, University of Göttingen, Germany

Sheldrick, G. M. (1997) SHELXTL, Program for the Solution and Refinement of Crystal Structures, University of Göttingen, Germany

Smith, R. W., Kennard, M. A. and Dudik, M. J. (1997) *Mat. Res. Bull.*, 32(6), 649 – 656

Tombs, N. C., Croft, W. J. and Mattraw, H. C. (1963) *Inorg. Chem.*, 2, 872

TOPAS (2000), Version 2, Bruker-AXS, Germany

Vicat, J. and Aléonard, S. (1968) *Mat. Res. Bull.*, 3, 611 – 620

Visser, J. (1969) *J. Appl. Cryst.*, 2, 89 – 95

Wells, A. F. (1984) *Structural Inorganic Chemistry,* Pg. 1064 – 1081, Clarendon Press, Oxford

Yang, Z., Liang, J. K., Chen, X. L., Xu, T. and Xu, Y. P. (2001) *J. Alloys & Compds.*, 327, 215 – 219

Yang, Z., Liang, J. K., Chen, X. L. and Chen, J. R. (2002) *J. Solid State Chem.*, 165, 119 – 124

Ye, N., Zeng, W. R., Wu, B. C., Huang, X. Y. and Chen, C. T. (1998) *Z. Kristallogr.* NCS, 213

Young, R. A. (1993) *The Rietveld Method*, Pg. 22, International Union of Crystallography, Oxford